Nanocrystalline Materials for (Solar) Photoelectrochemical Water Splitting

Von der Naturwissenschaftlichen Fakultät der
Gottfried Wilhelm Leibniz Universität Hannover

zur Erlangung des Grades

Doktorin der Naturwissenschaften

(Dr. rer. nat.)

genehmigte Dissertation von

Maryam Jami, M. Sc.

2017

Referent: Prof. Dr. rer. nat. Detlef W. Bahnemann

Korreferent: Prof. Dr. rer. nat. Thomas Scheper

Tag der Promotion: 16.05.2017

Danksagung

An dieser Stelle möchte ich mich bei allen bedanken, die mich während meiner Promotion begleitet und unterstützt haben.

Mein besonderer Dank gilt Prof. Dr. Detlef Bahnemann, der meine Arbeit in den letzten Jahren betreut hat und mir die Möglichkeit gegeben hat in seinem Arbeitskreis zu promovieren. Außerdem danke ich ihm für die wertvollen Erfahrungen, angeregten Diskussionen und die Realisierung meiner eigenen Ideen.

Prof. Dr. Thomas Scheper danke ich recht herzlich für die Möglichkeit an seinem Institut zu promovieren und für die Übernahme des Koreferats.

Ferner danke ich Prof. Dr. Jürgen Caro ganz herzlich nicht nur für die Übernahme des Vorsitzes der Promotionskommission, sondern auch für seine Unterstützung als mein zweiter Betreuer während der Arbeit an meinem Projekt.

Ich danke Dr. Ralf Dillert für seine ständige Hilfsbereitschaft, den wertvollen Erfahrungs- und Wissensaustausch und für zahlreiche Anregungen zu meiner Arbeit und viele kritische Diskussionen.

Dieser Arbeit wurde in Rahmen eines Projektes der „Hannover School for Nanotechnology" durchgeführt, daher danke ich den Förderern und Mitarbeitern dieses Programms für mein Stipendium. Ferner war Dr. Fritz Schulze Wischeler ein wichtiger Ansprechpartner während meiner Zeit in diesem Programm.

Den Praktikanten Yanpeng Suo, Hendrik Schulze und Hadeel Banbela danke ich für ihre tolle Mitarbeit und ihr hohes Engagement.

Ich danke allen Mitarbeitern des Arbeitskreises Bahnemann und dem gesamten Institut für Technische Chemie für die schöne Zeit und Zusammenarbeit. Besonderer Dank geht hierbei an: Manuel Fleisch, Luis Granone, Christoph Haisch, Imme Kretschmer und Stephanie Melchers für deren Unterstützung während der PEC-Messungen und Materialcharakterisierungen. Desweiteren möchte ich mich besonders bei Martin Pähler, Martina Weiß und Ulrike Dreschel für deren Hilfe bei all meinen Fragestellungen und Lösung meiner Probleme bedanken.

Ein großer Dank geht an meine Freunde und Kolleginnen: Jenny Schneider, Irina Lücking und Arsou Arimi für das Korrekturlesen meiner Arbeit.

Ein besonderer Dank geht an Djamal Oucherif, da ohne seine Fähigkeiten die Erstellung meiner Arbeit in LaTeX nicht möglich gewesen wäre.

Außerdem möchte ich meinen Freunden: Arsou, Anita, Camilla, Fabian, Faycal, Jenny, Irina, Lena, Pilar und Steffi für die schönen Momente innerhalb und außerhalb der Arbeitszeit danken.

Ganz besonders möchte ich meinen Eltern danken, die mich mit ihrer Unterstützung erst so weit gebracht haben. Außerdem danke ich meinen Geschwistern Zohreh und Kamran, meinem Onkel, und Soheila für das Zuhören, immer Dasein und ihre Unterstützung.

Zu guter Letzt möchte ich meinem Ehemann Jan danken. Er hat mich liebevoll und mit viel Geduld bei der Erstellung meiner Arbeit unterstützt und war mir eine große Stütze, wenn es darum ging, mir den Rücken freizuhalten.

Kurzzusammenfassung

Der Klimawandel und die absehbare Erschöpfung fossiler Brennstoffe erhöhen die Dringlichkeit der Entwicklung sauberer, billiger und erneuerbarer Energiequellen. Solare Wasserspaltung zur Herstellung von Wasserstoff und Sauerstoff ist eine ideale Strategie zur Erzeugung von Wasserstoff als eine saubere Energiequelle.

In der vorliegenden Arbeit werden Hämatit und Pyrit, die in der Natur ausreichend verfügbar und deren Bandlückenenergien für die effektive Nutzung von Solarenergie geeignet sind, für photoelektrochemische (PEC) und photokatalytische (PK) Wasserspaltung untersucht. Dabei wurden kommerziell verfügbare und selbsthergestellte kristalline Nanopartikel jeweils als Photoelektroden oder als Photokatalysatoren für die PEC oder PK Wassersspaltung eingesetzt. Die elektrochemischen Charakteristika von vorbereiteten Photoanoden (aus α-Fe_2O_3) und Photokathoden (aus FeS_2) wurden im Dunkeln und unter Bestrahlung mit sichtbarem Licht untersucht.

Die photokatalytische O_2-Bildung über α-Fe_2O_3 und die H_2-Bildung über FeS_2 wurden sowohl in reiner Form als auch mittels modifizierten Photokatalysatoren untersucht. Um ihre photokatalytische Aktivität zu erhöhen, wurde die Oberfläche der Photokatalysatoren mit verschiedenen Co-Katalysatoren (Co-Kat) wie Edelmetallen (Pt und Au) und Metalloxiden (NiO, CuO, CoO, IrO_2, Cr_2O_3 und RuO_2) modifiziert. Sulfid und Sulfit wurden als Elektronendonoren im H_2-Produktionssystem und Fe^{3+} als Elektronenfänger im O_2-Produktionssystem eingesetzt. Die H_2- und O_2-Produktionsraten für die reinen und mit Co-Kat-beladenen Photokatalysatoren (FeS_2 und Fe_2O_3) wurden unter sichtbarer Bestrahlung gemessen und die entsprechende Photoneneffizienz (ζ) bestimmt.

Um die optimale Beladung für die Co-Kat herauszufinden, wurden RuO_2/Fe_2O_3 und Pt/FeS_2 mit unterschiedlichen Gewichtsprozent (Gew.%) von RuO_2 und Pt hergestellt. Die Ergebnisse zeigen, dass der optimale Beladungsprozentsatz bei 0,5 Gew.% der Co-Kat-Beladung liegt. Darüber hinaus wurde festgestellt, dass NiO der beste Co-Katalysator für die H_2-Bildung mittels FeS_2 war, während RuO_2 die geringste Aktivität in dieser Reaktion zeigte. Im Rahmen der Untersuchungen für die O_2-Bidung stellte sich RuO_2 als bester Co-Katalysator heraus, während IrO_2 die niedrigste Aktivität zeigte.

Die komplette Wasserspaltung wurde in einer Kombination, die aus zwei Photokatalysatoren NiO/FeS_2 (H_2-Bildung), RuO_2/Fe_2O_3 (O_2-Bildung) und einem reversiblen Redoxsystem (IO_3^-/I^-) besteht, in einem Z-Scheme System untersucht.

Stichwörter: Wasserspaltung, Photokatalyse, Wasserstoffproduktion, Wasseroxidation, Hämatit, Pyrit.

Abstract

Climate change and the depletion of fossil fuels are increasing the urgency to develop clean, cheap, and renewable energy sources. Solar water splitting to form molecular hydrogen (H_2) and oxygen (O_2) is an ideal strategy to produce clean and recyclable hydrogen as an energy source.

In the present work, materials with sufficient abundance and suitable bandgap energies for visible light harvesting such as hematite (α-Fe_2O_3) and pyrite (FeS_2) were studied for photoelectrochemical (PEC) and photocatalytic (PC) water splitting. Commercially available and self-prepared crystalline nanoparticles were employed as the photoelectrodes or as the photocatalysts for PEC or PC water splitting, respectively. The electrochemical behavior of prepared photoanodes (from α-Fe_2O_3) and photocathodes (from FeS_2) were investigated in the dark and under visible light irradiation.

The photocatalytic production of O_2 over hematite and H_2 over pyrite was studied in both bare and modified photocatalysts. The surface of the photocatalysts was modified with various co-catalysts (Co-Cat) including noble metals (Pt and Au) and metal oxides (NiO, CuO, CoO, IrO_2, Cr_2O_3, and RuO_2) to enhance their photocatalytic activity. Sulfide and sulfite were used as sacrificial electron donors in the H_2 production system and Iron (III) ions as sacrificial electron scavengers in the O_2 evolution system. H_2 and O_2 production rates for the bare and the Co-Cat loaded FeS_2 and Fe_2O_3 were measured under visible light irradiation and the corresponding photonic efficiencies (ζ) were estimated.

In order to determine the optimum loading percentage of Co-Cats, RuO_2/Fe_2O_3, and Pt/FeS_2 with different weight %(wt.%) of RuO_2 and Pt were prepared. The results indicate 0.5 wt% of Co-Cat loading to be the optimum loading percent. Furthermore, NiO was found to be the best co-catalyst for H_2 formation over FeS_2, while RuO_2 showed the lowest activity in this reaction. On the other hand, RuO_2 was found to be the best co-catalyst for O_2 formation over Fe_2O_3, while IrO_2 showed the lowest activity in this reaction.

The overall water splitting was investigated in a two-step photocatalytic water splitting (Z-scheme) system consisting of NiO/FeS_2 (H_2 evolution), RuO_2/Fe_2O_3 (O_2 evolution), and IO_3^-/I^- as a reversible redox mediator.

Keywords: water splitting, photocatalysis, hydrogen production, water oxidation, hematite, pyrite.

Contents

Contents

Contents

List of Symbols

Abbreviation

A/A^- Electron Acceptor

CB   Conduction Band

Co-Cat Co-Catalyst

D/D^+ Electron Donor

FTO   Fluorine-doped Tin Oxide

GC   Gas Chromatograph

MS   Mass Spectrometer

NHE   Normal Hydrogen Electrode

QMS   Quadrupole Mass Spectrometer

RHE   Reversible Hydrogen Electrode

SCLJ   Semiconductor/Liquid Junction

SEM   Scanning Electron Microscopy

SHE   Standard Hydrogen Electrode

TEM   Transmission Electron Microscopy

UV   Ultraviolet

VB   Valence Band

Vis   Visible

XRD   X-ray Diffraction

Contents

Symbols and Units

$\Delta G°$ Standard Gibbs Energy Change

$\Delta n/\Delta t$ Evolution Rate

ϵ Molar Absorptivity

μ_{ex} Excess Chemical Potential

ν Frequency

ϕ Quantum Yield

Φ_b Schottky Barrier Height

Φ_M Work Function of the Metal

τ Average of the Grain Size of the Crystals

θ Diffraction Angle

ε_{LH} Light Harvesting Efficiency

ε_{SC} Permittivity of the Semiconductor Electrode

ζ Photonic Efficiency

A Absorbance

A Surface Area

b Path Length

C Capacitance of the Space Charge Layer

c Concentration

d_{SC} Space Charge layer Thickness

E Applied Potential

E_C Conduction Band Edge Potential

E_0 Vacuum Level

E_{FB} Flat-band Potential

E_x Electron Affinity

I Irradiance of the Lamp

J Photocurrent Density

J_0 Incident Photon Flux

J_g Absorbed Photon Flux

K Shape Factor

R_∞ Diffuse Reflection

S Scattering Coefficient

V_{on} Onset potential

z_e Number Electrons

λ_g Wavelength Correspond to Band Gap Energy

λ Wavelength

E^0 Standard Potential

E_g Band Gap Energy

L_D Diffusion Length

N_D Donor Density

°C   Degree Celsius

a.u.   Arbitrary Unit

cm   Centimeter

eV   Electron Volt

g   Gram

h   Hour

K   Kelvin

L   Liter

Contents

m   Meter

min   Minute

mol   Mole

nm   Nanometer

T   Temperature

V   Volt

W   Watt

wt%   Percentage by Weight

α   Material Absorption Coefficient

Physics Constants

ε_0 Permittivity of Free Space($8.85 \times 10^{-12}\,\mathrm{F\,m^{-1}}$)

c Speed of Light in Vacuum ($299\,792\,458\,\mathrm{m\,s^{-1}}$)

e_0 Elementary Charge ($1.602\,176\,62 \times 10^{-19}\,\mathrm{C}$)

h Planck Constant ($6.626\,068\,96 \times 10^{-34}\,\mathrm{J\,s}$)

k Boltzmann Constant ($1.381 \times 10^{-23}\,\mathrm{J\,K^{-1}}$)

N_A Avogadro Constant ($6.022\,141\,79 \times 10^{23}\,\mathrm{mol^{-1}}$)

1 Introduction and Objectives

In order to reduce the carbon output and keep the global temperature increases below $2\,°C$, alternative energy systems should be developed to replace fossil fuels [1]. Solar energy could be a source of energy to satisfy all human energy needs provided that it can be efficiently harvested. The three conventional devices for capturing and converting electromagnetic energy are photovoltaic cells, photoelectrochemical cells, and photocatalytic systems [2]. Photovoltaic cells have proven to be an effective approach and are highly efficient (up to 43.5 %) at converting solar energy to electricity. However, these cells are expensive and the electricity gained from them is difficult to store or to transfer. On the other hand, photoelectrochemical cells and photocatalytic systems can convert solar energy to fuels (such as molecular hydrogen) to overcome such problems [2, 3].

Photoelectrochemical (PEC) and photocatalytic (PC) solar energy conversion systems offer the ability to convert electromagnetic energy from the sun into chemical energy through the splitting of water into molecular hydrogen (H_2) and oxygen (O_2). Water splitting using the PEC or the PC route is an ideal strategy for producing clean and recyclable hydrogen as an energy source.

The water splitting reaction is the most fundamental and important reaction and it is also known as an artificial photosynthesis system. Artificial photosynthesis systems are developed based on the biological photosynthesis process. Nature provides a practical and efficient way to use solar energy for producing fuels in the process of the photosynthesis in plants. In photosynthesis, the solar energy is used to rearrange electrons into H_2O and CO_2, which ultimately leads to the storage of solar energy in the form of carbohydrates [4].

The difference between the two water splitting systems is that in the PC system photocatalyst powders are dispersed in a reactor with water in order to produce hydrogen and oxygen simultaneously throughout the entire suspension. On the other hand, in PEC systems the photoactive semiconductors are employed as electrodes to drive water oxidation (photoanode) and the reduction of protons to hydrogen (photocathode) similar to conventional water electrolysis. PEC systems include the

benefit of collecting the products (H_2 and O_2) separately [4, 5].

The water splitting reaction is an uphill reaction with a large positive change in the Gibbs free energy (ΔG^0=237 kJ mol^{-1}) [6]. Ideally, the energy needed to drive this reaction should be provided from the sunlight. The principle of photo-electrochemical water splitting was reported for the first time in 1972 by Honda and Fujishima using TiO_2 and Pt [7]. Since then, over 130 inorganic materials have been discovered to be convenient photocatalysts (or photoelectrodes) for the water splitting reaction. Some of these reported materials are able to perform the overall water splitting and to produce both H_2 and O_2, while the others are only able to produce one of these products. However, most of the reported materials for the overall water splitting exhibit a large band gap and this fact limits the efficient utilization of solar energy. A large part of the solar light spectrum is in the visible region, and therefore the search for suitable visible-light-driven photocatalysts is an ongoing quest [5].

Based on the Gibbs free energy of the water splitting reaction, 1.23 eV is the energy cost of this reaction. This suggests that each photocatalyst with a band gap energy of 1.23 eV could drive the water splitting reaction. In this case, this photocatalyst could have a solar to hydrogen efficiency of 47%. In reality, however, the situation is different and this reaction has significant energy losses, for example due to the respective O_2 or H_2 evolution overpotentials. When these energy losses are considered, the photocatalyst should have a band gap of at least ~ 2.3 eV and a maximum solar to hydrogen efficiency of 7% [8, 9]. It should be notice that often in the literature an optimum band gap of 2.0–2.25 eV for this reaction is recommended which reaching a higher solar to hydrogen efficiency [10, 11].

Considering the above-mentioned aspect of the photocatalytic water splitting reaction, the ultimate goal of creating efficient and cheap photocatalytic water splitting systems lies in the design of cells or combinations of photocatalysts which could simultaneously drive both hydrogen and oxygen evolution reactions upon visible light irradiation. The practical strategy will be a two-photon water splitting system. This approach in known as tandem cell configuration in PEC and as Z-scheme water splitting in PC. In both approaches it is possible to use two smaller band gap materials, thus enabling the effective utilization of solar energy.

The optimum band gaps for the dual photocatalyst systems based on the tandem cells (or Z-scheme) have been reported in several reports [8, 10, 12, 13]. Generally, one of these materials has a larger band gap than the other one. The calculation shows that for optimum efficiency the large band gap material should have a band

gap of ~ 1.7 eV while the small band gap material should have a band gap of ~ 1.0 eV. This system has the potential to yield a photocatalytic water splitting efficiency of up to 29% [8]. And further calculation shows that for a combination of two materials with band gaps of 2.25 and 1.77 eV the solar to hydrogen efficiency could be around 24% [11]. However, the dual systems are more complicated than the single photocatalyst systems (e.g. they will have twice the energy loss). One of the best reported Z-scheme systems is $Rh:SrTiO_3$ and $BiVO_4$ in combination with Fe^{3+}/Fe^{2+} as redox shuttle mediator. This system gives a solar to hydrogen efficiency of 0.1% [14].

In the present study, two semiconductors with sufficient abundance in nature were chosen to be investigated as possible candidates for the photoelectrodes in a tandem cell or as photocatalysts in a Z-scheme system. Hematite (α-Fe_2O_3) is known as a photoanode in PEC systems and the position of its band gap is suitable for O_2 evolution reaction. On the other hand, in the solar energy literatur, pyrite (FeS_2) is usually known as a suitable hydrogen evolution electrode.

The central objective of the present thesis is the realization of the photocatalytic water splitting reaction under visible light irradiation employing hematite and pyrite as the respective photocatalysts. Therefore, initially the PEC behavior of these two semiconductors should be investigated. The photocatalytic properties of both semiconductors should also be determined. For this purpose the O_2 evolution reaction on hematite and the H_2 evolution reaction on pyrite should be investigated separately. In this context, it is particularly important to quantify their performance under co-catalyst loading and in the presence of sacrificial reagents.

To achieve the goal of this study, first nanocrystalline α-Fe_2O_3 and FeS_2 were synthesized employing wet chemical bottom-up methods. These nanoparticles were then employed to prepare the PEC photoelectrodes or used as photocatalysts in the PC system. Aside from the synthesized nanoparticles, commercially available α-Fe_2O_3 and FeS_2 were also applied in this study.

The PEC measurements were performed in a three-electrode system, where Pt was the counter electrode, Ag/AgCl the reference electrode, and a pyrite- or a hematite- electrode was the working electrode, respectively. The PEC measurements include current-voltage and impedance measurements. Current-voltage characterizations were carried out both in the dark and under visible light ($\lambda > 420\,nm$) irradiation to observe the effect of light on the activity of the water oxidation or reduction reaction. Furthermore, impedance measurements were essential to determine the flat-band potential and the donor density of α-Fe_2O_3 and FeS_2.

Two approaches were used to determine the photocatalytic activity of α-Fe_2O_3 and FeS_2. First, the activity of each individual photocatalyst was investigated separately for water oxidation (with α-Fe_2O_3) or water reduction (with FeS_2) in the presence of suitable sacrificial reagents. Then the combination of the two photocatalysts in the Z-scheme system for homogenous production of H_2 and O_2 was studied.

Furthermore, in this thesis, the effect of different Co-Cat loadings on the surface of α-Fe_2O_3 and FeS_2 was studied. For this purpose noble transition metals (such as Pt or Au) or metal oxides (such as NiO or RuO_2) were loaded on the α-Fe_2O_3 or FeS_2, and the photocatalytic activity of O_2 or H_2 production respectively, was determined.

Photocatalytic H_2 or O_2 evolution was investigated in sacrificial systems. In these cases, just one half-reaction of the water splitting could occur. The oxygen evolution reaction was studied on bare and Co-Cat loaded α-Fe_2O_3 where Fe^{3+} ions were used as electron acceptors (sacrificial agents), while the hydrogen evolution reaction was investigated on bare and Co-Cat loaded FeS_2 employing sulfide and sulfite ($S^{2-}/SO_3{}^{2-}$) as sacrificial electron donors. Finally, the best Co-Cat/FeS_2 in the hydrogen evolution reaction and the best Co-Cat/Fe_2O_3 in the oxygen evolution reaction were chosen as combination for the Z-scheme water splitting. Here the overall water splitting under visible light irradiation could be observed.

2 Theoretical background

2.1 The Semiconductor

Solid materials are categorized into two types based on the temperature dependency of their electrical conductivity: metallic conductors and semiconductors. A metallic conductor is a substance with a conductivity that decreases as the temperature is raised. A semiconductor is a substance with a conductivity that increases as the temperature is raised. Usually, materials with very low electrical conductivities, such as the most synthetic polymers, are classified as insulators (Figure 2.1a,b).

When a semiconductor absorbs photons with an energy higher than its band gap energy, electrons leave the valence band and populate the empty orbitals of the conduction band. As a consequence of such an electron promotion, positively charged holes are left in the valence band. The formation of a so-called electron-hole pair is shown in Figure 2.1c.

These photogenerated electrons and holes are now mobile and can drive reduction and oxidation reactions if the charge injections into the reactants are thermodynamically favorable. The distinctions between an insulator and a semiconductor is related to the magnitude of the band gap. In the case of an insulator, the band gap is large (usually $> 4\,\mathrm{eV}$ [15]) therefore at ordinary temperatures just few electrons will be promoted and the conductivity will remain close to zero.

The semiconductors are also classified into intrinsic and extrinsic semiconductors. Examples for intrinsic semiconductors are silicon and germanium. The semiconducting properties of these materials are based on the band structure of the pure material. In an extrinsic semiconductor, the charge carriers are present as a result of the replacement of some atoms by the dopant atoms. Based on the nature of the dopants present in the semiconductor lattice, the extrinsic semiconductor can be classified into the n-type or p-type semiconductor. If the dopant has fewer electrons than its host, there will be a narrow band which accepts electrons from the valence band. As a consequence of this procedure, the holes within the band will be mobile and the substance is a p-type semiconductor (Figure 2.1d). In the case of an n-type

semiconductor, the dopant has more electrons than its host and forms a narrow band that can supply electrons to the conduction band. Thus the electrons will be mobile and build the majority of the charge carriers (Figure 2.1e).
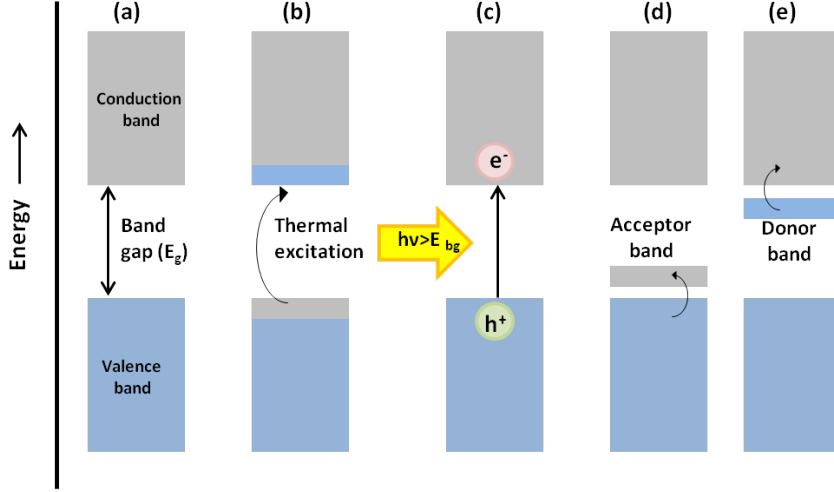
Figure 2.1: (a) an insulator or a semiconductor at $T = 0\,K$, (b) a semiconductor at T $>0\,K$, at temperatures above $0\,K$ the electrons populate the levels of the upper conduction band. (c) Photo-generation of electron-hole pairs in a semiconductor, (d) A p-type semiconductor, here the dopant exhibit less electrons than its host and the holes are the majority carriers. (e) An n-type semiconductor, here the dopant exhibit more electron than its host and the electrons are the majority carriers.

In the present work, hematite and pyrite are the two semiconductors which have been employed. A general overview of these two materials will be given in the following chapters.

2.2 Hematite

Hematite (α-Fe_2O_3) is the most common iron-bearing mineral and thermodynamically stable form of iron oxide. It is the pigment of "red beds". Hematite is an n-type semiconductor, however, the synthetic α-Fe_2O_3 can be n-type or p-type. This depends on the impurity content and oxygen deficiency in the hematite lattice. The structure of hematite can be described as a hexagonal close packing of oxygen atoms with iron in two-thirds of the octahedral interstices. They arrange in the corundum structure, where each iron has six oxygen neighbors and each oxygen has four iron neighbors [4, 16, 17]. Figure 2.2 presents the unit cell of hematite.
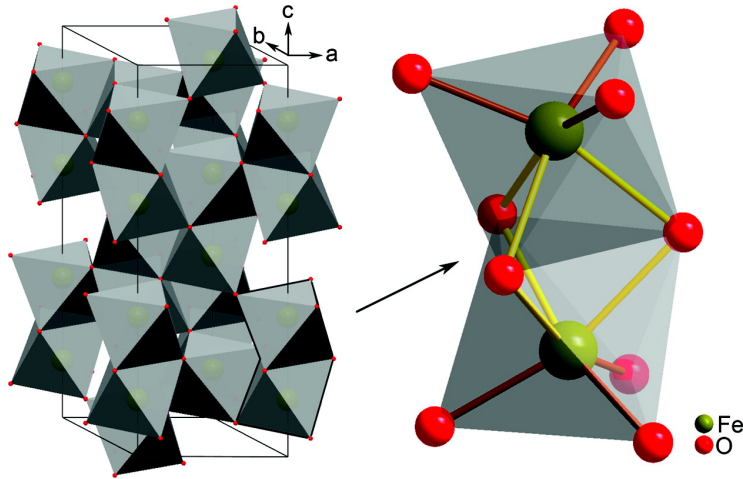
Figure 2.2: Left: the unit cell of hematite, Right: a detailed view of one Fe_2O_9 dimer, Reprinted with permission from [18], ©2010 American Chemical Society.

The band structure and the band gap of hematite play an important role for investigations of this material in solar energy conversion system. According to most of the reports hematite has indirect bandgap transition based on the transition of Fe^{3+} d–d origin [4, 19–22]. The value of the band gap has been reported to be between 1.9 and 2.2 eV corresponding to $\lambda = 650$ to 560 nm [20, 23, 24]. However, a few studies have reported a direct bandgap of hematite [25, 26]. This could be due to the charge transfer from an O 2p orbital to Fe 3d (E>3.2 eV) [19]. Hematite absorbs shorter wavelengts of the solar light spectrum (yellow to ultraviolet photon in the visible region). The characteristic red color is due to the relatively good transmission of red light [4, 18].

The conduction band energy of hematite is determined theoretically and experimentally. The theoretical calculation (using DFT + U) for the centers of the band gap of the (0001) and (0112) orientations gave the conduction band energies at -4.48 eV and -5.34 eV. However, in this calculation, the band gap energy of hematite was taken 3.08 eV. Hankin *et al.* [24] took these values and considering the band gap energy value of hematite to be 2.05 eV, recalculated the conduction band energies. These Authors reported $E_{CB} = -3.46$ eV, $E_{VB} = -5.51$ eV for the (0001) orientation and $E_{CB} = -4.32$ eV, $E_{VB} = -6.37$ eV for the (0112) orientation. Normally, these values are not expected for hematite. For example, the value -3.46 eV corresponding to -0.51 V vs. SHE. This means that hematite should be able to perform the water reduction reaction [24, 27].

However, the experimental studies gave other values and hematite usually is not able to reduce water. In some experiments, the flat band potential of hematite is determined by means of Mott-Schottky plots. The conduction band energy is usually $\sim 0.3\,\mathrm{eV}$ higher than the flat band potential. For example taking the determined value for the flat band potential of hematite 0.4 V [4, 24, 28], this gives the conduction band edge $\sim 0.1\,\mathrm{eV}$. The valence band edge could be determined by considering the band gap of the hematite.

2.3 Pyrite

Pyrite (FeS_2) is the most common sulfide mineral on earth and has a cubic structure. The name of pyrite represents a structure type for the series of material with the composition of AB_2 (such as $FeSe_2$, CuS_2, $NiSe_2$, etc.). Pyrite was the first mineral structure determined in 1914 by Bragg with his new X-ray diffraction system [29]. The crystal structure of pyrite is similar to that of the NaCl-type structure. Here the disulfide $(S_2)^{2-}$ groups are located at the anion sites while the low-spin Fe(II) atoms at the corners and face center (Figure 2.3). Each S atom is tetrahedrally coordinated with one S neighbor (the other half of the S_2 molecule) and three Fe neighbors. Each Fe is in the center of an octahedron of S atoms. Even though all six Fe-S distances are equal, the octahedron is not perfect and is slightly compressed along one axis [16, 30].

Optical and electrical properties of pyrite have been investigated in both mineral and synthetic state [16, 31–35]. These investigations found that pyrite can be both n- and p-type semiconductor [16, 30, 34, 36]. FeS_2 pyrite has a strong absorption coefficient (6×10^5 cm^{-1}) and absorbs in the visible region of the light. The band gap of the pyrite has been measured to be 0.9 ± 0.2 eV. The indirect transition state of pyrite is derived from the splitting of the iron 3d state. In this context, the conduction band is formed from the eg doublet of iron 3d orbitals and in the upper part from the 4s orbital. The valence band is formed from t_{2g} triplet of iron 3d orbitals and the antibonding 2pπ molecular orbitals of the $(S_2)^{2-}$ group [16, 30, 37, 38].

The position of the conduction band edge was reported to be $-4.5\,\mathrm{eV}$ in absolute vacuum scale ($\sim$ -0.25 V vs. NHE), taking $E_g = 0.9\,\mathrm{eV}$ the valence band edge will be $-5.4\,\mathrm{eV}$ [27, 33, 39].
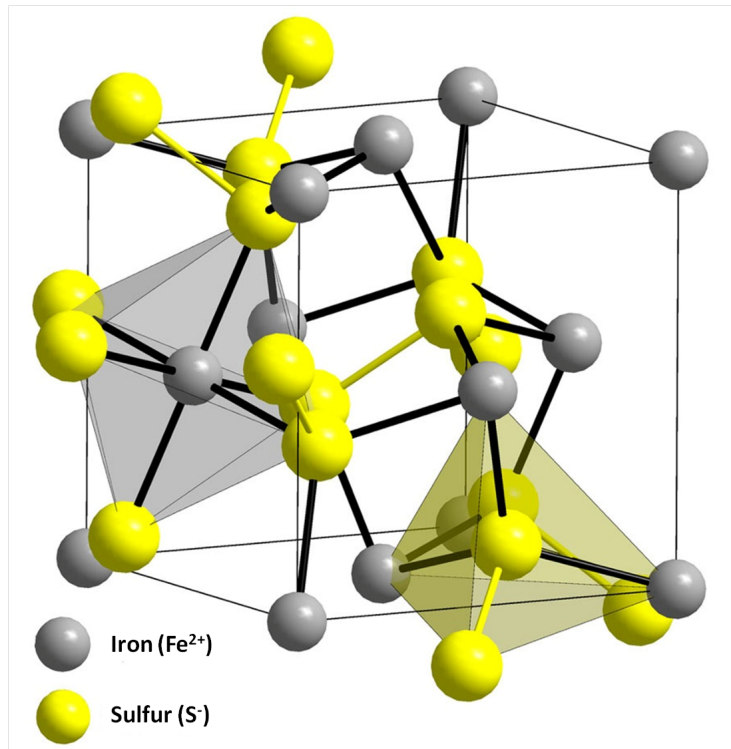
Figure 2.3: Crystal structre of pyrite, ©2009 American Mineralogist Crystal Structure Database.

2.4 Solar Water Splitting

There are several pathways for producing solar fuels (e.g., molecular hydrogen). These methods can be divided into direct and indirect pathways. Photovoltaics-electrolysis is a common indirect route. In this system, the solar energy will be converted to the electrical energy via photovoltaic cells, and the electrolyzers will convert electrical energy into chemical energy (hydrogen). However, the most elegant method seems to be the direct way. Here the solar energy will be converted to fuels without producing electricity. Photoelectrochemical (PEC) and photocatalytic (PC) solar energy conversion systems are the two direct approaches to produce solar fuel. In both approaches, semiconductor materials are applied to oxidize and reduce water to oxygen and hydrogen, respectively [2].

It is possible to distinguish between these two methods. In PC system the semiconductor (the photocatalyst) will be dispersed in pure water in order to produce hydrogen and oxygen homogeneously throughout the solution. The PC system is easy to scale-up but has a big disadvantage which is the separation of producing

hydrogen and oxygen, and this probably leads to the undesirable reverse reaction. In PCE systems the photoactive materials are employed as electrodes. In this case, usually, O_2 evolution (oxidation) occurs at the anode and H_2 evolution (reduction) occurs at the cathode. Thereby a separate collection of the products is possible [2, 4].

In this thesis, both systems have been applied. Therefore, this section deals with some basic principle of solar water splitting and the following sections deal with the description of PCE and PC water splitting systems.

2.4.1 Photoelectrolysis

The free energy change (ΔG°) of the water splitting reaction under the standard condition is 237.2 $kJ\,mol^{-1}$, which, based on the Nernst equation, corresponds to a standard redox potential (ΔE°) of 1.23 V per electron transferred. This means, that a semiconductor should absorb light with the photon energy greater than 1.23 eV ($\lambda \sim 1000$ nm and shorter) to drive the water splitting reaction.

The overall water splitting reaction consists of two half reactions as follows:

Water oxidation (oxygen evolution reaction):

$$H_2O + 2\,h^+ \longrightarrow 2\,H^+ + \frac{1}{2}\,O_2 \tag{2.1}$$
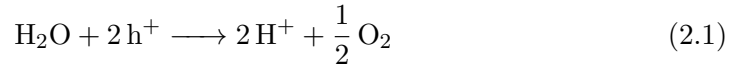
Water reduction (hydrogen evolution reaction):

$$2\,H^+ + 2\,e^- \longrightarrow H_2 \tag{2.2}$$

Overall reaction:

$$H_2O \longrightarrow H_2 + \frac{1}{2}\,O_2 \tag{2.3}$$

In this process, the oxygen evolution reaction requires four electron-hole pairs, while the hydrogen evolution reaction requires two electron-hole pairs. With this, the overall reaction is a four electron transfer reaction which can usually be promoted if a semiconductor with the suitable band gap is employed for this reaction and a catalyst for the multi-electron transfer steps is present as well.

2.4.2 Requirements of the Semiconductors

The fundamental principle of solar water splitting is shown in Figure 2.4. In the ideal case, if a semiconductor exhibits a band gap energy (E_g) value of 1.23 eV

it should be able to drive the water splitting reaction. However, in reality, the situation is different and the semiconductor should have at least a band gap value ~ 2.0–2.25 eV. Because the water splitting reaction has significant energy losses through the O_2 or H_2 evolution overpotential.
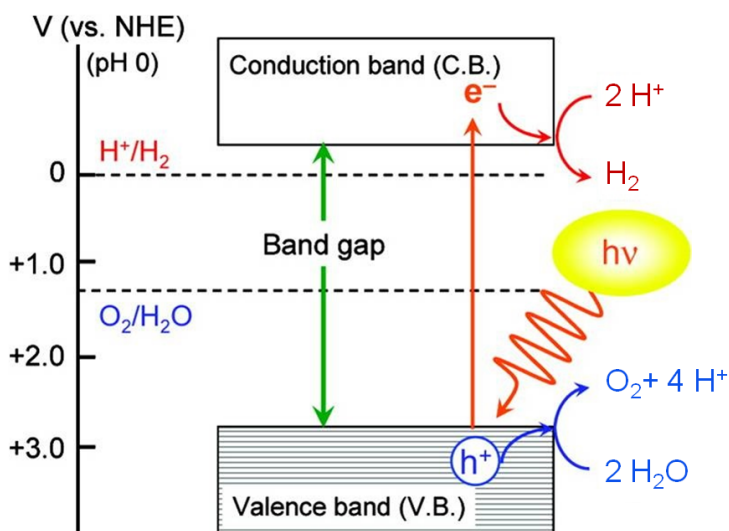
Figure 2.4: Basic principle of overall water splitting on a semiconductor particle. Adapted with permission from [40], ©2007 American Chemical Society.

Aside from (E_g), the band position of the semiconductor is also important. The conduction band edge energy (E_{CB}) and valence band edge energy (E_{VB}) should straddle the electrochemical potentials of E° (H^+/H_2) and E° (O_2/H_2O), to be able to drive the water reduction and oxidation reaction using the photogenerated electrons/holes.

Figure 2.5 depicts the band positions of several semiconductors in contact with an aqueous electrolyte at pH 1 and their relation to the potentials of water splitting. The energy scale is given on the left for comparison to the vacuum level and the normal hydrogen electrode (NHE), respectively. The fact is that the band edge position of the semiconductors can be influenced by the pH of the electrolyte.

Figure 2.5 indicates some of the possible semiconductors as candidates for water splitting. TiO_2 is one of the semiconductors, which is able to split water. However, TiO_2 is just able to absorb in the UV region of the solar spectrum. One aim of present work is water splitting utilizing solar energy. Sunlight spectrum consists of three main parts (Figure 2.6). Figure 2.6 indicates that 53 % of the solar spectrum is in the visible region while just 4% of the solar spectrum is in UV region. It is
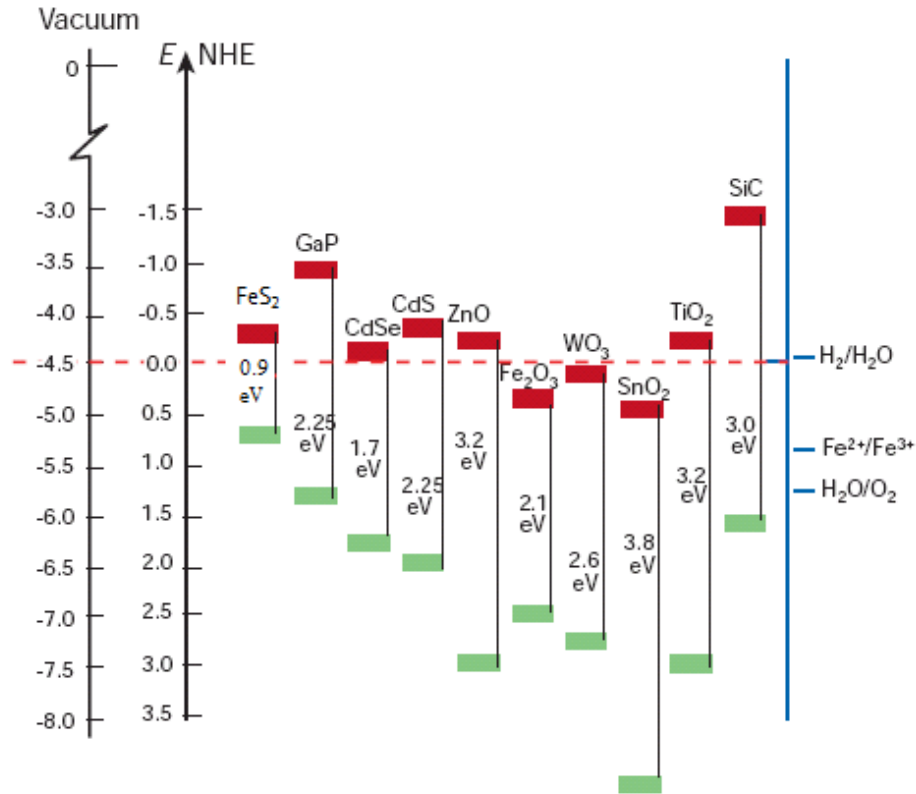
Figure 2.5: Band positions of several semiconductors in contact with aqueous electrolyte at pH 1. Adapted with permission from [3], ©2001 Nature Publishing Group.

necessary to harvest visible light for effective water splitting.

Figure 2.5 also shows some of the visible light active semiconductors. But most of these semiconductors are able to perform just half water splitting reactions. Hematite and pyrite are the two semiconductors which are investigated in this work. As Figure 2.5 indicates hematite is just able to produce O_2 while pyrite can only produce H_2.

Other important factors also should be considered for a good and suitable semiconductor for water splitting. One of this requirements is good stability in the aqueous solution (or electrolyte) under the illumination. Other factors such as charge separation, mobility and lifetime of the photogenerated electrons and holes should also be considered. These properties are strongly affected by the crystal structure, crystallinity, and particle size [5].
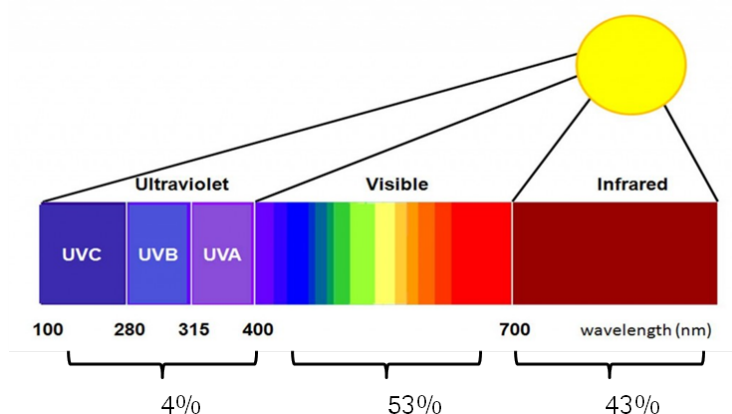
Figure 2.6: Solar light spectrum

2.5 Concept of Photoelectrochemical Cells

The basic configuration of a photoelectrochemical cell is illustrated in Figure 2.7.
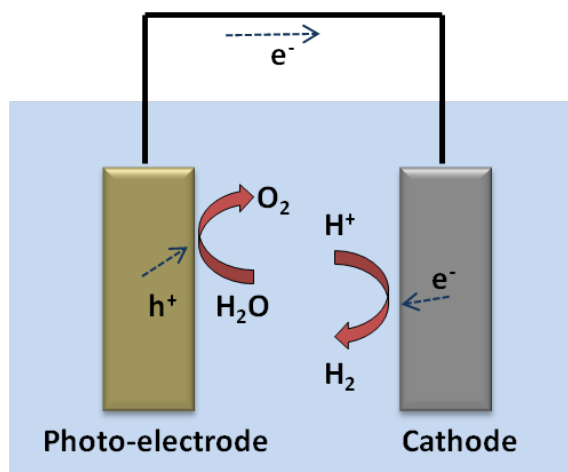
Figure 2.7: Schematic illustration of basic concept of a photoelectrochemical cell

Usually, in a PEC system, one or both electrodes can be a photoactive semiconductor. In the 1970 s Honda-Fujishima reported about using TiO_2 electrode for solar water splitting [7]. In their PEC configuration, TiO_2 was used as the photoanode and a metal (in this case Pt) as the cathode (same configuration as Figure 2.7). When TiO_2 is irradiated with UV light photogenerated electron-hole pairs are produced. The photogenerated electrons reduce water to form H_2 on the Pt counter electrode while the holes in the photoanode oxidize water and produced

O_2 with some external bias.

In this section, the effect of the band bending at the interface between semiconductor and electrolyte will be introduced, followed by using hematite (as photoanode) and pyrite (as photocathode) in the PEC system.

2.5.1 Space Charge Layer and Band Bending

When a semiconductor is brought into contact with an electrolyte solution (or other phases such as gas or metal), the electric charges will be redistributed and a double layer will be generated. The migration of the charge carriers between the semiconductor and the electrolyte, or the trapping of the charge carriers at interfacial surface states, produces a space charge layer. As the result of the formation of the space charge layer, the valence and conduction bands will be bent.
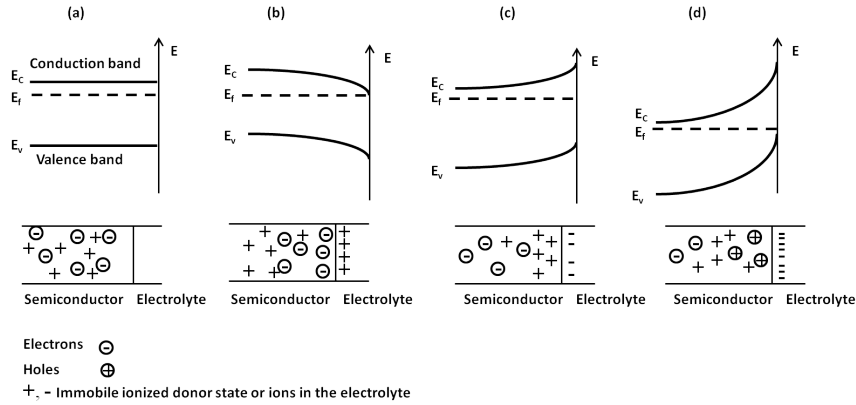
Figure 2.8: Schematic illustration showing space charge layer formation and band bending in case of an n-type semiconductor in contact with an electrolyte. (a) Flat band situation, (b) Accumulation layer, (c) depletion layer, (d) inversion layer.

Figure 2.8 depicts an n-type semiconductor in contact with an electrolyte under polarization using a potentiostat at different potentials relative to the flat band potential. In this figure, four different cases can be observed. The first case (Figure 2.8a) is the flat-band potential and there is no space charge layer. Here the applied potential is equal to the flat band potential and therefore the semiconductor exhibits a consistent charge distribution. The second case is the accumulation layer, which occurs when the applied potential is less than the flat band potential (Figure 2.8b). Here the positive charges exist at the interface and the electrons are accumulated in the semiconductor near the surface within the space charge layer

region. Hence the bands of the semiconductor are bent downwards to the direction of the surface due to the decrease of the potential energy of the electron. The third case is the depletion layer and this occurs when the applied potential is greater than the flat band potential (Figure 2.8c). In this case, the negative charges exist at the interface and positive charges accumulate near the surface. This situation is causing the upward band bending to the direction of the surface. If the depletion of majority carriers goes so far into the semiconductor, the Fermi level will decrease below the intrinsic level and site closer to the valence than the conduction band (this occurs when the applied potential is much greater than the flat band potential). In this case, the surface region of the semiconductor seems to be p-type while the bulk still shows n-type behavior. This space charge layer is called an inversion layer (Figure 2.8d).

2.5.2 α-Fe$_2$O$_3$ Photoanodes for Water Splitting

In a photoelectrochemical cell, the photoanode is responsible for oxygen evolution and is usually an n-type semiconductor. One of the most investigated photoanode material is hematite. One of the first investigations on hematite as a material for water photolysis has been done in 1976 by Hardee and Bard [41]. They investigated photocurrent measurements on thin films of Fe_2O_3 prepared on Ti and Pt substrates via chemical vapor deposition (CVD).

As mentioned in section 2.2, the band gap of hematite makes it possible for this material to absorb a significant portion of the solar spectrum. In addition, the position of the valence band edge is convenient to oxidize water. However, the position of the conduction band edge of α-Fe$_2$O$_3$ is not suitable to produce hydrogen. Thus an external bias is required to initiate the water splitting reaction (Figure 2.9). Besides its band gap, hematite has other advantages such as its chemical stability and it is nontoxic, abundant and inexpensive. All of these benefits make α-Fe$_2$O$_3$ an interesting candidate as a photoanode in PEC solar water splitting. But there are major challenges to use this material in PEC and make it a complex system.

One of the main issues is that hematite exhibits a very short hole diffusion length ($L_D = 2 - 4$ nm [21]) and this permits the unfavorable premature recombination of the electrons and holes in the material and this before they could diffuse to the surface to perform chemical reaction such as water oxidation. Hematite also needs a large overpotential for water oxidation. The reasons for this fact could come from different sources. For example, it could be due to the electrical resistance in the electrode or electrolyte, or from the depletion of charge carriers at the surface.
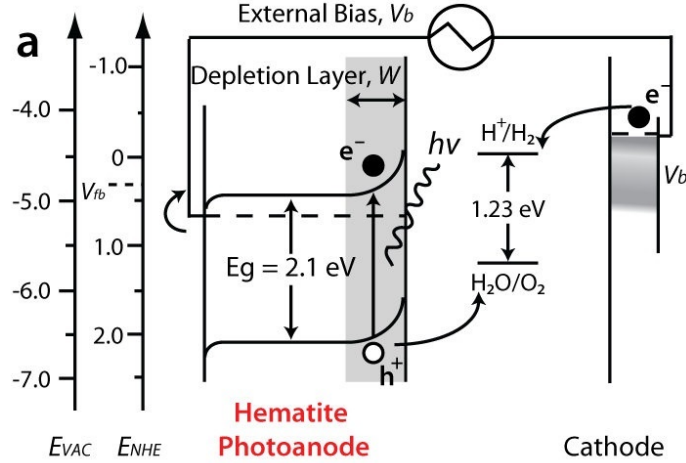
Figure 2.9: Energy diagram of a photoelectrochemical cell with a single photoelectrode, here hematite is employed as the photoanode and performed the oxygen evolution (oxidation) reaction, and a cathode performed the hydrogen evolution (reduction) reaction. Adapted with permission from [4], ©2011 John Wiley & Sons.

This occurs when an electrochemical reaction is fast enough to lower the surface concentration of the charge carriers below that of bulk solution [28, 42].

The relative low absorption coefficient of hematite ($\sim 10^4$ cm^{-1} [43, 44]) presupposes a film thickness around 400-500 nm for complete light absorption [4]. Generally, the light harvesting efficiency (ε_{LH}) of incident photons by a semiconductor is dependent on the material absorption coefficient (α) and the thickness (l) according to the following equation:

$$\varepsilon_{LH} = 1 - e^{\alpha l} \tag{2.4}$$

Based on this equation, each semiconductor needs to have a thickness of $3/\alpha$ to be able to absorb 95% of the light at a given wavelength. For example, at wavelength 550 nm for hematite ($\alpha = 8 \times 10^4$ cm^{-1}), the thickness should be 400 nm to absorb 95% of the light at this wavelength [45].

However, there are strategies to overcome these problems. The first strategy could be optimizing the electrode morphology, this leads to increasing of the water splitting photocurrent density. Because the electrode morphology affects the charge carriers recombination and this is a critical factor to control the photocurrent [4, 18,

46]. The second strategy could be, employing various surface treatment (catalysis) which help to reduce the overpotential [4, 47]. Nevertheless, the performance of the best-optimized hematite photoanodes are far from materials such as TiO_2 and WO_3 [48].

2.5.3 Photocathodes for Water Splitting

A good photocathode for the water splitting should be stable in aqueous solution and under illumination. Furthermore, it should be able to supply sufficient cathodic current to reduce protons to H_2 and as mentioned in section 2.4.2, the position of the conduction band edge must be convenient to fully reduce water to H_2.

In section 2.5.1, the band bending of the semiconductors has been discussed. When a semiconductor is brought into contact with an electrolyte solution, the Fermi level of the semiconductor will equilibrate with the electrochemical potential of the liquid through transferring charge across the interface. In the case of a p-type semiconductor, the band bending will occur in the way that the photogenerated electrons float toward the interface, while holes are moved into the bulk of the solid. Hence it will be expected that the photoexcitation drives electrons from the solid into the solution (see Figure 2.10). In some way, this cathodic current could protect the surface of the semiconductor from the oxidation. Based on this fact, p-type semiconductors are the best option as photocathodes for the hydrogen evolution. Searching literature reveals some of the p-type semiconductors (such as p-GaP, p-InP, p-Si) which have been applied in the PEC system as photocathodes [49].

Jägermann *et al.* [32] investigated the photoelectrochemical behavior of the FeS_2 electrode. They expected that n-FeS_2 is able to produce O_2 as RuS_2 since they
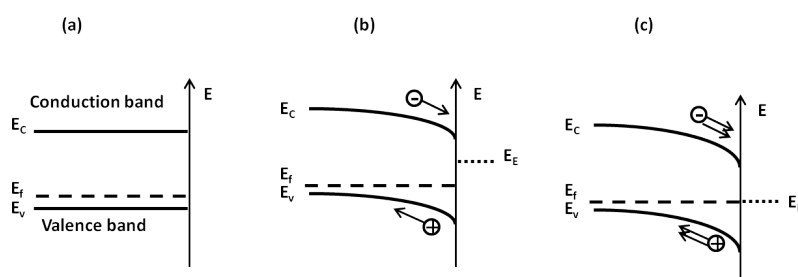

Figure 2.10: Schematic illustration of energy levels of a p-type semiconductor (a), a p-type semiconductor in contact with a liquid; (b) before equilibrium, (c) after equilibrium.

have the same structure. According to their results at the positive potential only a corrosion to $SO_4{}^{2-}$ was observed and no O_2 was produced. Further studies were performed by Ennaui *et al.* [33]. They demonstrated the operation of a PEC cell based on FeS_2 with high photocurrent efficiency and reported the interesting role of the $I^-/I_3{}^-$ redox couple in the charge transfer reaction. As an iron based material, pyrite is an interesting material and could be considered as an electrode in the photoelectrochemical cells. This is due to its excellent properties such as being an abundant and a nontoxic material, exhibiting a very good photoabsorption characteristics, and suitable band gap making pyrite possible to absorb a significant portion of the solar spectrum [16, 30, 33–35] (more information about pyrite in section 2.3).

However one of the big challenges of using this material in PEC or PC system is its photocorrosion during the illumination. Pyrite electrodes in contact with water and under illumination photocorrode via hole transfer corresponding to the following overall reaction [30]:

$$FeS_2 + 8\,H_2O + 15\,h^+ \xrightarrow{\ h\nu\ } Fe^{3+} + 2\,SO_4{}^{2-} + 16\,H^+ \qquad (2.5)$$
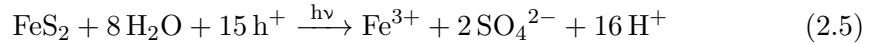
Due to this reaction, it is not easy to have a stable system during the illumination. In most cases, the stability of the system depends on the surface properties of the pyrite electrode and the possibility of stabilization of the interface of the electrode, e.g. in the presence of electron donor reagents [30, 50].

In the present study the photoelectrochemical behavior of pyrite electrodes has been studied to find out whether this material could be a good candidate as a photocathode in a PEC cell.

2.6 Photocatalytic Water Splitting

The search for highly efficient and affordable semiconductor based photocatalysts for the water splitting is an ongoing quest. Besides this point, developing new strategies and modifying the operating system could also influence the efficiency of the reaction. In this section first, two of these strategies will be introduced, which have been used in the present study to improve the activity of the photocatalyst (hematite or pyrite). The following subsections are describing various PC water splitting systems.

In principle, there are three different systems for PC water splitting: a single

photocatalyst water splitting system (or one-step excitation), a Z-scheme overall water splitting system (or two-step excitation) and water splitting system in the presence of sacrificial reagents (electron or hole scavengers).

2.6.1 Co-catayst Loading

One of the issues affecting the efficiency of the photocatalytic reaction is the charge carrier recombination. Therefore the strategy to improve the photocatalytic activity must be based on the efficient separation of the photogenerated charges to avoid bulk/surface charge recombination and transfer to the separated active sites on the surface of the photocatalyst. This could also inhibit the backward reaction of hydrogen and oxygen to produce water.
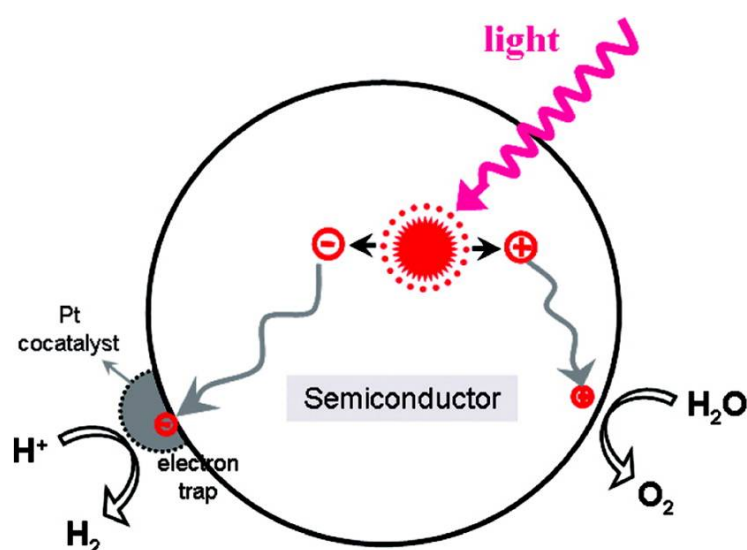
Figure 2.11: Processes of charge transfer between semiconductor photocatalyst and co-catalyst, in the example of Pt as co-catalyst. Reprinted with permission from [51], ©2010 American Chemical Society.

Some transition noble metals (such as Pt[52, 53], Rh[52, 53] and Au[54–56]) and metal oxides (such as NiO [57, 58] and RuO_2 [59–61]) are widely used as effective co-catalysts for photocatalytic water splitting. Pt [56, 58, 62] is one of the most applied noble metal co-catalyst in different photocatalytic water splitting systems. The charge separation and transfer process between the co-catalyst (here Pt) and the photocatalyst are depicted in Figure 2.11. To explain how the co-catalysts loading could help these processes, it should be considered that usually, the Fermi levels of these noble metals are lower than that of the semiconductor photocatalyst.

In this way the photogenerated electrons can be transferred to the surface of the photocatalyst and will be trapped by the noble metal co-catalyst, while the photogenerated holes remain at the photocatalyst and migrate to its surface. These facts reduce the possibility of the electron-hole recombination whereby an efficient separation of the photogenerated electrons and holes can be achieved [51]. This
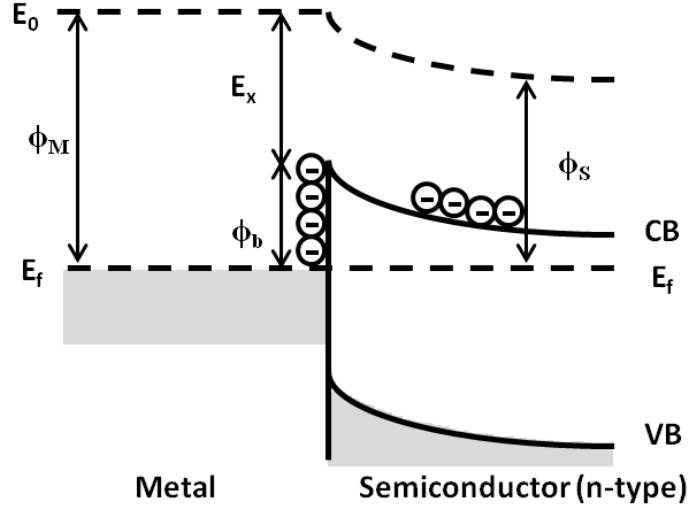
Figure 2.12: Schematic illustration of the Schottky barrier formation at the metal-semiconductor interface in equilibrium. E_0: vacuum level, E_F: Fermi level, Φ_M: work function of the metal, Φ_S: work function of the semiconductor, Φ_b: Schottky barrier height.

explanation is represented in the illustration of the formation of a Schottky barrier at the metal-semiconductor junction as shown in Figure 2.12. Separately and before contact, the metal and an n-type semiconductor have different Fermi level positions and as Figure 2.12 depicts metal has a higher work function (Φ_M) than the semiconductor (Φ_S). When they are brought together after contact, the electrons will migrate from the semiconductor to the metal and this continues until the two Fermi levels are aligned. Due to this contact, a space charge layer develop. Furthermore, the surface of the metal raises an excess of electrons while an excess of positive charge occurres on the surface of the semiconductor since the electrons migrate from the barrier region. As a result, the semiconductor bands bend upwards toward the surface, and the layer is said to be depleted. The formed barrier at the metal-semiconductor interface is called the Schottky barrier and the height

of the barrier (Φ_b) is given according to the following equation:

$$\Phi_b = \Phi_M - E_x \tag{2.6}$$

Here E_x is the electron affinity and usually measured from the conduction band edge to the vacuum level of the semiconductor [63].

It should be considered that due to the noble metal loading the charge recombination will be reduced but the water splitting remains still difficult. This is due to the facts that the recombination cannot be completely suppressed and the backward reaction of H_2 and O_2 to form H_2O is thermodynamically favorable [48].

In water splitting, the backward reaction must be suppressed because of the negative $\Delta G°$ of water formation reaction (-237.2 $kJ\,mol^{-1}$). The transition metal oxide co-catalysts (such as NiO, RuO_2, and IrO_2) seem to be able to produce active sites for H_2 or O_2 evolution. These could block the charge carrier recombination and enhance the photocatalytic activity. According to the literature, metal oxide co-catalysts, such as NiO, are able to improve the activity with efficient charge separation for water splitting and suppressing the backward reaction.

Finally, it should be noted that some of the co-catalysts are better for the H_2 evolution reaction and others for the O_2 evolution reaction. For example, Pt is well-known as a H_2 evolution co-catalyst [5, 64] while IrO_2 is well-known as O_2 evolution co-catalyst [5, 59, 65].

2.6.2 Nanoscale Effect

Nanostructured photocatalysts and photoelectrodes are recently becoming very popular [46, 47, 66]. The reason for this is that recent investigations assumed that nanoscaling leads to the improvement of the catalytic properties over the bulk forms [67, 68]. The fact is that nanoscale photocatalysts have several advantages for water splitting reaction over the bulk ones. This is due to the following aspects: nanostructured photocatalysts have a large surface area thereby increasing the number of the catalytic sites for water splitting. Nanoscaling also leads to shorter diffusion lengths for charge carriers to reach the surface. It is also possible to profit from the quantum size effect among the nanoparticulate materials and adjust the band gap of the material. With increasing the band gap, the conduction band edge shifts to more reducing and the valence band to more oxidizing potentials. Nanoscaling also affects the light distribution. The absorption of the incident light is better for films with the thickness in the nm range. The light harvesting

is also better in micro- or nanoscale materials, due to the scattering of the light in the colloidal suspension the light is mostly trapped in the suspension [11, 69, 70].

The advantages of nanomaterials for solar energy conversion were demonstrated by several groups [11, 59, 60, 69, 71–74]. For example, Grätzel's group reported on nanostructured dye-sensitized photoelectrochemical cell [72] or using nanolayers [73] or nanoparticles [74] in PEC systems. In the literature some examples for improving the photocatalytic water splitting exist due to the nanoscaling effect. Saito *et al.* reported about $LiNbO_3$ nanowires which are prepared via a metal complex-based strategy. The photocatalytic performance of obtained nanowires ($70\,nm \times 10\,\mu m$, $E_g = 4.0\,eV$) was enhanced in comparison with the bulky $LiNbO_3$ [75]. In another example Yan *et al.* reported about overall water splitting over Zn_2GeO_4 nanorods ($100\,nm \times 150\,nm$). These nanorods improved the PC water splitting performance and photoreduction of CO_2. The authors supposed that this leads to the reduced number of crystal defects, high specific surface area and beneficial microstructure on the catalyst's surface [76]. One of the most active nanoscale photocatalysts was reported by Yokoi *et al.* in 2011. The authors reported about NiO-loaded $NaTaO_3$ nanoparticles. Their investigations indicate that the photocatalytic activity for overall water splitting reaction ($2.0\,\mu mol\,h^{-1}$ of H_2 with stoichiometric O_2) was three times higher than non-structured bulk $NaTaO_3$ particles [77].

Besides all of the advantages nanostructured photocatalysts have also significant disadvantages that might hinder the activity and efficiency of the photocatalytic reaction. Some of these disadvantages are summarized as follows: the large surface area promotes the defect recombination. Since nanostructured photocatalysts exhibit larger specific interfacial areas, the surface and the interfacial recombination rates will also be increased. The generation of the space charge layer in the colloidal nanoparticles is different from that in the large particles. The electrical field in small semiconductors is usually small so that high dopant levels are required to produce a significant potential difference between the surface and the surface of the particles [79].

The charge carrier separation in the nanoparticles is more complicated to achieve than in the bulk because at the average doping concentrations the space charge layers are not effective on the nanoscale. Figure 2.13 shows a comparison between the space charge layers in large and small particles. Generally, the space charge layer thickness d_{SC} of spherical nanoparticles cannot be much greater than the radius $d/2$ of the particles and this fact confines the possible barrier height at the interface. For example, O'Regan *et al.* [80] calculated for $16\,nm$ TiO_2 nanoparticles with a
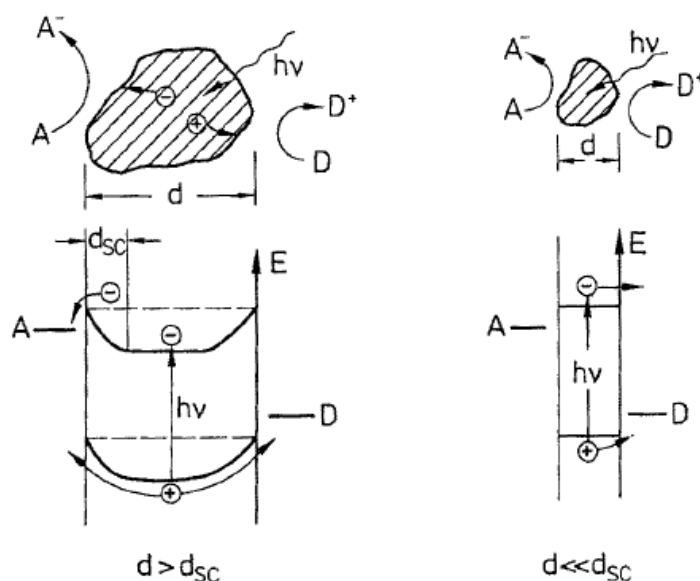
Figure 2.13: Illustration of the space charge layers in large (left) and small (right) particles, A: electron acceptor and D electron donor. Reprinted with permission from [78], ©1994 Springer, Berlin, Heidelberg.

dielectric constant and ionized donor concentration values of 130 and $10^{17} \, \mathrm{cm}^{-3}$ respectively, a barrier height of $0.3 \, \mathrm{mV}$ under maximum depletion. This resulted in essential flat bands in nanoparticles as is noticeable in Figure 2.13 for the nanoparticles in absence of a strong applied bias [11, 69, 78, 80].

2.6.3 Single Photocatalyst Water Splitting System

Basically, overall water splitting with a photocatalyst which exhibits a suitable band gap for this reaction should be possible (more details are given in section 2.4.2). However, most semiconductors and even TiO_2 are not able to split water without modifications such as loading with co-catalysts [81]. Figure 2.14 illustrates overall water splitting over the active sites (co-catalysts). Some of the reported photocatalysts which split water under UV illumination with co-catalyst modifications are: $Pt/RuO_2/TiO_2$ [59], $NiO/NaTaO_3$ [83–85], $Pt/Sr_2Nb_2O_7$[86], and $NiO/Sr_2Nb_xTa_{2-x}O_7$ [87]. One of the best performance of the photocatalytic overall water splitting has been reported by Kato *et al.* in 2003 [85]. They doped NiO-loaded $NaTaO_3$ with lanthanum (with different wt% of NiO and mol % of La) and illuminated with UV light. They observed stoichiometric H_2 and O_2 evolution
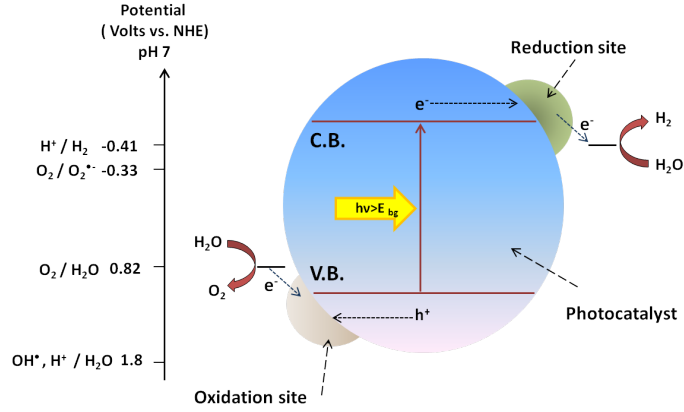
Figure 2.14: Schematic illustration of photocatalytic water splitting by a single photocatalyst over the active sites (co-catalysts), the values of one-electron couples are taken from [82].

and the maximum quantum yield has been reported to be 56% at 270 nm. Altogether, these efficient photocatalysts are UV light active and to harvest the solar light, effective visible light active photocatalysts should be considered [88].

Some of the visible light active photocatalysts are presented in Figure 2.5. Theoretically visible active photocatalysts such as CdS, CdSe, and ZnS seem to have suitable band positions for water splitting. However, CdS and CdSe are not able to produce H_2 and O_2. Furthermore, it is well known that these materials prone to photocorrosion in the photocatalytic reaction where CdS (or CdSe) itself will be oxidized by the photogenerated holes according to the following reaction [5, 81, 89]:

$$CdS + 2\,h^+ \longrightarrow Cd^{2+} + S \tag{2.7}$$

Photocorrosion has also been reported in case of ZnO in the absence of noble metal co-catalysts (h^+: photogenerated holes) [5, 81]:

$$ZnO + 2\,h^+ \longrightarrow Zn^{2+} + \frac{1}{2}\,O_2 \tag{2.8}$$
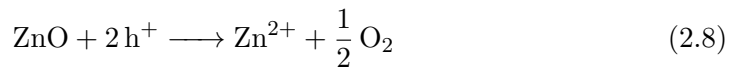
2.6.4 Z-scheme Overall Water Splitting System

Clearly, overall water splitting via a single photocatalyst has significant challenges. On the other hand, the Z-scheme water splitting systems could solve some of the issues regarding the overall water splitting via a single photocatalyst. Figure 2.15 illustrates the basic principles of the overall water splitting by two photocatalysts
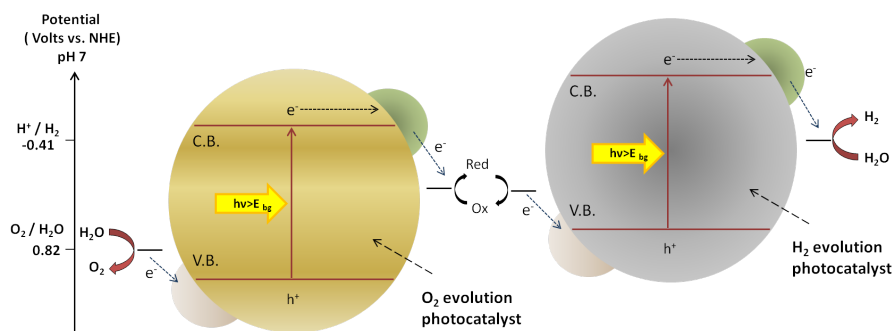
Figure 2.15: Schematic illustration of basic principle the overall water splitting by two photocatalysts in the Z-scheme system including the shuttle redox mediator.

in the so-called Z-scheme system. With this system, it is possible to employ the narrow band gap materials and most importantly visible light active materials such as WO_3, Fe_2O_3, and FeS_2. Either the valence band or the conduction band position of these semiconductors is not suitable for H_2 or O_2 evolution reaction. Thus, the best strategy will be to combine two visible light active photocatalysts whereby one of them is able to produce H_2 and the other one is able to produce O_2 (Figure 2.15). The system was introduced by Bard in 1979 [90] based on the inspiration from the natural photosynthesis of green plants. Later on, the system has been developed using different photocatalysts and employing suitable shuttle redox mediators [88, 91, 92].

In a Z-scheme system, each photocatalyst is just proper for a half-reaction of water splitting. Therefore, this system is not only expanding the scope of applying photocatalysts with improper band edge position for water splitting but also is capable of separating the active sites of each reaction (H_2 or O_2 production) thus suppressing the backward reaction of hydrogen and oxygen to produce water. One critical issue of the Z-scheme water splitting is the backward reaction involving redox mediators which is thermodynamically more favorable than water splitting. Therefore, it is important to construct photocatalytic systems with high selectively for the forward reactions.

Nowadays Z-scheme systems are popular and extensively investigated. Some of the investigated Z-scheme water splitting systems were reported by the Domen group [6, 64, 93, 94]. For example, they investigated Z-scheme systems with two different semiconductor photocatalysts using a modified ZrO_2/TaON species (as H_2 evolution photocatalyst) and various O_2 evolution photocatalysts with shuttle
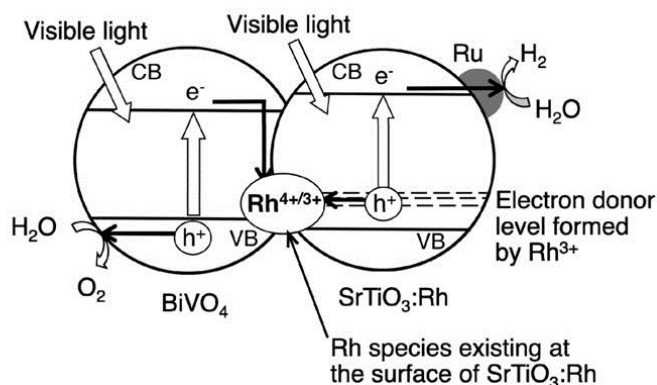
Figure 2.16: Mechanism of water splitting using Ru/SrTiO$_3$:Rh as H$_2$ evolution photocatalyst and BiVO$_4$ as O$_2$ evolution photocatalyst in a Z-scheme photocatalysis system driven by electron transfer between H$_2$- and O$_2$- photocatalysts. Reprinted with permission from [95], ©2009 American Chemical Society.

redox mediators. The best result under the optimal condition has been reported for a system with Pt/ZrO$_2$/TaON (for H$_2$ evolution), Pt/WO$_3$ (for O$_2$ evolution), and IO$_3^-$/I$^-$ as the shuttle redox mediator. In this system, an apparent quantum yield of 6.3% at 420.5 nm has been reported [64].

It is also possible to have Z-scheme water splitting without the shuttle redox mediator to avoid undesired backward reactions or a filter effect due to absorption by the redox mediator. For example Sasaki *et al.* [95] have reported about a system with Ru/SrTiO$_3$:Rh (for H$_2$ evolution) and different photocatalysts for O$_2$ evolution such as BiVO$_4$ and WO$_3$. In addition, they proposed a mechanism for the Z-scheme water splitting including interparticle electron transfer between the two photocatalysts over Rh species (with reversible oxidation number) existing at the surface of SrTiO$_3$:Rh (see Figure 2.16) .

2.6.5 Photocatalytic H$_2$ or O$_2$ Evolution in Sacrificial Systems

One of the main strategies to check the activity of a photocatalyst or to test if a photocatalyst is suitable for H$_2$ or O$_2$ evolution is to carry out the reaction in the presence of suitable sacrificial reagents. These sacrificial reagents are usually various kinds of inorganic ions (such as S^{2-}/SO$_3^{2-}$, I$^-$, Ag$^+$ or Fe^{3+}) or organic compounds (such as pollutants) which act as electron donors or acceptors, respectively. These reagents are called "sacrificial reagents" since they will be consumed during the
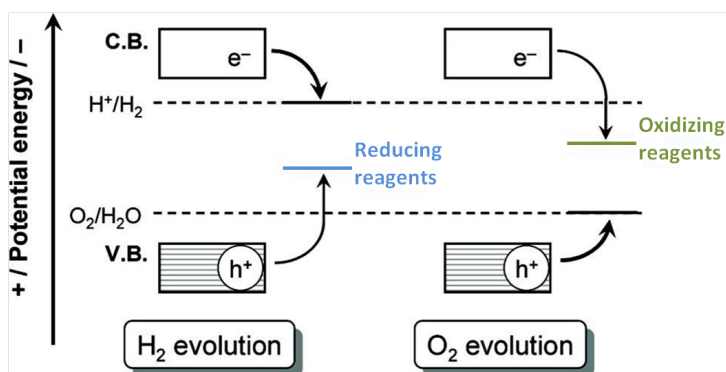
Figure 2.17: Illustration of the basic principle of photocatalytic H_2 and O_2 evolution in presence of suitable reducing and oxidizing reagents. Adapted with permission from [40], ©2007 American Chemical Society.

photocatalytic reaction [88, 96].

Expectedly the system will be involved in the production of H_2 or O_2. Therefore, these tests give the opportunity to improve the photocatalytic hydrogen or oxygen generation rates. Figure 2.17 illustrates the basic principle of photocatalytic H_2- and O_2- production applying sacrificial reagents. In presence of reducing reagents (also called electron donors or hole scavengers) in the photocatalytic reaction, the photogenerated holes oxidize the reducing reagents instead of water. Thereby, the photogenerated electrons will be accumulated in the conduction band of the photocatalyst and improve the H_2 production rate. In the other case, in presence of oxidizing reagents (also called electron acceptors or electron scavengers), photogenerated electrons reduce the oxidizing reagents instead of water [40, 88].

Even though in the illustration in Figure 2.17 the band edges of the photocatalyst seem to be suitable for overall water splitting, these systems are also suitable for the photocatalysts where just one of the band edges is suitable for water oxidation or reduction. Generally, it should be considered, that these systems are just involved with one of the half reaction of the water splitting, therefore the term of "water splitting" is not suitable for these reactions.

Commonly used hole scavengers for H_2 evolution reaction are alcohols [81, 97–101] and sulfide ions [51]. In present work S^{2-}/SO_3^{2-} have been employed as the hole scavengers. These sacrificial reagents are widely used in case of CdS as the photocatalyst for H_2 production[48, 89, 102–104]. Photocorrosion is one of the main issues of using CdS as the photocatalyst. CdS will be photocorroded according to the reaction 2.7.

In presence of the reducing reagents such as S^{2-} and $SO_3{}^{2-}$, first the holes could react with the S^{2-} to form S (reaction 2.9), subsequently S could react with $SO_3{}^{2-}$ and produce $S_2O_3{}^{2-}$ (reaction 2.10), in order to prevent any detrimental deposition of S onto CdS [48, 103].

$$S^{2-} + 2\,h^+ \longrightarrow S \tag{2.9}$$

$$S + SO_3{}^{2-} \longrightarrow S_2O_3{}^{2-} \tag{2.10}$$
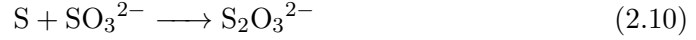
On the contrary to the reported suitable hole scavengers for the H_2 evolution reaction, the variety of electron scavengers for O_2 evolution reaction are limited. Silver (Ag^+) is one of the widely used electron acceptors [81, 105–107]. Beside of silver cations, iron cations are also common in O_2 evolution reactions [108–110]. In the present study ferric ions (Fe^{3+}) have been employed as the electron scavengers to produce molecular oxygen according to reaction 2.11 and reaction 2.12. Here the photogenerated holes oxidize water to O_2 while photogenerated electrons reduce Fe^{3+} to Fe^{2+}:

$$2\,H_2O + 4\,h^+ \xrightarrow{\ h\nu\ } O_2 + 4\,H^+ \tag{2.11}$$

$$4\,Fe^{3+} + 4\,e^- \xrightarrow{\ h\nu\ } 4\,Fe^{2+} \tag{2.12}$$
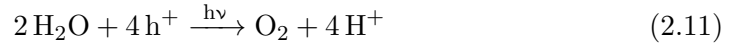
In 2013 Schneider and Bahnemann published a critical article about the undesired role of the sacrificial reagents [111]. In this article, first, the authors discussed in detail the role of sacrificial organic electron donors such as methanol or any alcohol which exhibits a hydrogen atom at the carbon atom in the α-position to its OH group. Generally, it is expected that the H_2 formation from the photocatalytic oxidation of the methanol is carried out by the photogenerated electrons in the photocatalyst (for example TiO_2). However due to a process called "current doubling effect", it is possible that half of the produced H_2-gases are formed through the action of holes and not that of electrons. And therefore the overall efficiency of the H_2 formation reaction could be limited by the initial hole transfer to the sacrificial reagent [78, 112].

Furthermore, the authors discussed the role of sacrificial inorganic electron donors such as sulfide (S^{2-}) and sulfite ($SO_3{}^{2-}$). As mentioned, these sacrificial reagents are widely used in H_2 production systems employing CdS as the photocatalyst. In the literature different supposed mechanisms for the hydrogen production in the presence of $S^{2-}/SO_3{}^{2-}$ exist. One of these mechanisms is discussed by Jang *et al.* [103] and mentioned above (reaction 2.9 and 2.10). However, Bao *et al.* [113] supposed a different mechanism for this reaction using a Pt-loaded CdS photocatalyst

and suggested a mixture of SO_4^{2-}, $S_2O_6^{2-}$, $S_2O_3^{2-}$ and S^{2-} as the products of this reaction. The proposed reaction mechanism for the H_2 production in a mixture of S^{2-}/SO_3^{2-} is summarized as follows:

$$2\,H_2O + 2\,e^- \longrightarrow H_2 + 2\,OH^- \tag{2.13}$$

$$SO_3^{2-} + 2\,OH^- + 2\,h^+ \longrightarrow SO_4^{2-} + H_2O \tag{2.14}$$

$$2\,SO_3^{2-} + 2\,h^+ \longrightarrow S_2O_6^{2-} \tag{2.15}$$

$$2\,S^{2-} + 2\,h^+ \longrightarrow S_2^{2-} \tag{2.16}$$

$$SO_3^{2-} + S^{2-} + 2\,h^+ \longrightarrow S_2O_3^{2-} \tag{2.17}$$

$$S_2^{2-} + SO_3^{2-} \longrightarrow S_2O_3^{2-} + S^{2-} \tag{2.18}$$
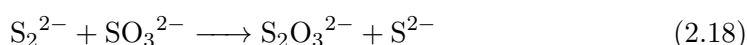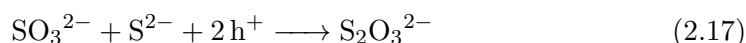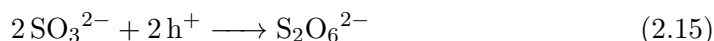
Generally, the oxidation of S^{2-} and SO_3^{2-} can either be carried out by a two-electron transfer process or even through the thermodynamically less favorable one-electron oxidation, which will form two powerful reducing agents as free radical intermediates, i.e. $S^{-\bullet}$ (E^0 = -1.7 V vs. NHE) and $^{\bullet}SO_3^-$ (E^0 = -2.4 V vs. NHE) [81, 111]. Based on this fact and various proposed mechanisms suggested by different authors, it could be expected that different reactions and products are involved in the photocatalytic oxidation of sulfide and/or sulfite in aqueous semiconductor suspensions.

In most investigations only the H_2 production is reported and there are no experiments involving the analyses of the reaction mixture and clarifying the role of used sacrificial reagents [89, 104, 114]. It is very important to understand from either the direct reductive or the indirect oxidative pathways the H_2 will be formed.

The deficiency of explanation of the role of the sacrificial reagents exists not only in the case of electron donors but also for the electron acceptors too. As mentioned, silver cations (Ag^+) is one of the widely used electron acceptors in the O_2 evolution reactions. It is supposed that the O_2-evolution reaction occurs in the presence of Ag^+ as follows:

$$2\,H_2O + 4\,h^+ \xrightarrow{h\nu} O_2 + 4\,H^+ \tag{2.11}$$

$$4\,e^- + 4\,Ag^+ \xrightarrow{h\nu} 4\,Ag^0 \tag{2.19}$$

$$n\,Ag^0 \xrightarrow{h\nu} Ag_n^{\ 0} \tag{2.20}$$
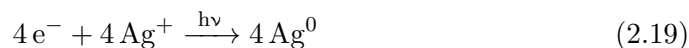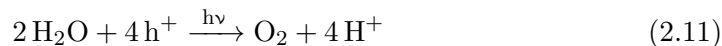
The O_2 evolution could also be performed in presence of ferric ions (Fe^{3+}) as sacrificial electron acceptors. As mentioned this procedure proceeds according to the

reactions 2.11 and 2.12.

However, the O_2 evolution reactions could not perform when reagents such as CCl_4 or $C(NO_2)_4$ are used as the electron acceptors. This fact means that these active electron acceptors are not suitable for the O_2 evolution reaction, introducing the question of why Ag^+ and Fe^{3+} are capable of performing this reaction. Furthermore, it is not clear if Ag^+ and Fe^{3+} are involved in the water oxidation reaction.

If it is considered that the photogenerated holes are capable of performing following one-electron oxidation and oxidize Ag^+ and Fe^{3+}(reactions 2.21 and 2.22), then it is obviously not clear whether the produced O_2-gases are only due to the water oxidation reaction.

$$h^+ + Ag^+ \longrightarrow Ag^{2+} \tag{2.21}$$

$$h^+ + Fe^{3+} \longrightarrow Fe^{4+} \tag{2.22}$$
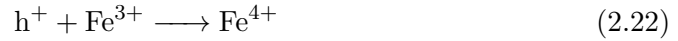
Ag^{2+}-species could produce Ag_2O_2 in aqueous solution according to the following reaction:

$$2\,Ag^{2+} + 2\,H_2O \longrightarrow Ag_2O_2 + 4\,H^+ \tag{2.23}$$
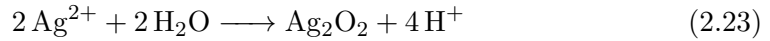
And Ag_2O_2 could react with the photogenerated holes from the photocatalytic reaction and produce O_2 according to the following reaction:

$$Ag_2O_2 + 2\,h^+ \longrightarrow 2\,Ag^+ + O_2 \tag{2.24}$$
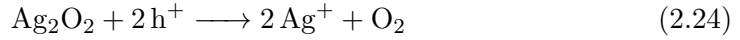
Similar to the above-mentioned reactions, Fe^{4+} could also undergo an oxidation reaction and produce O_2 based on the following reactions:

$$Fe^{4+} + h^+ \longrightarrow Fe^{5+} \tag{2.25}$$

Fe^{4+} could be further oxidized:

$$2\,Fe^{5+} + 2\,H_2O \longrightarrow [Fe_2O_2]^{6+} + 4\,H^+ \tag{2.26}$$

$$[Fe_2O_2]^{6+} \longrightarrow 2\,Fe^{3+} + O_2 \tag{2.27}$$
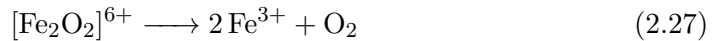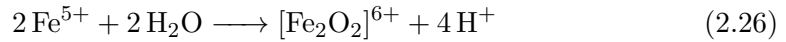
Based on these aspects, the role of metal cations such as Ag^+ and Fe^{3+} in the photocatalytic O_2 evolution systems should carefully be defined since they are able to perform other reactions (reactions 2.21-2.27) besides being the electron scavenger in the system.

3 Materials, Analytical and Experimental Methods

This Chapter is divided into four sections. The first section deals with the preparation methods of the nanoparticles and electrodes followed by the section of the characterization of these samples. The last two sections deal with the photoelectrochemical and photocatalytical tests on these samples.

3.1 Materials

Three types of semiconductors have been studied: iron oxide Fe_2O_3, iron disulfide FeS_2 and titanium dioxide TiO_2. Each of them were either purchased commercially (see table 3.1) or prepared according to published synthesis methods. Fe_2O_3 and FeS_2 electrodes have been prepared for photoelectrochemical investigations. All chemicals were purchased from Sigma Aldrich and were used as received without further purification. All aqueous solutions were prepared with deionized water from a SARTORIUS ARIUM 611 apparatus (resistivity = 18.2 MΩ·cm).

Table 3.1: Commercial photocatalysts used in this work

Material	Crystal structur	Supplier
Fe_2O_3 (20-40 nm)	Hematite	io-Li-tec Germany
FeS_2(325 mesh)	Pyrite	Sigma-Aldrich
TiO_2 Aeroxide P25 (21 nm)	30% Rutile and 70% Anatase	Evonik Germany
TiO_2 Hombikat UV100 ($\leq$10 nm)	100% Anatase	Huntsman Germany

3.1.1 Preparation of Hematite (α-Fe_2O_3) Nanoparticles

α-Fe_2O_3 nanoparticles have been prepared from inorganic precursors according to Faust *et al.*[115]. In a typical synthesis, 100 mL of 0.1 M aqueous iron (III) chloride (prepared from $FeCl_3$ or $FeCl_3 \cdot 6\,H_2O$) were added dropwise into 400 mL vigorously stirred boiling water. The solution was refluxed for 1 h and subsequently cooled

in an ice bath. The resulting colloidal suspension had a dark red color and was extremely acidic based on the following reaction:

$$2\,FeCl_3 + 3\,H_2O \longrightarrow Fe_2O_3 + 6\,HCl \tag{3.1}$$
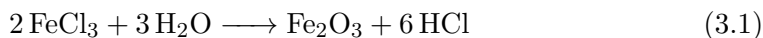
The colloidal Fe_2O_3 suspension was dialyzed against deionized water using a dialysis tube (Medicell International, MWCO 12000-14 000). The suspension was dialyzed at least for three days changing the deionized water several times until the electrical conductivity had reached a value below $2\,\mu S\,cm^{-1}$ (measured via Qcond 2200 from VWR) and the pH was ≥ 6. Finally, the colloid was freeze-dried by an ALPHA 1-4 LSC Freeze Dryer and a dark red Fe_2O_3 powder was obtained.

3.1.2 Preparation of Pyrite (FeS$_2$) Nanoparticles

Pyrite (FeS_2) nanoparticles have been prepared according to a method published by Bai *et al.*[116]. This synthesis method was very sensitive to the presence of O_2. Therefore the synthesis was carried out under constant N_2-flow in a round three-neck flask. In this flask 0.259 g of iron (II) chloride tetrahydrate ($FeCl_2 \cdot 4\,H_2O$, 99%) (1.30 mmol) were dissolved under purging with N_2 in 90 mL of dimethyl sulfoxide (DMSO) containing $361\,\mu L$ thioglycolic acid (TGA, 99%). The solution was stirred under N_2 purging and finally yielded a green color. After 30 min, 10 mL of an aqueous sodium thiosulfate pentahydrate ($Na_2S_2O_3 \cdot 5\,H_2O$, 99.5%) solution (5.85 mmol) were added dropwise to the reaction mixture under N_2 atmosphere. The color of the solution quickly changed from green to brown. Subsequently, the reaction mixture was brought to the boiling temperature and refluxed under N_2 atmosphere. Thereby, the resulting colloidal suspension changed the color from brown to dark gray. The nanocolloids were allowed to grow and crystallize under continuous reflux at a temperature around $412\,K$ for 2-8h. The reflux time affected the size of the resulting nanoparticles. The products were separated from the reaction media by centrifugation and washed several times with ethanol and deionized water. The final products were dried in vacuum at $334\,K$ for 5h. The resulting powder had a gray color. The chemicals used for the synthesis of the pyrite nanoparticles are presented below (see Table 3.2).

Table 3.2: Chemicals for the synthesis of the pyrite nanoparticles

Chemicals	Molecular weight $[g\,mol^{-1}]$	Mol [mmol]	Mass [g]	Volume [mL]	Equivalents
$FeCl_2 \cdot 4\,H_2O$	198.18	1.3	0.25	-	1
$Na_2S_2O_3 \cdot 5\,H_2O$	248.18	5.8	1.45	-	4.5
$HSCH_2COOH$	92.12	5.2	-	0.361	4
$(CH_3)_2SO$	78.13	1267	-	90	975
H_2O	18.01	555	-	10	427

3.1.3 Preparation of Colloidal Platin (Pt) Nanoparticles

Nobel metal nanoparticles like Pt were used as co-catalysts in this work. In some cases, colloidal Pt was used to modify FeS_2- or Fe_2O_3- photocatalyst. The colloidal Pt particles were thermally prepared by reducing $H_2PtCl_6 \cdot 6\,H_2O$ solution with sodium citrate according to Brugger *et al.* [117]. 6 mL of a sodium citrate solution $(20\,mg\,L^{-1})$ was added to 23.4 mL of a boiling 0.001 M solution of $H_2PtCl_6 \cdot 6\,H_2O$. Subsequently, the mixture was refluxed for 4 h. The colloid was cooled at room temperature and dialyzed against deionized water (using the dialysis tube) until the electrical conductivity had a value below $5\,\mu S\,cm^{-1}$.

3.1.4 Loading of FeS$_2$-Nanoparticles with Pt

The synthesis method of pyrite (section 3.1.2) was modified to load pyrite nanoparticles (FeS_2) with platinum (Pt). For this purpose, first the synthesis described previously was carried out. After a reaction time of two hours, the desired amount of the colloidal platinum solution (described in section 3.1.3) was added. Subsequently, the reaction mixture was refluxed under nitrogen for further 1 h. The suspension was slowly cooled down and allowed to stand overnight under an inert gas (N_2). The separation and drying procedures were applied here as previously described in section 3.1.2 for pyrite nanoparticles.

3.1.5 Preparation of Co-Cat/FeS$_2$ and Co-Cat/α-Fe$_2$O$_3$

Pyrite powder (FeS_2 99.8% trace metals basis 325 mesh) and hematite powder (α-Fe_2O_3 99.5% 20-40 nm) were procured from Sigma Aldrich and Ionic Liquid Technologies, respectively. The in situ metal photodeposition, as well as the metal

impregnation on FeS_2 or Fe_2O_3, were carried out as reported elsewhere [85].

Noble metal loading: Briefly, the in situ photodeposition of noble metals on the surface of FeS_2 or Fe_2O_3 was performed via a photoreduction reaction from aqueous solutions containing the desired concentrations of $H_2PtCl_6 \cdot 6\,H_2O (\geq 37.50$ % Pt basis) and $HAuCl_4 \cdot 3\,H_2O$ (≥ 49.00 % Au basis) to obtain 0.5 wt% of the appropriate metal loading.

Metal oxide loading: Metal oxide co-catalysts were loaded onto FeS_2 or Fe_2O_3 by an impregnation method employing the corresponding aqueous solutions containing the desired concentrations of $Co(NO_3)_3 \cdot 6\,H_2O$, $Cu(NO_3)_2 \cdot 3\,H_2O$, $IrCl_3 \cdot xH_2O$, $K_2Cr_2O_7$, $RuCl_3 \cdot xH_2O$ and Ni_2O_3 to obtain 0.5 wt% of the appropriate metal oxide loading. FeS_2 or Fe_2O_3 was thoroughly mixed with the above mentioned precursor solutions of the proper concentration followed by a thermal treatment at 534 K for 1h in air to form the desired metal co-catalyst.

3.1.6 Preparation of α-Fe$_2$O$_3$ Electrodes

The preparation of the α-Fe_2O_3 electrodes (photo-anode) was performed as follows. First a transparent colloidal suspension of α-Fe_2O_3 was prepared according to Faust *et al.* (section 3.1.1) and dip-coated on Fluorine-doped tin oxide (FTO) glass slides. The FTO glass was purchased from Sigma Aldrich with a dimension of 300 mm × 300 mm × 3.2 mm and a surface resistivity $\sim$ 8 Ω/sq. The FTO glass slides were cut to 30 mm × 30 mm pieces and cleaned with detergent solution, immersed in ethanol in an ultrasonic bath for 15 min, rinsed with deionized water and then dried in air at 353 K. The FTO glass was taped with an adhesive tape that just a surface area of 20 mm × 20 mm of the conductive site of the FTO was available for the coating.

The α-Fe_2O_3 colloidal suspension was coated on FTO at room temperature using a dip-coater with an immersion speed of $30\,cm\,min^{-1}$ and a withdrawal speed of $12\,cm\,min^{-1}$. During each dipping the substrate remained in the suspension for 2 s and was subsequently dried for 2 min at room temperature. This dipping and drying procedure was repeated for twelve cycles to obtain the expected thickness of the deposited substrate. The resulting films were calcined in an oven at different temperatures for 1 h.

3.1.7 Preparation of FeS$_2$ Electrodes

For the preparation of pyrite electrodes (photo-cathode), FeS$_2$ powder (table 3.1) and natural single crystal were used.

FeS$_2$ Electrodes from natural Pyrite:

The natural crystal came from Navajun Spain and had a cubic form (Figure 3.1). The crystal was cut into slices with a thickness of approximately 1 mm along the planes of the cubic lattice with a surface area of 30 mm × 30 mm. The surfaces were polished and cleaned with deionized water. The surface did not go through further etching, since there should not be any differences between the photochemical behavior of an etched and a natural one (according to Jaegermann *et al.* [32]).
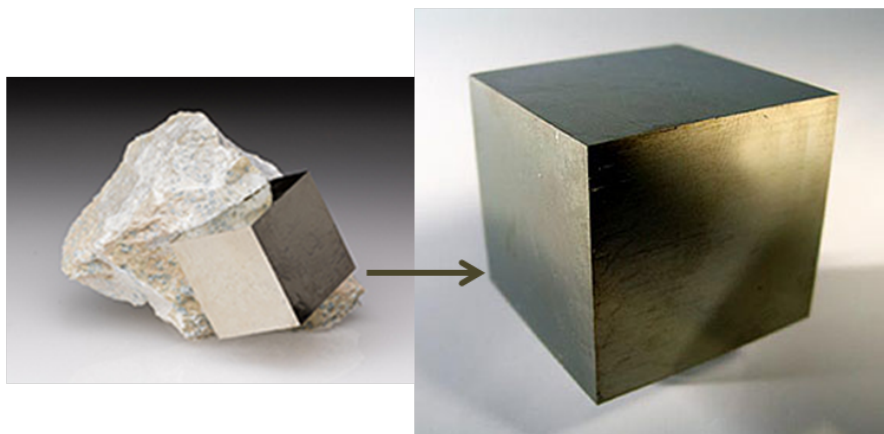
Figure 3.1: Pyrite mineral

FeS$_2$ Eectrodes from Doctor Blade Method:

The pyrite photocathodes were prepared based on the Doctor Blade method. The pastes for this method were prepared according to a procedure published for the screen printing of TiO$_2$ [118]. Figure 3.2 shows this procedure using the commercially available FeS$_2$ powder. The FTO glass used as the substrate was cleaned and prepared as described in section 3.1.6. A layer of paste was coated on the FTO glass plates by doctor blading. Subsequently the Films were heated at 400 °C (or 500 °C) in air for 1 h to remove the organic phase.
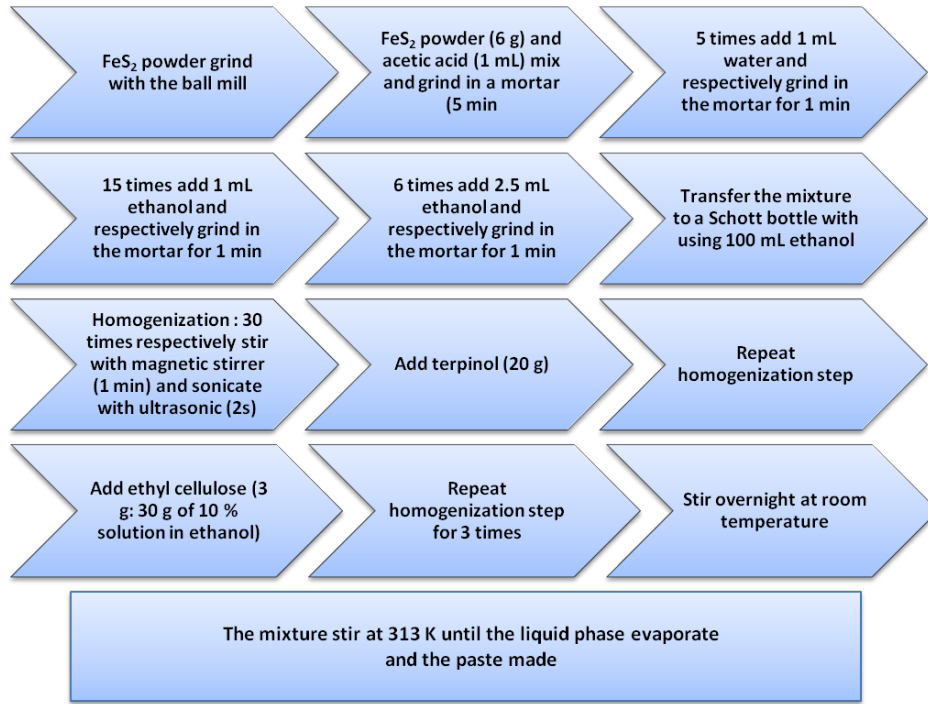
Figure 3.2: The procedure steps used for the preparation of FeS_2 paste.

3.2 Analytical Methods

3.2.1 X-Ray Diffraction (XRD)

X-ray diffraction (XRD) patterns were acquired at room temperature with Cu Kα radiation on a Bruker D8 Advance instrument in the 2θ range of $10°$ - $80°$ in Bragg-Brentano geometry (θ-θ scan). In addition, all of the diffractograms were analyzed with DIFFRAC Plus Eva software and compared with the ICDD database (The International Centre for Diffraction Data). Average particle sizes were calculated from the peak broadening of the XRD patterns using the Scherrer equation (eq. (3.2)).

$$\tau = \frac{K\lambda}{\beta cos\theta} \tag{3.2}$$

In this equation τ is average of the grain size of the crystals, K is a dimensionless shape factor, λ is the X-ray wavelength, β is half width (FWHM) and θ is the diffraction angle or Bragg angle.

3.2.2 UV-Vis Spectroscopy

The UV-Vis or UV-Vis-NIR (in case of pyrite) absorption spectra of the samples were recorded using a Varian Cary 100 Scan UV-Vis or an Agilent Cary 5000 spectrophotometer.

The diffuse reflectance measurement was performed by using an Ulbricht sphere. In this case, barium sulfate was used as a reflectance standard. The reflectance (R) was converted by the instrument software to F(R) values according to the Kubelka-Munk function:

$$F(R_\infty) = \frac{(1 - R_\infty)^2}{2R_\infty} = \frac{K}{S} \tag{3.3}$$

R_∞: diffuse reflection of the sample, $K = 2\beta$: absorption coefficient, $S = 2s$: scattering coefficient

The band gaps were determined by the respective Tauc plots of the modified Kubelka-Munk function $(F(R).h.\nu)^n$ versus the energy of the exciting light $(h.\nu)$ based on the following equation [22, 119]:

$$(F(R_\infty) \cdot h\nu)^n \propto h\nu - E_g \tag{3.4}$$

$h\nu$: photon energy, E_g: band gap energy, n: is 1/2 for direct transitions and is 2 for indirect transitions.

3.2.3 Scanning Electron Microscopy (SEM)

Field-emission scanning electron microscopy (FE-SEM) measurements were carried out on a JEOL JSM-6700F field-emission microscope equipped with a cold field emission gun electron source. The sample surface was scanned with an electron beam and the emitted electrons from the sample were collected by a secondary electron detector (SE). A tungsten single crystal filament with an accelerating voltage of 2.0 kV was used as an electron source.

The scanning electron microscope has been used to examine the particle morphologies and shape. Besides this function, SEM was also applied as an analytical tool for the characterization of samples. Here, especially the energy-dispersive X-ray spectroscopy (EDXS) is important. By means of the EDXS, the chemical compositions of some samples were analyzed.

3.2.4 Transmission Electron Microscopy (TEM)

Transmission electron microscopy (TEM) was performed by a FEI Tecnai G2 F20 TMP instrument (C_s = 2 mm, C_C = 2mm), equipped with a 200 kV field emission gun. Micrographs were taken in bright field (BF) and selected area electron diffraction (SAED) mode.

3.2.5 Raman Microscopy

For Raman measurements, a confocal Raman microscope (Senterra Bruker Optik GmbH) has been employed. All spectra were obtained in backscattering geometry using a microscope device that allows the incident light (633 nm He-Ne laser with a power of 2 mV) to be focused on the sample as a spot of about 2 μm in diameter.

3.2.6 High Performance Ion Chromatography (HPIC)

High performance ion chromatography (HPIC) was performed with a high performance DIONEX ICS-1000 ion chromatography system equipped with a 2 × 250 mm IonPac AS9-HC column, a conductivity detector and an electro regenerator suppressor. As eluent an alkaline solution was applied (0.008 mol L^{-1} Na$_2$CO$_3$ and 0.0015 mol L^{-1} NaHCO$_3$) with its flow rate being 0.3 mL min^{-1}.

3.2.7 Photometric Cuvette Test

The photometric studies were performed on a Dr Lange ISiS 6000 MDA Photometer. All of the cuvette tests were purchased from Hach Lange GmbH (Düsseldorf Germany). The measurements were carried out on diluted samples and have been calculated to the real concentrations.

The details of the cuvette tests were as follow; (these details were all adapted from the product information sheets from Hach Lange GmbH, for more information see [120])

LCK 320 Iron (II/III) Test:

Iron (II) ions form an orange-red complex with 1.10-phenanthroline. The iron (III) ions are reduced to iron (II) ions. The pH of the sample should be 3 − 9. The color reaction of the Fe$^{2+/3+}$ analyses is strongly temperature dependent. Therefore the working temperature of the samples and cuvettes should be around 20 °C. The concentration limit of this test is 0.2 − 6.0 mg Fe$^{2+/3+}$/L.

LCK 653 Sulfide Test:

In this test, dimethyl-p-phenylenediamine reacts with hydrogen sulfide to form an intermediate compound which turns into leucomethylene blue. The leucomethylene blue is oxidized to methylene blue by iron(III) ions. The pH of the sample should be 3 – 10 and the temperature of both samples and reagents should be 15 – 25 °C. The concentration limit of this test is $0.1 - 2.0$ mg S^{2-}/L.

LCK 654 Sulfite Test:

The reagent reacts with sulfites to form a yellow complex. The pH of the sample should be 3 – 10 and the temperature of both samples and reagents should be 15 – 25 °C. The samples must be analyzed immediately after they have been taken. The concentration limit of this test is $0.1 - 5.0$ mg $SO_3{}^{2-}$/L.

LCK 153 Sulfate Test:

Sulfate ions react with barium chloride in an aqueous solution to form barium sulfate, which is only sparingly soluble. The resulting turbidity is measured photometrically. The pH of the samples should be 3 – 10 and the temperature of both samples and reagents should be 15 – 25 °C. The concentration limit of this test is $40 - 150$ mg $SO_4{}^{2-}$/L.

3.2.8 Determination of Iron (II/III) concentration with 1,10-Phenanthroline

UV-visible absorption spectroscopy is a suitable method for determination of the concentration of any compound which forms a complex that absorbs strongly in the UV-Vis region of the electromagnetic spectrum. The intensity of this absorption and its concentration are linearly related according to the Beer's Law:

$$A = \epsilon b c \tag{3.5}$$

A: absorbance, ϵ: molar absorptivity, b: the path length, c: concentration of the absorbing species

The concentration of Fe (II) ions and the total concentration of iron present in the solution were determined spectrophotometrically by using 1, 10- phenanthroline. The total iron concentration in the solution was determined by reducing Fe (III) ions to Fe (II) ions with hydroxylamine. The absorbance of the samples and the

calibration standards were recorded employing the Varian Cary 100 Scan UV-Vis system over a range of 200-800 nm using a 1 cm cell. The absorption at 508 nm is referred to the ferrous complex. This method has a concentration limit of 0.2-0.4 mg Fe/L, therefore, the samples were diluted before the measurements. The detail of this determination and the calibration curve are presented in Appendix (see appendix 1).

3.3 Photoelectrochemical Measurements (PEC)

3.3.1 Photoelectrochemical Reactor

In this thesis, two setups were employed for the photoelectrochemical measurements. However, the photoelectrochemical reactor was the same for all measurements. A ZAHNER PECC-2 reactor (with a dimension of 6×2.5×8 cm) was used for the PEC measurements (Figure 3.3). The optical window was made of quartz glass with 1.8 cm diameter. In this reactor, the electrolyte volume was 7.2 mL and the light path length in the electrolyte was 1.8 cm.

All of the measurements were performed in a three-electrode system with 0.1 M NaOH as the electrolyte. Pt was used as a counter electrode, Ag/AgCl (3 M NaCl) as a reference electrode and a pyrite- or hematite- electrode as the working electrode. The potential measured against the Ag/AgCl electrode can be converted to the RHE (Reversible Hydrogen Electrode) according to eq. (3.6) or to the NHE (Normal Hydrogen Electrode) according to eq. (3.7):

$$E_{RHE} = E_{Ag/AgCl} + E^0_{Ag/AgCl} + 0.059 \times pH \qquad (3.6)$$

$$E_{NHE} = E_{Ag/AgCl} + E^0_{Ag/AgCl} \qquad (3.7)$$

$E^0_{Ag/AgCl}$ is the potential of the Ag/AgCl electrode against the standard hydrogen electrode (SHE) and its value depends on the concentration of the solution used in the electrode itself. To present the results with the reference to NHE, the measured $E_{Ag/AgCl}$ values were added to 0.21 V.
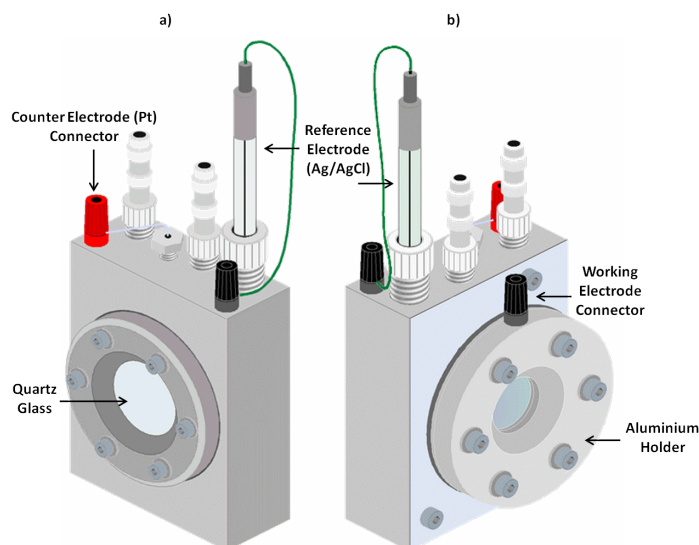
Figure 3.3: Photoelectrochemical reactor a) front-side b) back-side (addapted from[121])

3.3.2 PEC Measurements on Hematite-Electrodes

I-V-Measurements:

The photoelectrochemical properties of the hematite-anodes were determined by current–voltage (I–V) curve measurements. These measurements were carried out with the ZAHNER PECC-2 reactor and the data acquisition was performed with a potentiostat (Iviumstat from IVIUM Technologies) in potential range between -1.0 to +1.0 V. Here Pt was used as a counter electrode, Ag/AgCl (3 M NaCl) as a reference electrode and 0.1 M NaOH as an electrolyte. The I-V curves were measured in the dark and under illumination. Therefore a 450 W Xenon lamp (OSRAM XBO 450) with a cut-off filter for $\lambda > 420\,\text{nm}$ (for visible light source) was applied as a light source. Furthermore, a water filter was used to avoid the infrared rays and the heating of the reactor. The estimated light intensity outside of the reactor was $\sim 30\,\text{mW}\,\text{cm}^{-2}$.

Impedance Measurements:

The flat-band potentials were determined by impedance spectroscopy by means of the Mott-Schottky plots. The measurements were carried out in the dark at room temperature with a Zahner electrochemical workstation (ZAHNER Zenium from ZAHNER Elektrik GmbH, Figure 3.4). The measurement was performed in 0.1

Figure 3.4: The Zahner electrochemical setup [121]

M NaOH in a three electrode system; hematite-electrode as the working electrode, Pt wire as a counter electrode and Ag/AgCl (3 M NaCl) electrode as a reference electrode. The potential was varied between -1.0 to +1.0 V in the frequency range of 10 - 10000 Hz with an amplitude of 0.2 mW.

3.3.3 PEC Measurements on Pyrite-Electrodes

All of the PEC measurements of the pyrite electrodes were performed on Zahner electrochemical setup (ZAHNER Zenium from ZAHNER Elektrik GmbH, Figure 3.4). This setup was equipped with a LED light source for different wavelength. Thus the IPCE measurements (Incident Photon to Current Efficiency) were also possible on pyrite electrodes. Beside the IPCE measurements, the I-V-curves and the flat-band potential of the pyrite electrodes were determined. The details of the PEC cell have been already described in section 3.3.1. The measured $E_{Ag/AgCl}$ values were converted to E vs. NHE (Normal Hydrogen Electrode) by the software according to eq. (3.6) and eq. (3.7).

3.4 Photocatalytic Measurements (PC)

The photocatalytic measurements were performed in two different setups. One of the setups was equipped with a gas chromatograph (GC) and the other one with a mass spectrometer (MS) as the detection unit.

3.4.1 PC Measurements with GC Detector

The photocatalytic reactions were carried out in a double jacket quartz glass reactor (150 mL) with two outlets (Figure 3.5). These outlets have been used for purging the suspension in the reactor with Argon gas. In a typical test, first the suspension in the reactor was purged with Ar for 30 min to remove dissolved O_2. Afterwards, these outlets could be sealed with silicon rubber septa and the headspace above the liquid phase was also purged with Ar until no O_2 and N_2 were detected by the gas chromatograph. The photoreactor was connected to a water cooling system which kept the temperature constant at 20 °C. The photoreactor was irradiated from the outside using an Osram XBO 450 W Xenon lamp in a Müller LAX 1000 lamp housing. The evolved gases were collected with a locking-type syringe (Valco Precision Sampling Syringe, Series A-2, 0.5 mL) through one of the silicone rubber septa. The gas detection was performed with a gas chromatograph (Shimadzu 8A) equipped a molecular sieve 5 Å packed column and a TCD detector. Argon was used as the carrier gas.
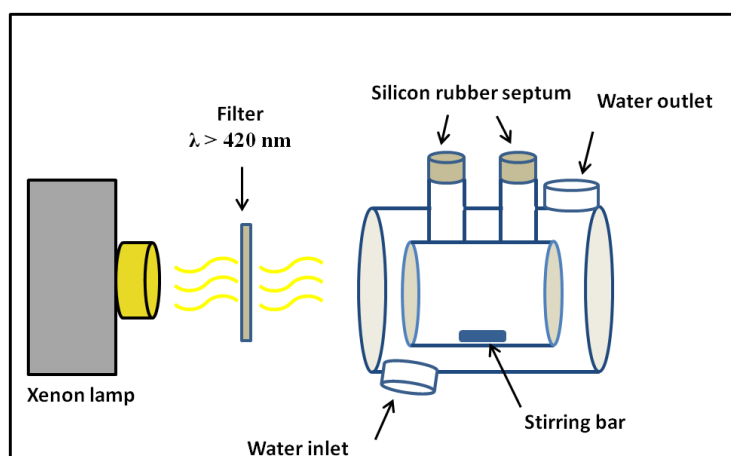
Figure 3.5: Schematic illustration of the reactor used for the photocatalytic reaction, the evolved gases were determined by means of the GC.

3.4.2 PC Measurements with MS Detector

The photocatalytic reactions were carried out in a double jacket quartz glass reactor (100 mL) with in- and outlets for the cooling water system which kept the temperature during the measurements at 20 °C. The photoreactor was continuously purged with argon gas and the flow rate of Ar was controlled with a mass
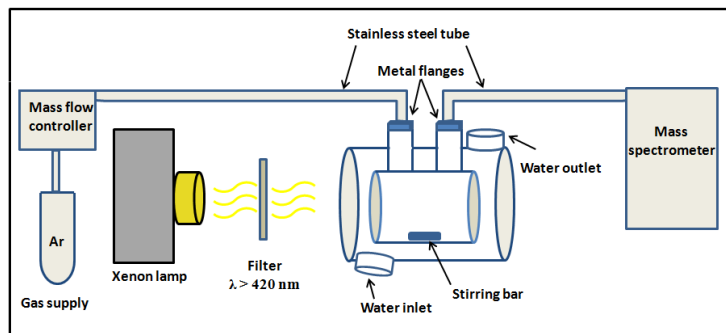
Figure 3.6: Schematic illustration of the continuous experimental setup of the photocatalytic reaction, the evolved gases were determined by means of a mass spectromete (MS), the Ar flow rate during the reaction was $10\,\mathrm{cm^3\,min^{-1}}$.

flow controller. At the same time, the photoreactor was connected to a quadrupole mass spectrometer (QMS) for gas analysis (Hiden HPR-20) as schematically shown in Figure 3.6. In a typical test, first the suspension in the reactor was purged with Ar for 30 min to remove dissolved O_2. Thereafter, the reactor was connected to the Ar mass flow controller and to the QMS. To remove the air in the headspace of the reactor, an Ar gas stream with a flow rate of $50\,\mathrm{cm^3\,min^{-1}}$ has been continuously flown through the reactor before the irradiation, until no traces of molecular O_2 or N_2 could be detected by the QMS. Before the irradiation, the Ar flow rate was switched to $10\,\mathrm{cm^3\,min^{-1}}$ and this remained constant during the whole reaction. The measurements were started with the data acquisition in the dark until the background was stable. Subsequently, the photoreactor was irradiated from the outside using an Osram XBO 1000 W Xenon lamp in a Müller LAX 1000 lamp housing with a cut-off filter for $\lambda > 420\,\mathrm{nm}$. The photocatalytic gas production was monitored continuously in time intervals of about 30 s. After the irradiation time, the lamp was turned off and the data acquisition continued until the system reached a stable baseline. For quantitative analysis of H_2 and O_2, the QMS was calibrated employing standard diluted H_2 (2% in Ar) and O_2 (1% in Ar) both purchased from Linde Gas in Germany.

3.4.3 Photocatalytic O_2 Production with Hematite

The O_2 was photocatalytically produced employing hematite (Fe_2O_3) as the photocatalyst. In a typical test, $1\,\mathrm{g\,L^{-1}}$ of Fe_2O_3 or Co-Cat/Fe_2O_3 was suspended in 50 mL of an aqueous solution containing 0.1 M $Fe(NO_3)_3$ (or $Fe(NO_3)_3 \cdot 9\,H_2O$) as

oxidizing reagents. All of the PC O_2 evolution tests were carried on the MS-setup (section 3.4.2).

3.4.4 Photocatalytic H$_2$ Production with Pyrite

Hydrogen was photocatalytically produced employing pyrite (FeS_2) as the photocatalyst. In a typical test, $1\,g\,L^{-1}$ of FeS_2 or Co-Cat/FeS_2 was suspended in an aqueous solution containing 0.1 M $Na_2S \cdot 9\,H_2O$ and 0.02 M Na_2SO_3 as reducing reagents. The volume of the aqueous solution depended on the used photocatalytic setup.

3.4.5 Photocatalytic Water Splitting

The overall water splitting was carried out employing the so-called Z-Scheme system. In a typical test, $1\,g\,L^{-1}$ of the most active Co-Cat/FeS_2 as H_2 evolution photocatalyst and $1\,g\,L^{-1}$ of the Co-Cat/ Fe_2O_3 as O_2 evolution photocatalyst were suspended in $50\,mL$ of an aqueous solution containing a certain amount of I^-/IO_3^- (from NaI and $NaIO_3$) as the redox couple. All of the overall water splitting tests were carried on the MS-setup (section 3.4.2).

4 Results

4.1 Characterization of Hematite (α-Fe$_2$O$_3$)

4.1.1 Synthesized Hematite Nanoparticles

Structure and Morphology:

α-Fe$_2$O$_3$ nanoparticles have been synthesized by a solvothermal method as described in the experimental section (section 3.1.1). The as-synthesized powder was freeze-dried and calcined at 673 K for the XRD characterization. The XRD diffraction pattern of this powder is shown in Figure 4.1. The analyses of the XRD diffraction and its comparison with the ICDD database clearly indicated the entire characteristic peaks of the hematite crystal structure.
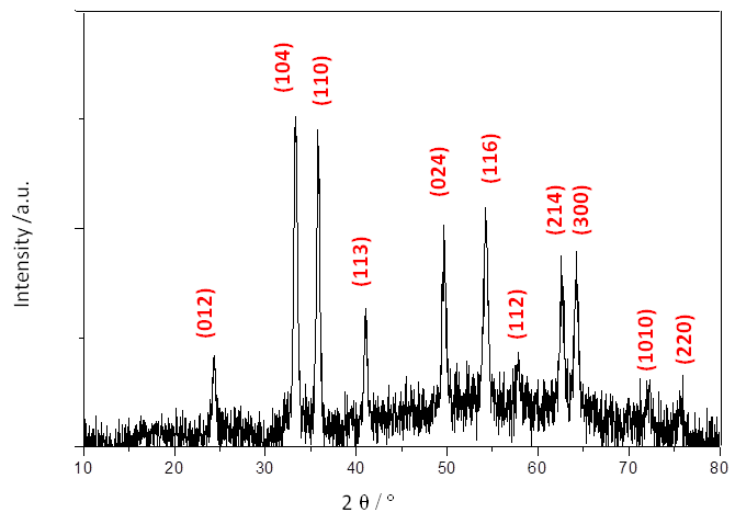
Figure 4.1: XRD pattern of colloidal hematite after freeze-drying and calcination (at 673 K), the reflection peaks are labeled with their Miller indices (hkl) and could all be indexed to the hematite phase of Fe$_2$O$_3$.

It is interesting to note that the XRD diffraction patterns of the hematite powder without calcination shows an amorphous structure (the respective diffraction

46

pattern (Figure 2) is shown in appendix 2).

The particle size and the structural morphology of the synthesized α-Fe$_2$O$_3$ nanoparticles were further characterized by TEM as shown in Figure 4.2. For these measurements, a small drop of the the colloidal aqueous α-Fe$_2$O$_3$ suspension was placed on the TEM grid and dried in air before the measurement. The TEM micrograph of the α-Fe$_2$O$_3$ colloids shows that the particles exhibit nanocuboid shapes. In the images shown in Figure 4.2 , the particles are agglomerated presumably due to the drying procedure. The particle size distribution of α-Fe$_2$O$_3$ was determined to be 20-30 nm.
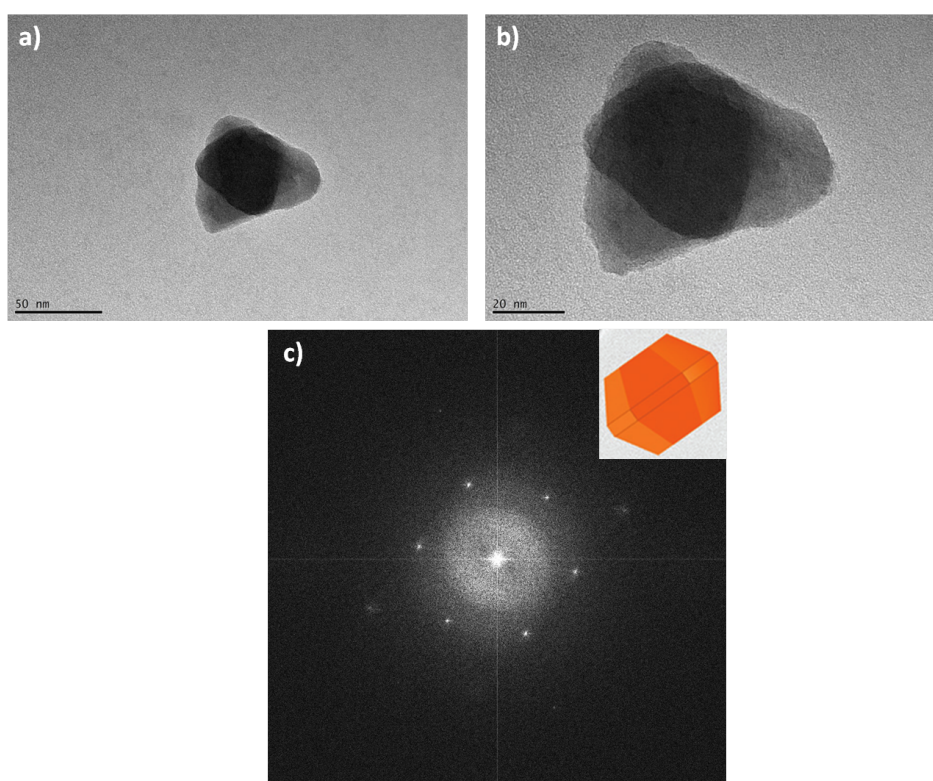
Figure 4.2: a & b)TEM images of colloidal hematite, c) HRTEM image and the corresponding FFT pattern with the geometrical model of a hematite nanocrystal.

Optical Characterization:

The optical properties of the freshly prepared colloidal α-Fe$_2$O$_3$ nanoparticles (diluted to the appropriated concentration) were determined using UV-Vis absorption spectroscopy (Figure 4.3a). Furthermore, the α-Fe$_2$O$_3$ colloids were freeze-dried

and investigated by the UV-Vis diffuse reflectance spectroscopy (Figure 4.3b).

The onset of absorption of the colloidal α-Fe_2O_3 starts below 560 nm; this indicates that hematite is a visible light active photocatalyst. The band gap energy of the α-Fe_2O_3 powders was determined by means of the Tauc plot of the modified Kubelka-Munk function versus the energy of the exciting light as already described in section 3.2.2. For this purpose first, the α-Fe_2O_3 colloids were freeze-dried and afterwards calcined at different temperatures. The thus calculated band gap energies are tabulated below (Table 4.1).The obtained values for the bandgap energy are in excellent agreement with the reported [4, 23] values for hematite, that is 2-2.2 eV.
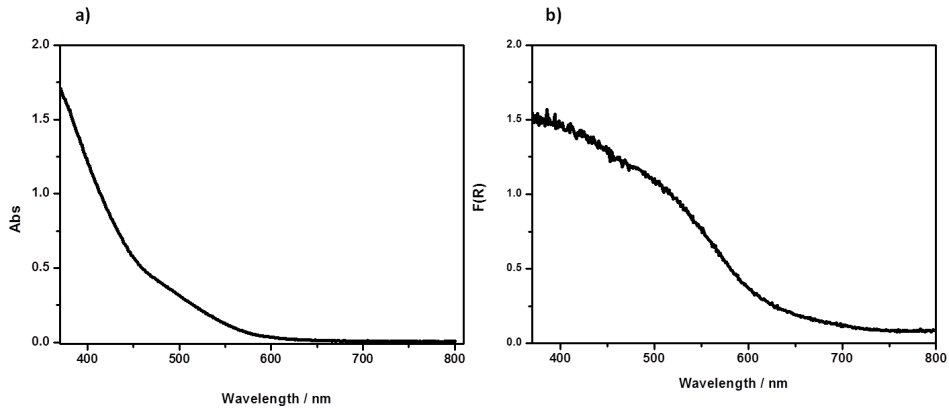
Figure 4.3: a) UV-Vis spectra of transparent colloidal α-Fe_2O_3 nanoparticles, b) Diffuse reflectance spectra of α-Fe_2O_3 powders.

Table 4.1: Band gap energies of α-Fe_2O_3 powder calcined at different temperatures.

Calcination Temperature [°C]	E_g [eV]
400	1.98
500	2.01
600	2.01
700	2.10

4.1.2 Commercial α-Iron (III) Oxide Powder (Fe_2O_3)

The X-ray diffraction (XRD) of the Fe_2O_3 obtained from io-Li-tec Germany (Figure 4.4) indicated that all of the reflection peaks could be indexed to the hematite

structure (PDF ICDD 01-071-5088). No other peaks from impurities such as maghemite have been detected.
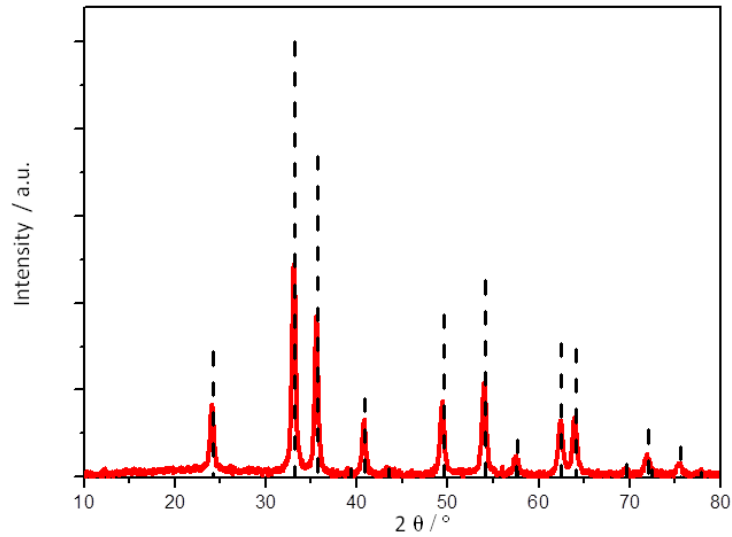
Figure 4.4: XRD pattern of the commercially used α-Iron (III) oxide (Fe$_2$O$_3$) purchased from io-Li-tec Germany. The standard powder pattern of hematite is shown by dashed lines (PDF ICDD 01-071-5088).
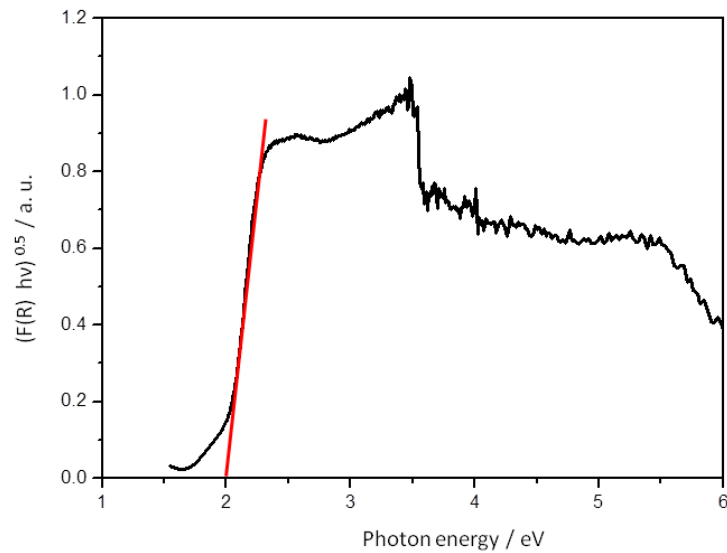
Figure 4.5: Tauc-plot (for indirect bad gap transition) calculated from the UV–vis diffuse reflectance spectrum of commercial Fe$_2$O$_3$.

The UV-vis diffuse reflectance spectrum of the commercial Fe_2O_3 has been measured and the band gap energy of the material has been determined using the Tauc plot of the modified Kubelka-Munk function (Figure 4.5). The band gap energy of the material is $E_g \sim 2.1 \pm 0.1$ eV.

4.2 Characterization of Pyrite (FeS$_2$)

4.2.1 Synthesized Pyrite Nanoparticles

Structure and Morphology:

FeS_2 nanoparticles have been synthesized as described in the experimental section (section 3.1.2). The reaction time could control the nanoparticle size. The reaction times have been varied between 2 h, 4 h, and 8 h. The nanoparticles prepared with a reaction time of 2 h had the smallest particle size and the ones prepared with 8 h reaction time exhibited the biggest size. The FeS_2 nanoparticles obtained after a reaction time of 4 h have been chosen for further characterization.
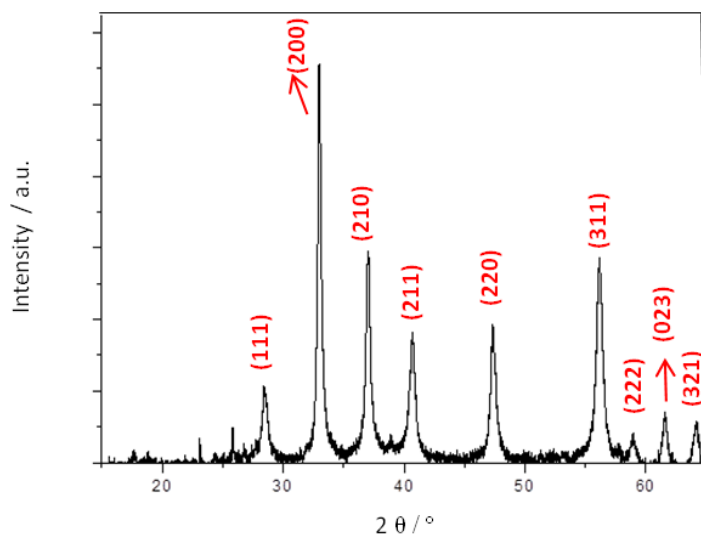
Figure 4.6: XRD pattern of FeS_2 nanoparticles after 4 h reaction time, the reflection peaks are labeled with their Miller indices (hkl) and all could be indexed to the cubic phase of FeS_2.

Figure 4.6 presents the XRD diffraction pattern of so prepared FeS_2 nanoparticles. The analyses of the XRD diffraction and its comparison with the ICDD database indicated that all reflection peaks could be indexed to the cubic phase

of FeS$_2$. No other peaks from impurities such as marcasite, pyrrhotite, or troilite could be detected.

In addition, the particles size of the FeS$_2$ nanoparticles have been calculated using the Scherrer equation (eq. (3.2)) and are presented in Table 4.2. The particle size distribution of the FeS$_2$ nanoparticles is in the range between 20-35 nm.

The particle shape and form have been investigated by means of the SEM. The SEM images show spherical shaped nanoparticles which are agglomerated (Figure 4.7).

Table 4.2: The particle size distribution of FeS$_2$ (pyrite) nanoparticles

2 theta [°]	h k l	Particle Sizes [nm]
28.4	1 1 1	18
33.0	2 0 0	32
37.0	2 1 0	25
40.7	2 1 1	18
47.3	2 2 0	24
56.2	3 1 1	25
58.9	2 2 2	31
61.6	0 2 3	36
64.1	3 2 1	35
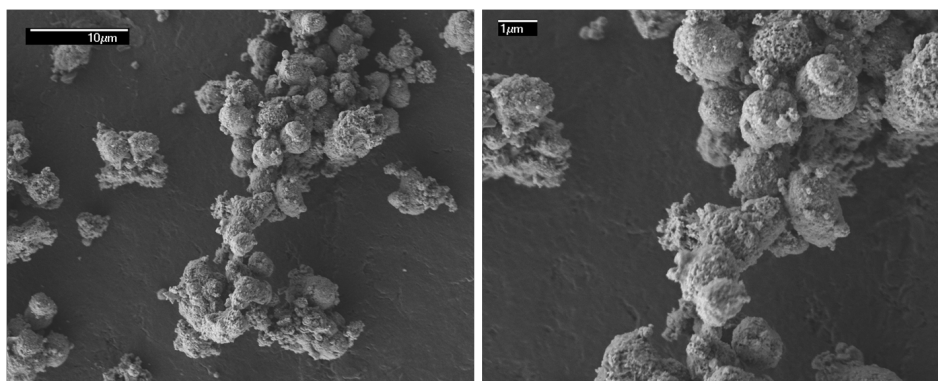
Figure 4.7: SEM images of FeS$_2$ nanoparticles prepared with a reaction time of 4 h.

Optical Characterization:

Figure 4.8 shows the optical absorption spectrum of the thus prepared colloidal FeS$_2$ nanoparticles at different dilutions. First the absorption has been determined

by using the UV-Vis spectroscopy. However, the absorption spectra indicate that the FeS$_2$ nanoparticles absorbed the entire ultra-violet and visible region of the light spectrum. Precisely investigations have been performed by means of a UV-Vis-NIR spectroscopy (the inset in Figure 4.8). The UV-Vis-NIR spectrum proves that the absorption starts below 1370 nm; this is in excellent agreement with the reported band-gap energy [30] for pyrite of 0.9 eV - 1.1 eV.
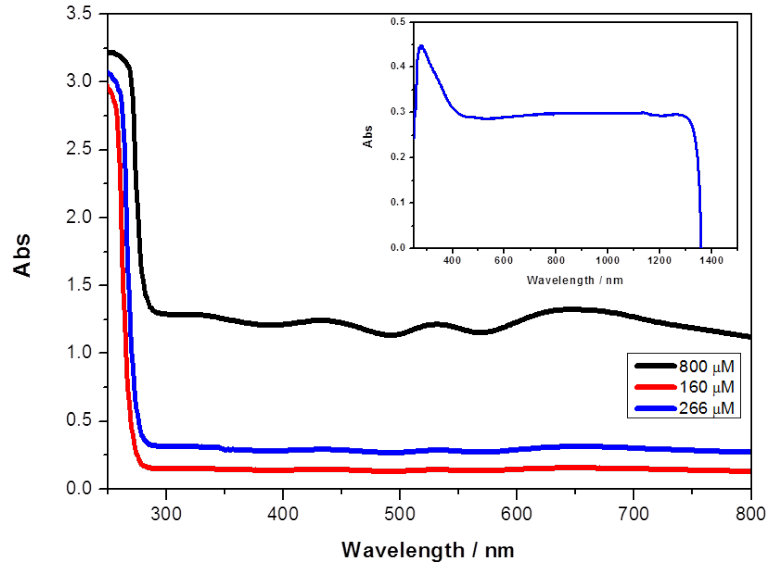
Figure 4.8: UV-Vis spectra of transparent colloidal FeS$_2$ nanoparticles with different concentration, Inset shows the UV-Vis-NIR spectrum of the colloidal FeS$_2$ nanoparticles at a concentration of 266 µM.

4.2.2 Commercial Iron (II) Disulfide Powder (FeS$_2$)

The X-ray diffraction (XRD) of the FeS$_2$ obtained from Sigma-Aldrich (Figure 4.9) indicated that all of the reflection peaks could be indexed to the cubic phase of FeS$_2$ (Also called Pyrite) (PDF ICDD 01-071-0053). No other peaks from impurities such as marcasite, pyrhotite, or troilite have been detected.

The UV-vis diffuse reflectance spectrum of FeS$_2$ has been measured and the band gap energy of the material has been determined using the Tauc plot of the modified Kubelka-Munk function (Figure 4.10). The band gap energy of the material is $E_g \sim 1.1 \pm 0.1$ eV.
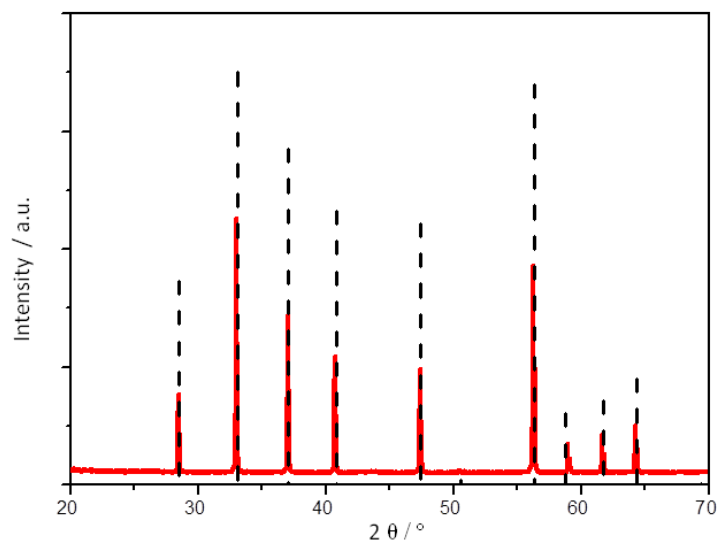
Figure 4.9: XRD pattern of the commercial Iron (II) disulfide (FeS$_2$) purchased from Sigma-Aldrich; The standard powder pattern of pyrite is shown by dashed lines (PDF ICDD 01-071-0053).
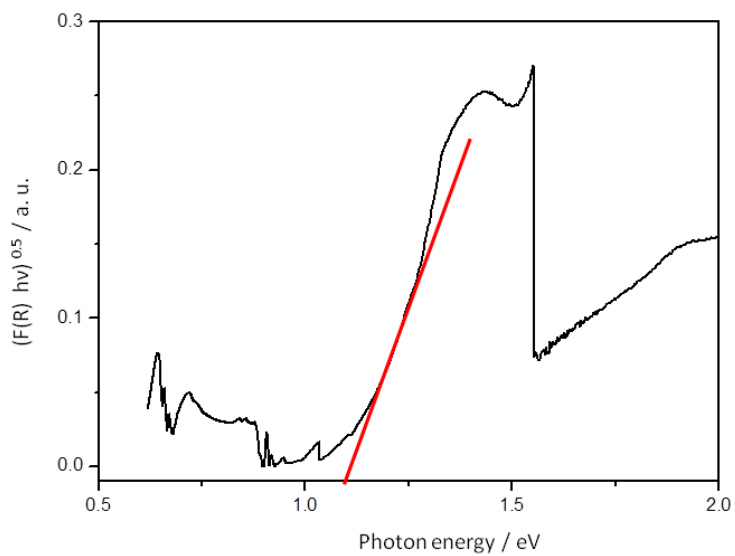
Figure 4.10: Tauc-plot (for indirect bad gap transition) calculated from the UV–vis diffuse reflectance spectrum of the commercial Iron (II) disulfide (FeS$_2$) purchased from Sigma-Aldrich

4.3 PEC Characterization of Hematite-Electrodes

4.3.1 I-V-Characteristics

α-Fe_2O_3 electrodes have been prepared from the colloidal suspension (15 mM) of α-Fe_2O_3 as described in section 3.1.6. The electrodes were un-doped and just calcined at different temperatures. Figure 4.11 shows the I-V curves for so prepared α-Fe_2O_3 electrodes in the dark and under illumination (450 W Xenon lamp with a cut-off filter $\lambda > 420$ nm). In the figure the current densities in the dark and under the illumination are shown as a function of the applied potential V vs. NHE (Normal Hydrogen Electrode).
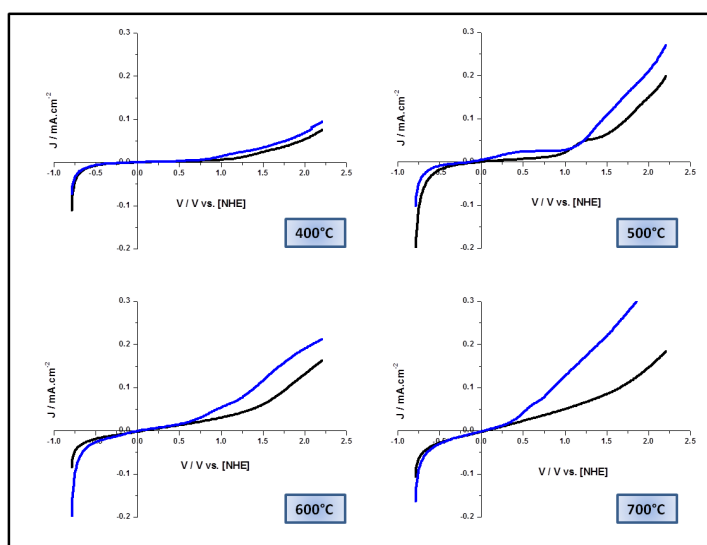
Figure 4.11: I-V curves of the α-Fe_2O_3 electrodes obtained at different calcination temperature (400 °C, 500 °C, 600 °C and 700 °C) in 0.1 M NaOH (pH 13). Current densities (mA cm^{-2}) in the dark (black lines) and under illumination (cut-off filter $\lambda > 420$ nm, light intensity ~ 30 mW cm^{-2}, blue lines) are shown as a function of the applied potential, V vs. NHE.

The two most important parameters that can be determined from a current-voltage curve are the plateau current and the onset potential. The analyses of the I-V curves under the dark conditions revealed that the electrocatalytic oxygen evolution started at the lower potentials for the electrodes obtained at higher calcination temperatures (600 °C and 700 °C). Moreover, these electrodes exhibit higher current density. In addition, the photocurrent curves show a better separation from the dark current for these electrodes.

The electrode prepared at a calcination temperature of 700 °C exhibits the highest value of the plateau current. The value of the plateau current indicates the amount of photogenerated holes reaching the semiconductor/liquid junction (SCLJ). Further investigations have been performed on the α-Fe$_2$O$_3$ electrodes prepared from the colloidal suspension with different concentrations (1.5 mM, 3 mM, 10 mM, and 15 mM). Figure 4.12 shows the current-voltage curves of the electrodes prepared from colloidal α-Fe$_2$O$_3$ suspensions with different concentrations and subsequently calcined at 700 °C.
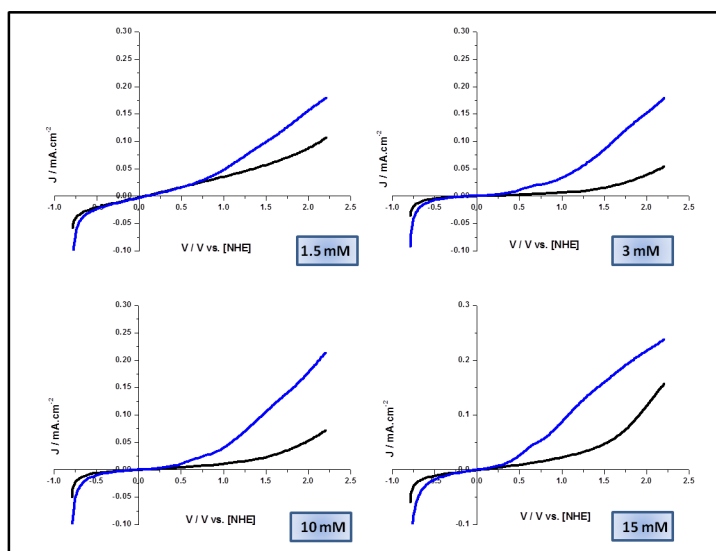
Figure 4.12: I-V curves of the α-Fe$_2$O$_3$ electrodes prepared from colloidal α-Fe$_2$O$_3$ with different concentration (1.5 mM, 3 mM, 10 mM, and 15 mM), measured in 0.1 M NaOH (pH 13). Current densities (mA cm^{-2}) in the dark (black lines) and under illumination (cut-off filter $\lambda > 420$ nm, light intensity ~ 30 mW cm^{-2}, blue lines) are shown as a function of the applied potential, V vs. NHE.

4.3.2 Impedance Measurements

Impedance measurements were performed on the hematite electrodes as described in section 3.3.2. These measurements have been executed at a frequency of 1 kHz. The flat-band potential can be experimentally determined by impedance spectroscopy using the Mott-Schottky equation. The flat-band potentials of α-Fe$_2$O$_3$ electrodes at the semiconductor/electrolyte junction have been measured from Mott-Schottky

plots using the following equation:

$$\frac{1}{C^2} = \frac{2}{\varepsilon_{SC} \cdot \varepsilon_0 \cdot e_0 \cdot N_D}(E - E_{FB} - \frac{kT}{e_0}) \tag{4.1}$$

C: capacitance of the space charge layer (F), ε_{SC}: permittivity of the semiconductor electrode, ε_0: permittivity of free space $(8.85 \times 10^{-12}\,\mathrm{F\,m^{-1}})$, e_0: elementary charge (C), N_D: donor density ($\mathrm{m^3}$), E: applied potential (V vs. RHE), E_{FB}: flat-band potential (V vs. RHE), k: Boltzmann constant $(1.381 \times 10^{-23}\,\mathrm{J\,K^{-1}})$, T: temperature (K).
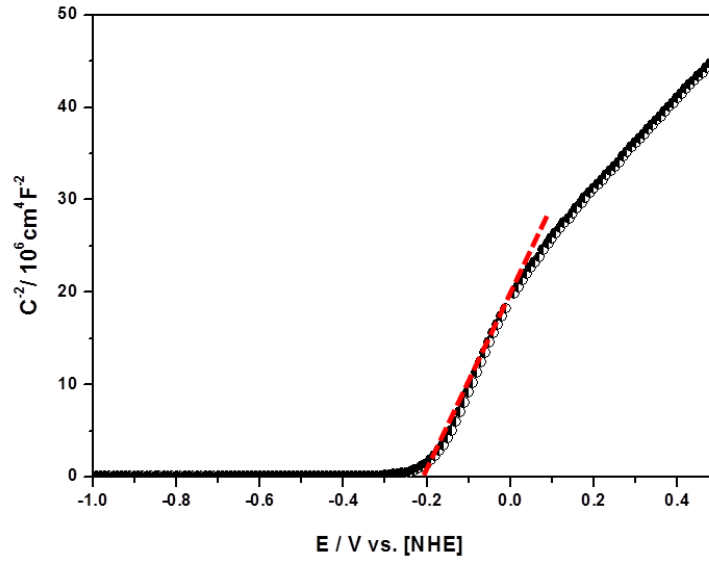
Figure 4.13: Mott-Schottky plot of an α-Fe$_2$O$_3$-electrode calcined at $400\,°\mathrm{C}$, measured in the dark, in 0.1 M NaOH (pH 13), with a frequency of $1\,\mathrm{kHz}$.

Figure 4.13 shows the plot of the $1/\mathrm{C}^2$ vs. E based on the Mott-Schottky equation (eq. (4.1)) for a hematite electrode prepared from colloidal α-Fe$_2$O$_3$ and calcined at $400\,°\mathrm{C}$. The $1/\mathrm{C}^2$ values have been normalized by the active area of the electrode. The intersecting point of the red line and the potential axis show the E_{FB} of the hematite. This point should be considered with accuracy around $\pm\,0.02$.

Table 4.3 summarizes the values determined for the flat-band potential of the hematite electrodes and the tempered FTO glasses. These results have been presented in E vs. NHE at the measured pH value and converted to RHE using eq. (3.6). Furthermore, the donor density values of the hematite electrodes were

determined using the following equation:

$$N_D = \frac{2}{\varepsilon_{SC} \cdot \varepsilon_0 \cdot e_0 \cdot m} \tag{4.2}$$

Where m is the slope of the regression line from the eq. (4.1) and ε_{SC} of the hematite was taken 24.1 according to the [122, 123].

The flat-band potential of Fe_2O_3 is usually found to be around 0.5 V versus the reversible hydrogen electrode (RHE) [3, 42, 124]. The results in the table are in good agreement with the reported values in the literature. In addition, the hematite electrodes showed a positive slope in the dark. This fact indicates that hematite is a n-type semiconductor with electrons as the majority carriers.

Table 4.3: E_{FB} of α-Fe_2O_3-electrode and FTO glass, N_D of α-Fe_2O_3-electrode, calcined at 400 °C and 600 °C, calculated from the respective Mott-Schottky plots, measured with a frequency of 1 kHz.

Electrodes	E_{FB} [V] vs. NHE pH 13	E_{FB} [V] vs. RHE	N_D [cm^{-3}]
α-Fe_2O_3-400 °C	-0.2	0.51	1.0×10^{19}
α-Fe_2O_3-600 °C	-0.3	0.41	3.23×10^{18}
FTO-400 °C	-0.58	0.13	-
FTO-600 °C	-0.61	0.10	-

4.4 PEC Characterization of Pyrite-Electrodes

4.4.1 Cyclic Voltammetry (CV)

The electrochemical measurements were performed on FeS_2-electrodes prepared from natural pyrite and FeS_2-powder as described in section 3.1.7.

The current-potential behavior of pyrite was investigated in the cyclic voltammetry (CV) mode. Figure 4.14 shows the CV of the natural pyrite in the dark and under the illumination in 0.1 M NaOH. In this figure the current densities in the dark and under the illumination are shown as a function of the applied potential V vs. NHE.

The Zahner electrochemical setup is equipped with a LED light source for the different wavelengths. IPCE (Incident photon to current efficiency) of the pyrite
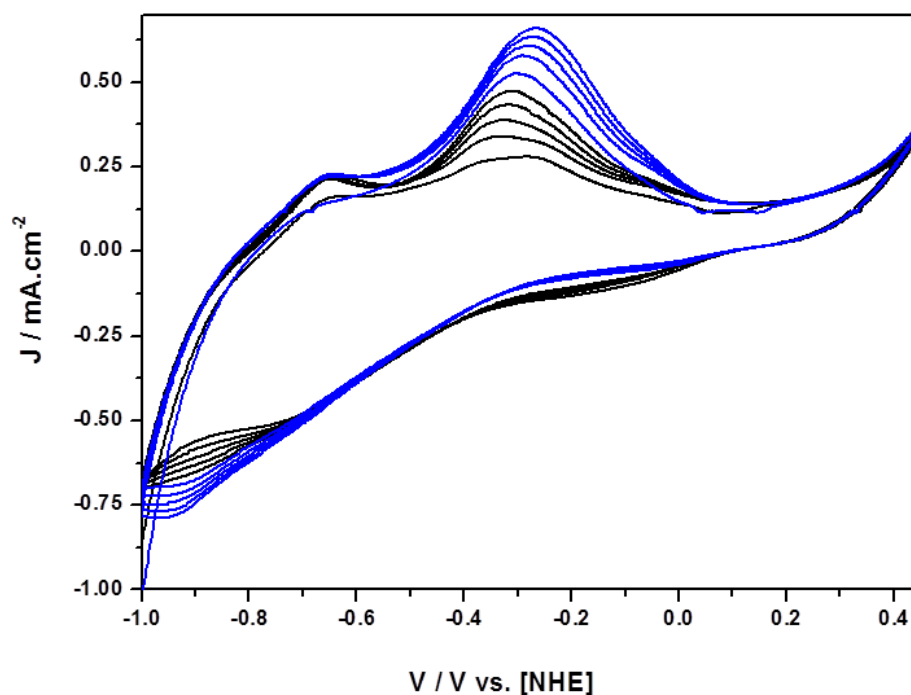
Figure 4.14: CV curves of the natural pyrite electrode measured in 0.1 M NaOH
(pH 13). Current densities ($mA\,cm^{-2}$) in the dark (black lines) and
under illumination ($\lambda = 455$ nm, $18.7\,mW\,cm^{-2}$, blue lines) are shown
as a function of the applied potential, V vs. NHE.

electrode has been measured to chose the best wavelength for the photocurrent
measurements (See Figure 3 in appendix 3). Based on the IPCE data, a light
source with the wavelength of 455 nm (light intensity $\sim 18.7\,mW\,cm^{-2}$) has been
chosen for the photocurrent measurements. In this figure, the current densities in
the dark and under the illumination are shown as a function of the applied potential
V vs. NHE.

Figure 4.15 presents the CV measurements of the pyrite electrode (prepared from
the FeS_2-powder and calcined at $400\,°C$). The measurement was carried out under
the same conditions.
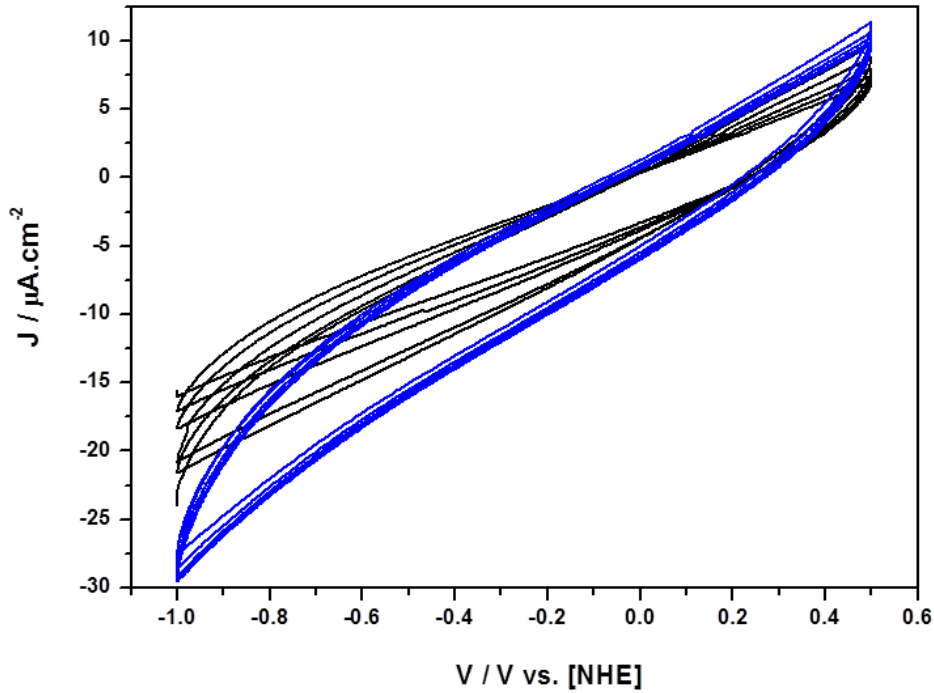
Figure 4.15: CV curves of the pyrite electrode (prepared from the FeS$_2$-powder, and calcined at 400 °C) measured in 0.1 M NaOH (pH 13). Current densities (mA cm^{-2}) in the dark (black lines) and under illumination ($\lambda = 455$ nm, 18.7 mW cm^{-2}, blue lines) are shown as a function of the applied potential, V vs. NHE.

4.4.2 Impedance Measurements

The flat-band potential of the pyrite electrode (prepared from the FeS$_2$-powder, calcined at 400 °C and 500 °C) has been determined by means of the impedance spectroscopy. Figure 4.16 shows the plot of the $1/C^2$ vs. E based on the Mott-Schottky equation (eq. (4.1)), for a pyrite electrode prepared from FeS$_2$-powder and calcined at 400 °C. The intersecting point of the red line and the potential axis indicates the E$_{FB}$ of the pyrite. This point should be considered with accuracy around $\pm$ 0.02.

Table 4.4 summarized the so calculated flat-band potentials of the pyrite electrodes and the tempered FTO glass. These results have been presented in E vs. NHE at the measured pH value and converted to RHE according to the eq. (3.6). Furthermore, the donor density (N_D) values of the pyrite electrodes were determined using eq. (4.2) (where $\varepsilon_{FeS_2} = 10.9$ [33, 125]).
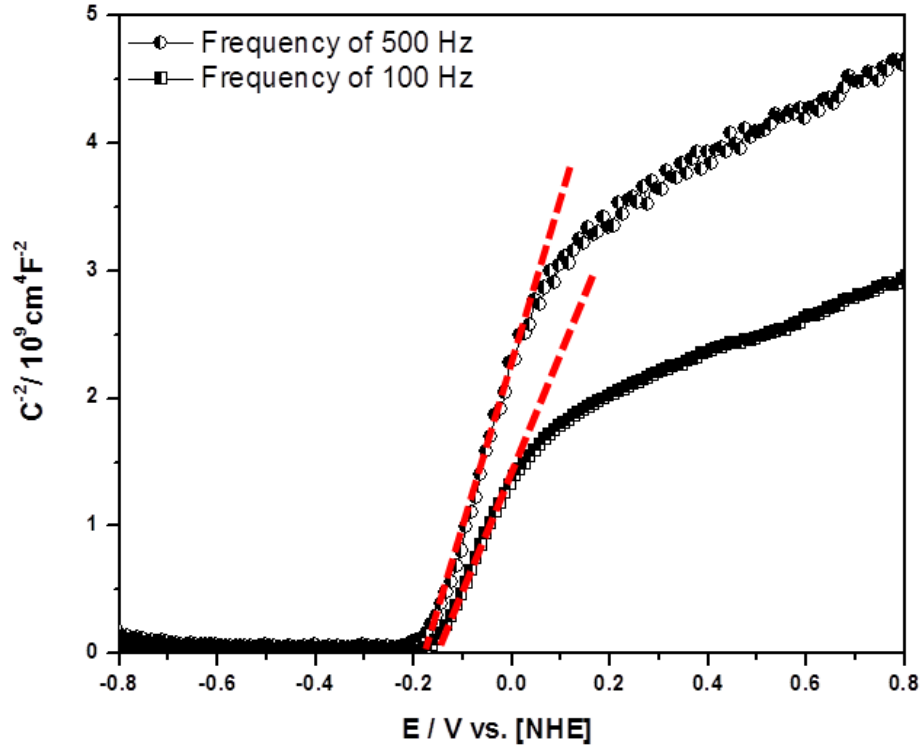
Figure 4.16: Mott-Schottky plot of FeS$_2$-electrode calcined at 400 °C, measured in the dark, in 0.1 M NaOH (pH 13), with frequencies of 500 Hz and 100 Hz.

Table 4.4: E$_{FB}$ of FeS$_2$-electrode and FTO glass, N$_D$ of FeS$_2$-electrode, calcined at 400 °C and 500 °C, calculated from the respective Mott-Schottky plots, measured with frequencies of 500 Hz and 100 Hz.

Electrodes	Frequency [Hz]	E$_{FB}$ [V] vs. NHE pH 13	E$_{FB}$ [V] vs. RHE	N$_D$ [cm^{-3}]
FeS$_2$-400 °C	500	-0.18	0.53	3.10×10^{20}
FeS$_2$-500 °C	500	-0.16	0.55	1.35×10^{19}
FeS$_2$-400 °C	100	-0.17	0.54	5.05×10^{20}
FeS$_2$-500 °C	100	-0.18	0.53	1.05×10^{19}
FTO-400 °C	500	-0.52	0.19	-
FTO-500 °C	500	-0.6	0.11	-
FTO-400 °C	100	-0.52	0.19	-
FTO-500 °C	100	-0.59	0.12	-

4.5 Photocatalytic (PC) Tests

In this work the photocatalytic activity results are presented in the form of the calculated hydrogen or oxygen production rate ($\mu mol\,h^{-1}$) and as photonic efficiency (ζ %).

The photonic efficiency (ζ) has been calculated according to eq. (4.3) [126].

$$\zeta = \frac{\Delta n/\Delta t}{J_0} \tag{4.3}$$

ζ: photonic efficiency, $\Delta n/\Delta t$: evolution rate of H_2 or O_2 in $mol\,s^{-1}$, J_0: incident photon flux ($mol\,s^{-1}$).

The incident photon flux (J_0) is calculated based on the following equation:

$$J_0 = \frac{I_a \cdot \lambda \cdot A}{N_A \cdot h \cdot c} \tag{4.4}$$

Where A is the illuminated surface area (7.065 cm^2), λ is the average illumination wavelength (from the wavelength range where the photocatalyst absorbs the light, for FeS_2 is 942 nm, for Fe_2O_3 is 597 nm), N_A is Avogadro number (mol^{-1}), h is Planck constant ($J\,s$) and c is the light velocity ($m\,s^{-1}$). I_a ($J\,s^{-1}\,cm^{-2}$) is determined from the integration of the irradiance of the lamp in the wavelength area between 420-800 nm (in case of FeS_2) or between 420-660 nm (in case of Fe_2O_3). For this purpose, the irradiance of the Xe arc lamp used for the photocatalytic tests was measured by a radiometer (BW Tek Company).

All of the photonic efficiencies of the photocatalytic reactions carried out with the MS measurement setup (section 3.4.2, which a mass spectrometer employed as the detector) have been calculated in this way.

4.5.1 O_2 Production with Hematite

Photocatalytic oxygen evolution tests have been performed on: synthesized α-Fe_2O_3-nanoparticles (more information in section 3.1.1), commercial α-Fe_2O_3 powder (more information in section 3.1), and on Co-Cat/Fe_2O_3-powders (more information in section 3.1.5). The results obtained employing the last two types of Fe_2O_3 will follow in the next section.

In all of these experiments 0.1 M aq.Fe$(NO_3)_3$ (pH $\sim$ 1.5-2) has been used as oxidizing reagent. There was no O_2 evolution in pure water. All of the photocatalytic O_2 production investigations have been performed by means of the MS measure-

ment set-up (with the mass spectroscopy as the detection unit, more information in section 3.4.2).
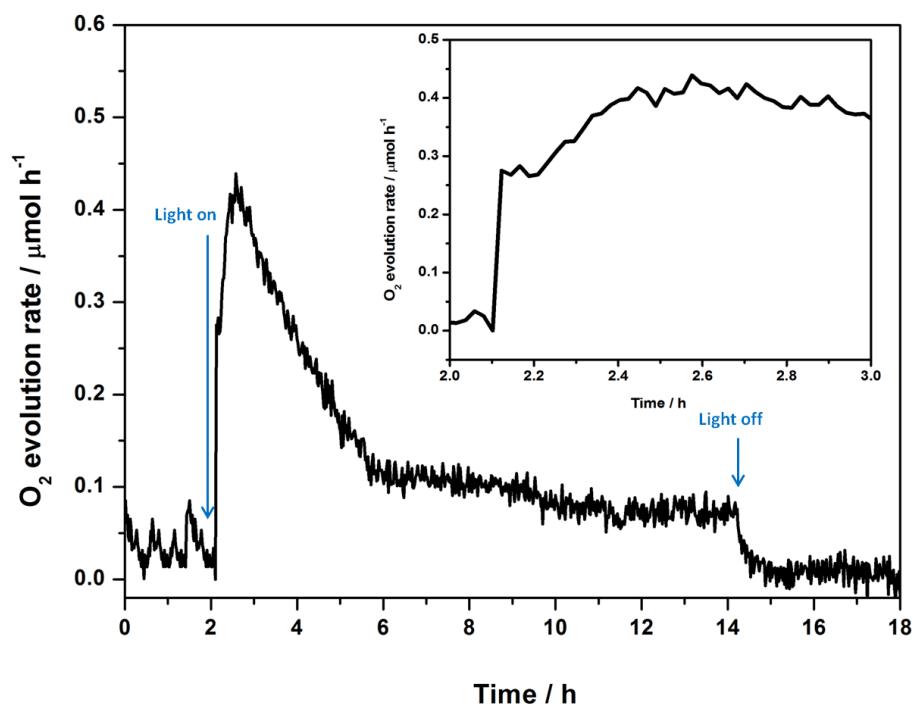
Figure 4.17: Photocatalytic O_2 evolution employing synthesized α-Fe_2O_3 nanoparticles suspended in 0.1 M aq.$Fe(NO_3)_3$ (pH 1.5-2) under visible light irradiation; light source: 1000 W xenon lamp with a cut-off filter $\lambda >$ 420 nm ($I_{420-660} \sim 66\,mW\,cm^{-2}$). Inset shows the O_2 evolution rate during the first hour of the irradiation.

Figure 4.17 illustrates a typical time courses of the photocatalytic O_2 production (the experimental details are described in section 3.4.3). Here $1\,g\,L^{-1}$ of the synthesized α-Fe_2O_3-nanoparticles was suspended in $50\,mL$ of an aqueous solution containing 0.1 M $Fe(NO_3)_3$. In all experiments first, the time course of the O_2 formation (and of that of other possible gaseous compounds) was monitored in the dark until the signals became constant within the limits of the experimental error (that is after 90-120 min). Here (Figure 4.17) the irradiation has been started after approximately 2 h. Subsequently, the O_2 evolution started after 20-30 min irradiation, the value rose fast but after 60 min irradiation the evolution rate decreased and the system reached nearly a constant O_2 evolution rate. When the Light was switched off after 12 h irradiation, a rapid decay of the O_2 evolution rate was observed and the baseline was then reached again.

The O_2 evolution rate has been determined from the difference between the average value of the evolution rate obtained upon the illumination and that observed in the dark (that is the baseline value at the end of the experiment). Usually, the data points measured at the end of each photocatalytic run have been considered as the baseline of the formation of the corresponding gaseous compound. With this calculation, the average value of the O_2 evolution rate obtained was 0.13 µmol h^{-1} ($\zeta = 1.56 \times 10^{-3}$ %) for the synthesized α-Fe$_2$O$_3$-nanoparticles. It should be noted that in this way all of the O_2 evolution rate data have been obtained, thus enabling the quantitative comparsion of all measured O_2 evolution rates in this work.

4.5.2 O_2 Production with RuO$_2$ loaded α-Fe$_2$O$_3$

The α-Fe$_2$O$_3$ powder has been modified with RuO$_2$ to improve its activity as an oxygen evolution photocatalyst. For this purpose, hematite (20-40 nm α-Fe$_2$O$_3$ powder from Ionic Liquid Technologies Germany) has been modified by means of the impregnation method (see section 3.1.5) with a solution of RuCl$_3 \cdot$ xH$_2$O. RuO$_2$ has already been used as oxygen evolution co-catalyst in various photoelectrochemical investigations [127, 128].

A set of experiments has been performed employing ruthenium loaded α-Fe$_2$O$_3$. Figure 4.18 illustrates the O_2 evolution rates (µmol h^{-1}) and the corresponding photonic efficiencies for α-Fe$_2$O$_3$ and its modification, respectively, for 0.1, 0.5, and 1 weight % of RuO$_2$ loaded α-Fe$_2$O$_3$. In all of these experiments 0.1 M aqueous Fe(NO$_3$)$_3$ (pH $\sim$ 1.5-2) has been used as oxidizing reagent.

The results in this section show that the RuO$_2$-loaded α-Fe$_2$O$_3$ is photocatalytically more active than the unmodified one. 0.5 % RuO$_2$ loaded α-Fe$_2$O$_3$ shows the highest activity. This was the reason why 0.5 weight % loading was chosen also for the modifications with the other co-catalysts (see next section).
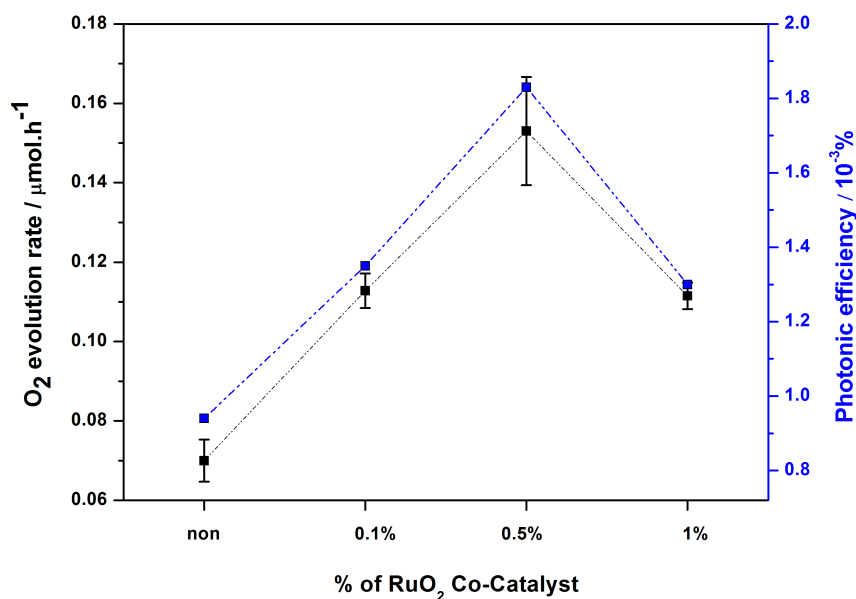
Figure 4.18: Photocatalytic O_2 evolution from 0.1 M aqueous $Fe(NO_3)_3$ solution (pH $\sim$ 1.5-2) employing α-Fe_2O_3 modified with different weight % of RuO_2 as the co-catalysts under visible light irradiation; light source: 1000 W xenon lamp with a cut-off filter $\lambda > 420\,nm$ ($I_{420-660} \sim 66\,mW\,cm^{-2}$).

4.5.3 O_2 Production with Co-catalyst loaded α-Fe_2O_3

The photocatalytic activity of the water splitting reaction can usually be improved by the utilization of different co-catalysts loaded onto the catalyst surface. These co-catalysts provide active sites for the redox reaction (that is for the oxidation or for the reduction reaction, respectively) and /or suppress the reverse reaction of water formation. Both noble metals (e.g., Pt, Au) and transition metal oxides (e.g., NiO, RuO_2) have been widely used as co-catalysts in photocatalytic water splitting systems showing significant enhancement of the photocatalytic activity for H_2 and O_2 evolution [129].

Since in this work it was very important to have an active O_2 evolution catalyst for the oxidation of water, a series of co-catalyst loaded α-Fe_2O_3 have been prepared. For this purpose commercial α-Fe_2O_3 (from Ionic Liquid Technologies Germany) has been used and has been modified with both, noble metal and transition metal oxide catalysts. Platinum (Pt), Gold (Au), Cobalt (Co), Copper (Cu), Iridium (Ir),

Chromium (Cr), Ruthenium (Ru), and Nickel (Ni) were loaded as pure metals or as metal oxides on these commercially available α-Fe_2O_3-powders and were used for the production of oxygen employing Fe^{3+} as electron acceptor (sacrificial agent).

Metal deposition on α-Fe_2O_3 was carried out by photodeposition and metal impregnation methods as described in section 3.1.5. The photocatalytic oxidation of water under visible light should produce O_2 and Fe^{2+} ions. Mass spectroscopy (MS) was used to analyze on-line the production of oxygen gas (see Figure 3.6).

The photocatalytic oxygen production rates and the photonic efficiencies (ζ) for all Co-Cat/Fe_2O_3 systems are given in table 4.5. In this table, the results are presented in the form of the calculated oxygen production rate (μmol h^{-1}) and as photonic efficiency (ζ %). RuO_2/Fe_2O_3 showed the highest photocatalytic activity for O_2 evolution in this studies with an O_2 formation rate of 0.15 μmol h^{-1} ($\zeta = 1.83 \times 10^{-3}$ %) while IrO_2/Fe_2O_3 exhibits a very low rate of 0.01 μmol h^{-1} ($\zeta = 1.31 \times 10^{-4}$ %). In the case of Cr_2O_3/Fe_2O_3, almost no O_2 could be detected.

Table 4.5: Photocatalytic O_2 production rates and photonic efficiencies (ζ) employing α-Fe_2O_3 modified with different co-catalysts (0.5 wt%) under visible light irradiation (light source: 1000 W xenon lamp with a cut-off filter $\lambda > 420$ nm, $I_{420-660} \sim 66$ mW cm^{-2}). 0.1 M aq.Fe(NO$_3$)$_3$ (pH 1.5-2) has been used as oxidizing reagents.

Co-Cat/Fe_2O_3	O_2 Production rate [μmol h^{-1}]	ζ [10^{-3}%]
RuO_2/Fe_2O_3	0.15	1.83
CuO/Fe_2O_3	0.15	1.75
CoO/Fe_2O_3	0.14	1.69
Pt/Fe_2O_3	0.13	1.51
Au/Fe_2O_3	0.09	1.17
Fe_2O_3	0.07	0.94
NiO/Fe_2O_3	0.06	0.68
IrO_2/Fe_2O_3	0.01	0.13
Cr_2O_3/Fe_2O_3	0	0

4.5.4 H$_2$ Production with Pyrite

Photocatalytic hydrogen evolution tests have been performed on: synthesized FeS_2 nanoparticles (discribed in section 3.1.2), commercial FeS_2 powder (more information in section section 3.1), and Co-Cat/FeS_2 powders (more information in section 3.1.5). The results obtained employing the last two types of FeS_2 will follow
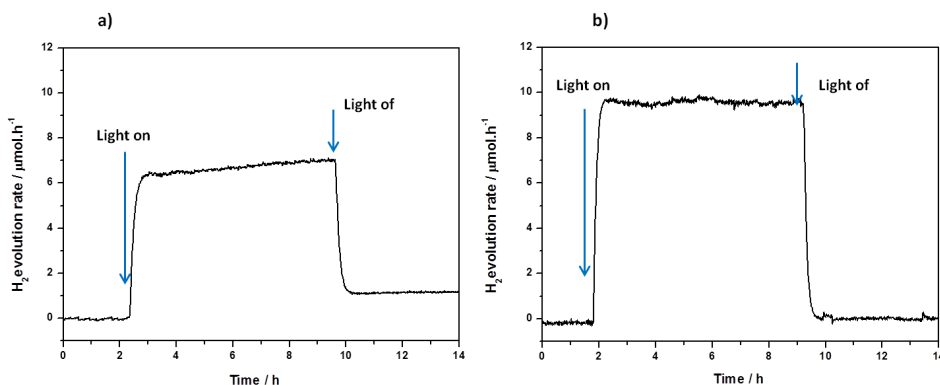
Figure 4.19: Photocatalytic H_2 evolution rate from a) synthesized FeS_2 nanopar-
ticles, b) synthesized FeS_2 nanoparticles modified with 0.2 wt% Pt,
suspended in aq. 0.1 M Na_2S and 0.02 M Na_2SO_3 (pH 13.5-14) un-
der visible light irradiation; light source: 1000 W xenon lamp with a
cut-off filter $\lambda > 420\,nm$ ($I_{420-800} \sim 110\,mW\,cm^{-2}$).

in the next section. In all of the experiments 0.1 M Na_2S and 0.02 M Na_2SO_3 have
been used as reducing reagents. There was no H_2 evolution in pure water, that is
in the absence of any sacrificial reagents.

Figure 4.19 presents typical time courses of the photocatalytic H_2 production
employing a) synthesized FeS_2 nanoparticles and b) FeS_2 nanoparticles modified
with 0.2 wt% Pt. In these experiments, 1g/L of the FeS_2-photocatalyst (synthesized
FeS_2 nanoparticles or FeS_2 nanoparticles modified with 0.2 wt% Pt) were suspended
in 50 mL of an aqueous solution containing 0.1 M Na_2S and 0.02 M Na_2SO_3 with pH
$\sim$ 13-14 (the experimental details are described in section 3.4.4). These experiments
have been performed using the MS measurement set-up.

Before the illumination, the time course of the H_2 (and other possible gaseous
compounds) formation was monitored in the dark until the signal becomes constant
(120-150 min). Afterwards, the light is switched on and the H_2 evolution was found
to start after 20-30 min irradiation. The H_2 evolution rate became nearly constant
after 40 min illumination (Figure 4.19). The light has been switched off after 9 h
irradiation, whereby a rapid decay of the H_2 evolution rate was observed and the
baseline was rapidly reached again. The H_2 evolution rate was determined from the
difference between the average of the values obtained in the part with so far constant
H_2 evolution rate and the baseline value (at the end of the measurement). In all
of the measurements, the data points measured at the end of each photocatalytic
reaction have been considered as the baseline. This is due to the fact that in some

cases (Figure 4.19a) the data points measured at the end of each photocatalytic reaction are found to be slightly higher than those at the very beginning monitored before the illumination.

All obtained H_2 evolution rates in this work have been calculated in this way. The H_2 evolution rate is found to be 5.53 µmol h^{-1} ($\zeta = 2.51 \times 10^{-2}$ %) in case of the synthesized FeS_2 nanoparticles and 9.56 µmol h^{-1} ($\zeta = 4.34 \times 10^{-2}$ %) for the Pt modified (0.2 wt%) nanoparticles.

4.5.5 H_2 Production with Pt loaded FeS_2-Nanoparticles

As shown in Figure 4.19 the modified FeS_2 nanoparticles show higher activity as compared to the unmodified ones. The effect of using Pt modification is already known in case of TiO_2 used as photocatalyst [129–131]. In this part of the work, the photocatalytic activity of the FeS_2 nanoparticles loaded with different weight % of Pt has been investigated. For this purpose, Pt-loaded FeS_2 nanoparticles have been prepared (detail in section 3.1.4).

The effect of the Pt loading on the photocatalytic H_2 evolution test has been studied using the GC measurement setup equipped with the gas chromatograph as the detection unit (GC-setup section 3.4.1). A set of experiments has been performed in a quartz glass photoreactor. The photoreactor was irradiated from the outside using an Osram XBO 450 W Xenon lamp without any filter (light intensity ~ 26 mW cm^{-2}). The photocatalytic H_2 evolution has been measured employing sulfide and sulfite as sacrificial electron donors. In a typical test, 1 g L^{-1} of the Pt-loaded FeS_2 was suspended in 60 ml of an aqueous solution containing 0.1 M $Na_2S \cdot 9\,H_2O$ and 0.02 M Na_2SO_3 (pH $\sim$ 13-14) as sacrificial reagents. The evolved H_2 gas was collected using a locking-type syringe and analyzed with the gas chromatograph.

Colloidal Pt nanoparticles have been used to prepare 0.01-, 0.1-,0.2-, 0.3-, 0.4-, 0.5- and 1 weight % of Pt loaded FeS_2-nanoparticles. The amount of evolved H_2 increased almost linearly as the function of the irradiation time (inset of Figure 4.20). However, in all of the test runs, the first trace of the H_2 evolution could only be detected after 90 min irradiation.

Figure 4.20 illustrates the comparison of the H_2 evolution rates of Pt loaded FeS_2-nanoparticles and their difference to the unmodified FeS_2-nanoparticles (black line).

The results in Figure 4.20 show that the Pt-loaded FeS_2-nanoparticles are photocatalytically more active than unmodified one. The 0.5 % Pt modification shows the highest activity. This was the reason that the 0.5 weight % of the loading
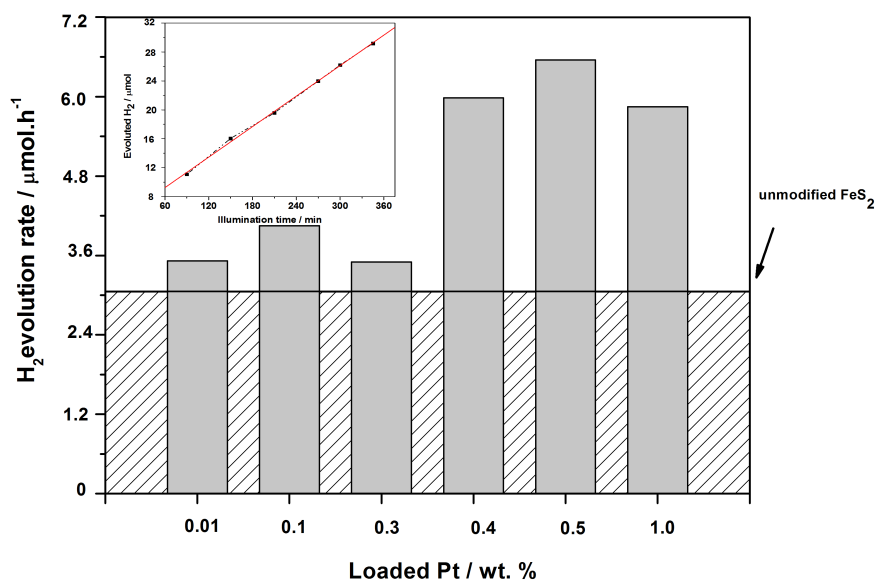
Figure 4.20: Photocatalytic H_2 evolution rates of the synthesized FeS_2 nanoparticles modified with colloidal Pt nanoparticles in different wt % in aqueous solution of 0.1 M Na_2S and 0.02 M Na_2SO_3 (pH 13.5-14), light source: 450 W xenon lamp ($I \sim 26\,\mathrm{mW\,cm^{-2}}$), Inset: H_2 evolution as the function of the illumination time in example of 0.1% Pt-loaded FeS_2.

material was chosen for the following co-catalyst modifications.

Generally, the results from these experiments (with GC-setup section 3.4.1) show lower activity as the results from MS-setup (section 3.4.2). It should be considered that the used Xenon lamp in this set-up was different from the one in the MS setup. Hence, the irradiance of the lamp was just around $26\,\mathrm{mW\,cm^{-2}}$(in case of the MS setup was around $110\,\mathrm{mW\,cm^{-2}}$).

4.5.6 H_2 Production with Co-catalyst loaded FeS_2

Since in this work it was very important to have an active H_2 evolution catalyst for the reduction of water, a series of co-catalyst loaded FeS_2 powders has been prepared. For this purpose commercial FeS_2-powders (from Sigma Aldrich) have been used and were modified with both noble metal and transition metal oxide catalysts. Platinum (Pt), Gold (Au), Cobalt (Co), Copper (Cu), Iridium (Ir), Chromium (Cr), Ruthenium (Ru), and Nickel (Ni) were loaded as pure metal or as metal oxide on these FeS_2-powders as co-catalysts and were used for the production

of hydrogen employing sulfide and sulfite as sacrificial electron donors.

Noble metal loading on the surface of FeS_2 was carried out by photodeposition, while the metal oxides were loaded onto FeS_2 by an impregnation method (see section 3.1.5). In a typical test, 0.05 g of Co- Cat/FeS_2 was suspended in 50 ml of an aqueous solution containing 0.1 M $Na_2S \cdot 9\,H_2O$ and 0.02 M Na_2SO_3 as sacrificial reagents. The reactor was irradiated from the outside for four hours with an Osram XBO 1000 W Xenon lamp in Müller LAX 100 lamp housing (with a cutoff filter for $\lambda > 420\,nm$, $I_{420-800} \sim 110\,mW\,cm^{-2}$). Hidden HPR20 mass spectroscopy (MS) was used to analyze on-line production of hydrogen gas (see fig. 3.6).

The photocatalytic H_2 production rate and the photonic efficiencies (ζ) for Co-Cat/FeS_2 are given in table 4.6. In this table the results are presented in the form of the calculated hydrogen production rates ($\mu mol\,h^{-1}$) and as photonic efficiencies (ζ). NiO/FeS_2 showed the highest photocatalytic activity for H_2 evolution with a formation rate of 14.65 $\mu mol\,h^{-1}$ ($\zeta = 6.66 \times 10^{-2}$ %) and RuO_2/FeS_2 exhibits a very low rate of 5.19 $\mu mol\,h^{-1}$ ($\zeta = 2.36 \times 10^{-2}$ %).

Table 4.6: Photocatalytic H_2 production rate and photonic efficiency (ζ) employing FeS_2 modified with different co-catalysts (0.5 wt%) under visible light irradiation, light source: 1000 W xenon lamp with a cut-off filter $\lambda > 420\,nm$ ($I_{420-800} \sim 110\,mW\,cm^{-2}$, 0.1 M $Na_2S \cdot 9\,H_2O$ and 0.02 M Na_2SO_3 have been used as reducing reagents.

Co-Cat/FeS$_2$	H$_2$ Production rate [$\mu mol\,h^{-1}$]	ζ [10^{-2}%]
NiO/FeS_2	14.65	6.66
Au/FeS_2	12.23	5.55
FeS_2	11.67	5.3
Cr_2O_3/FeS_2	11.53	5.24
CuO/FeS_2	11.48	5.21
CoO/FeS_2	10.36	4.71
IrO_2/FeS_2	9.10	4.13
Pt/FeS_2	8.41	3.82
RuO_2/FeS_2	5.19	2.36

4.6 Photocatalytic Water Splitting

4.6.1 Titanium Dioxide

For a better comparsion with the results obtained with α-Fe_2O_3 and FeS_2 the photocatalytic overall water splitting has also been investigated employing TiO_2 as the semiconductor. The band gap of rutile TiO_2 is ca. 3.0 eV and of anatase TiO_2 is ca. 3.2 eV [132] and the position of the potentials of the conduction and valence band are suitable for the evolution of H_2 and O_2. TiO_2 Aeroxide P25 has been modified with Pt and applied for the overall water splitting experiments. The Pt-loaded TiO_2 photocatalyst (Pt/TiO_2) has been prepared by the impregnation method using an aqueous H_2PtCl_6 solution and dried at 373 K for 24 hours.
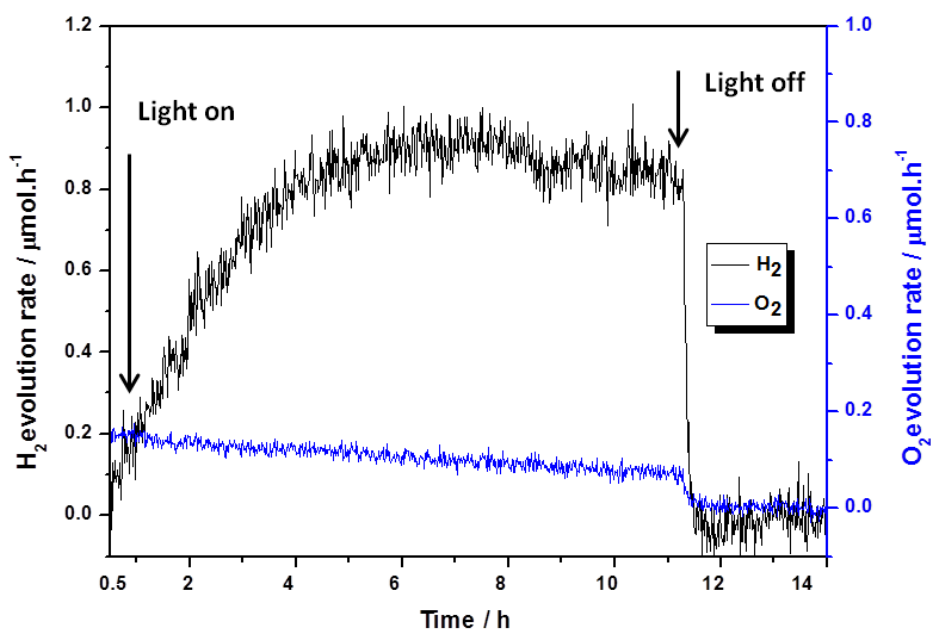
Figure 4.21: Photocatalytic overall water splitting employing Pt-loaded TiO_2 (0.5 wt % Pt) suspended in 50 mL pure water, photocatalyst concentration: $1\,g\,L^{-1}$, light source: 1000 W xenon lamp with an intensity of $40\,mW\,cm^{-2}$.

Figure 4.21 shows the evolution rates of H_2 and O_2 employing Pt/TiO_2 (0.5 wt % Pt) in pure water. The time course of the H_2 evolution was different from the H_2 production curves obtained in the presence of the sacrificial reagents. In this case, it took more than 4 h irradiation until the H_2 evolution rate became nearly constant. Because of this difference, the H_2 evolution rate could be determined

either from the difference between the average of the values obtained in the part with so far constant H_2 evolution rate and the baseline value (at the end of the experiment), or from the average value of the data points of the illumination data and the baseline value (at the end of the experiment). For the first case, the H_2 evolution rate was determined to be 8.33 µmol h^{-1} and for the second case 5.18 µmol h^{-1}.

The O_2 evolution rate was determined to be 0.14 µmol h^{-1}. This value does not confirm the stoichiometric ratio of H_2- and O_2- evolution during the photocatalytic overall water splitting. In general, for a stoichiometric overall water splitting the H_2 amount should be twice as high as the O_2 amount. Nevertheless, this result indicates that Pt/TiO$_2$ is able to split pure water into H_2 and O_2.

4.6.2 Z-Scheme System

As already described in section 4.6.1 some experiments considering the overall water splitting have been performed employing Pt loaded-TiO$_2$ as the photocatalyst. TiO$_2$ mostly absorbs the UV part of the solar spectrum which makes it difficult to harvest the sunlight effectively. Therefore the Z-scheme water splitting is a good strategy, since a wider range of visible light can be used. This approach is based on the fact that usually semiconductors either exhibit water oxidation or water reduction properties. In this work, modified-FeS$_2$ has been used for the water reduction and modified-α-Fe$_2$O$_3$ for the water oxidation.

The Z-scheme water splitting experiment has been performed employing the most active Co-Cat/-FeS$_2$ and the most active Co-Cat/Fe$_2$O$_3$ under visible light irradiation (Figure 4.22). In this case, NiO/FeS$_2$ was used for the H_2 evolution and RuO$_2$/Fe$_2$O$_3$ for the O_2 evolution. Subsequently, 0.011 µmol h^{-1} H_2 and 0.022 µmol h^{-1} O_2 were produced. In this case the electron transfer between the different photocatalyst particles can only provided through direct contact enabling the interparticle electron transfer.

Furthermore, the iodate/iodide (IO_3^-/I^-) system has been used as shuttle redox mediator to provide better electron transfer in the system. The photocatalytic oxidation of water to O_2 and the reduction of IO_3^- to I^- proceeded over the Co-Cat/Fe$_2$O$_3$ photocatalysts, while on the other hand, the photocatalytic reduction of water to H_2 and the oxidation of I^- to IO_3^- proceeded over the Co-Cat/FeS$_2$ photocatalysts (Figure 4.23 shows one of the examples).
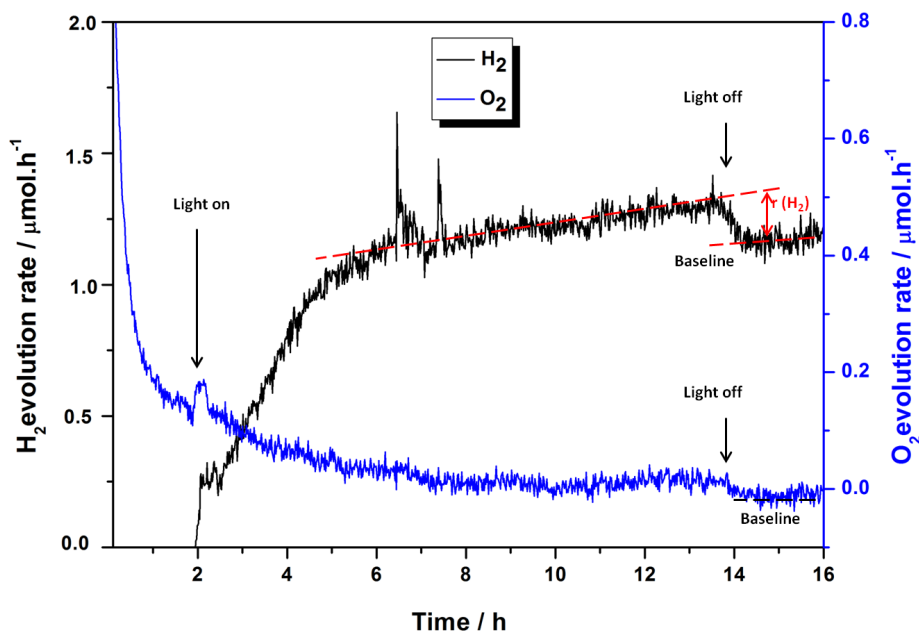
Figure 4.22: Photocatalytic overall water splitting under visible light irradiation; as photocatalysts a mixture of NiO/FeS_2 and RuO_2/Fe_2O_3 was employed and suspended in $50\,mL$ pure water, each photocatalyst concentration: $1\,g\,L^{-1}$, light source: 1000 W xenon lamp with a cut-off filter $\lambda > 420\,nm$ ($I_{420-660} \sim 66\,mW\,cm^{-2}$)

Table 4.7: Photocatalytic H_2 and O_2 production rates employing FeS_2 and Fe_2O_3 modified with different co-catalysts (0.5 wt%) under visible light irradiation, IO_3^-/I^- has been used as shuttle redox mediator wherever stated.

Photocatalysts	Aq. Solution	H_2 [$\mu mol\,h^{-1}$]	O_2 [$\mu mol\,h^{-1}$]
NiO/FeS_2-RuO_2/Fe_2O_3	-	0.011	0.022
NiO/FeS_2-CoO/Fe_2O_3	2 mM I^- 2.5 mM IO_3^-	0.62	0.032
NiO/FeS_2-RuO_2/Fe_2O_3	0.1 M I^- 2.5 mM IO_3^-	0.25	0.098
NiO/FeS_2-RuO_2/Fe_2O_3	0.1 M I^- 0.1 M IO_3^-	0.23	0.15
NiO-Pt/FeS_2-RuO_2-Pt/Fe_2O_3	0.1 M I^- 2.5 mM IO_3^-	0.20	0.105
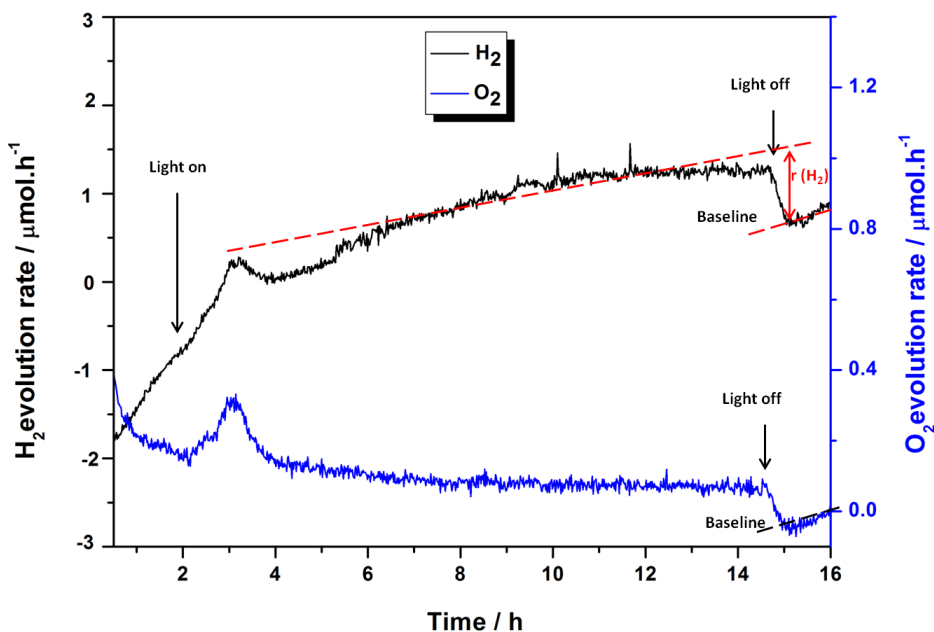
Figure 4.23: Photocatalytic overall water splitting in the presence of IO_3^-/I^- as shuttle redox mediator under visible light irradiation; as photocatalysts a mixture of $NiO-Pt/FeS_2$ and RuO_2-Pt/Fe_2O_3 was employed and suspended in 0.1 M I^-/2.5 mM IO_3^- (pH $\sim$ 7), each photocatalyst concentration: $1\,g\,L^{-1}$, light source: 1000 W xenon lamp with a cut-off filter $\lambda > 420\,nm$ ($I_{420-660} \sim 66\,mW\,cm^{-2}$)

Table 4.7 presents the H_2 and O_2 evolution rates for the Z-scheme water splitting systems. The first line shows the results obtained in pure water. The following lines present the results obtained in the presence of IO_3^-/I^- as shuttle redox mediator. The concentration of IO_3^-/I^- shuttle redox mediator has been varied to find the best combination with the highest activity.

4.7 Analysis of the Reaction Mixture

4.7.1 Photocatalytic O_2 production in presence of Fe^{3+}/Fe^{2+}

Oxygen production has been studied in the presence of 0.1 M aqueous $Fe(NO_3)_3$. $-9\,H_2O$. In this case, the Fe^{3+} ion acts as sacrificial oxidizing agent (electron acceptor) and the valence band holes oxidize water to produce O_2. The concentration changes of Fe^{3+} and Fe^{2+} in solution were determined from UV-Vis absorption spectra as described in section 3.2.8. For this purpose, the comparison of the solution
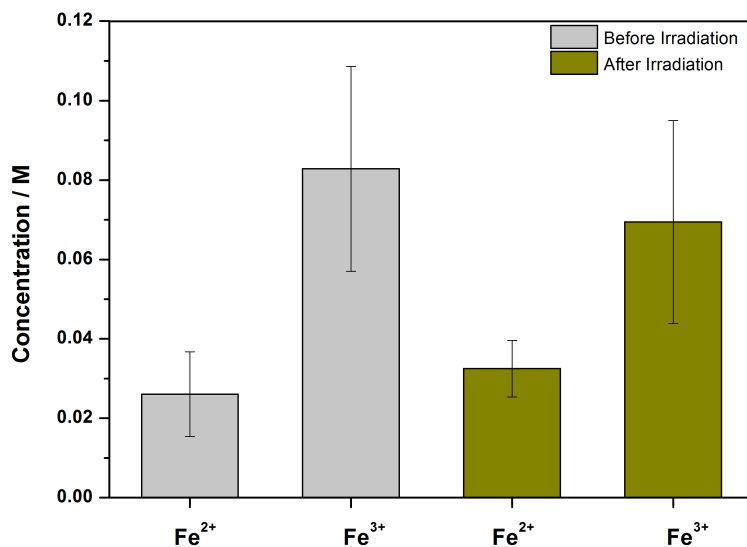
Figure 4.24: The concentrations of Fe^{2+} and Fe^{3+} before and after the photocatalytic reaction. The photocatalytic reaction of $1\,g\,L^{-1}$ α-Fe_2O_3 suspended in 0.1 M $Fe(NO_3)_3 \cdot 9\,H_2O$ and irradiated for 12 h by a xenon lamp.

before the irradiation and after the photocatalytic reaction has been studied.

Figure 4.24 presents the concentration changes of Fe^{3+} and Fe^{2+} before and after a photocatalytic oxygen evolution test. In this case, $1\,g\,L^{-1}$ α-Fe_2O_3 have been suspended in an aqueous solution of 0.1 M $Fe(NO_3)_3 \cdot 9\,H_2O$ (pH $\sim$ 1.5-2). Subsequently, the suspension was moved to the photoreactor and stirred for 30 min. Furthermore, the suspension was purged with Ar for 60 min and then a sample of the suspension has been taken to determine the concentrations of Fe^{3+} and Fe^{2+} before the irradiation. Afterwards, the photoreactor was connected to the mass spectroscopy and illuminated for 12 h. During this time the O_2 evolution rate was $0.08\,\mu mol\,h^{-1}$ O_2, which corresponds to $19.22\,\mu mol\,L^{-1}$ O_2 formed during the entire illumination time from this suspension. The second sample was taken after the irradiation to determine the concentrations of Fe^{3+} and Fe^{2+} after the irradiation. The amount of detected Fe^{3+} ion is reliable since the initial concentration of iron nitrate was 0.1 M. The experimental error was within 25 % through all the experiments between the values calculated from the amount of oxygen evolution and from the absorption spectra to calculate the concentration of Fe^{2+}/Fe^{3+} .

The fact that Fe^{2+} ion was already detected before the irradiation could be explained as follow; some of the already existing Fe^{3+} ions in the solution reduced and produced Fe^{2+} ions [133]. The second source of Fe^{2+} ion could be hematite. It is known that Fe_2O_3 in aqueous media exist as FeOOH and this could in acidic media react as follow and produce Fe^{2+} ions[134]:

$$FeOOH + e^- + 3\,H^+ \longrightarrow Fe^{2+} + 2\,H_2O \qquad (4.5)$$
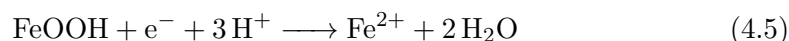
as mentioned the pH of the reaction media was 1.5-2.

Altogether in this reaction 0.013 M of Fe^{3+} was consumed and 0.006 M produced. Accordingly, the concentration ratio between consumed Fe^{3+} and produced Fe^{2+} is estimated to be $2:1$. Obviously, the amount of produced O_2 in these experiments is very lower than the produced Fe^{2+} ions.

4.7.2 Photocatalytic H_2 production in presence of $S^{2-}/SO_3{}^{2-}$

FeS_2 is not stable in aqueous solutions under irradiation and undergoes anodic dissolution (see reaction 2.5) [135, 136]. In the present work, S^{2-} and $SO_3{}^{2-}$ have been used as sacrificial reagents. These species prevent FeS_2 from the photocorrosion acting as hole scavengers, and also promote hydrogen evolution through making up half of the water splitting reaction.

However, it is important to see how the concentration of these ions changes during the reactions. For this purpose, the solution has been studied before the irradiation and after the photocatalytic reaction. These investigations have been performed by means of High Performance Ionic Chromatography (HPIC) and the Photometric Cuvette Test.

As already described (section 3.4.4) in a typical photocatalytic test 0.1 M Na_2S. $-9\,H_2O$ and 0.02 M Na_2SO_3 (with pH $\sim$ 13-14) were used as sacrificial reagents. In this part of work, $1\,g\,L^{-1}$ FeS_2 has been suspended in an aqueous solution which contained the same concentration of Na_2S and Na_2SO_3. The suspension was moved to the photoreactor and first stirred for 30 min; subsequently purged with Ar for 30 min. At this point, a sample of the suspension has been taken for the determination of the concentrations before the irradiation (C_0). Finally, the photoreactor was connected to the mass spectroscopy and irradiated for 4.5 h. During this time the H_2 evolution rate was $7.7\,\mu mol\,h^{-1}$ H_2, which corresponds to a formation of 0.7 mM H_2 from this suspension. The second sample was taken after the irradiation for the determination of the concentrations of S^{2-}, $SO_3{}^{2-}$, $SO_4{}^{2-}$, and $S_2O_3{}^{2-}$ after the

irradiation (C_t).

The S^{2-} concentrations have been determined via cuvette test since the IonPac AS9-HC column of the HPIC is not able to detect this anion. The concentrations of SO_3^{2-} have been detected via HPIC and SO_4^{2-} and $S_2O_3^{2-}$ could be detected as the products. Figure 4.25 presents these results in form of the concentration of the anions before and after the irradiation. Figure 4.25 depicts that S^{2-} concentration
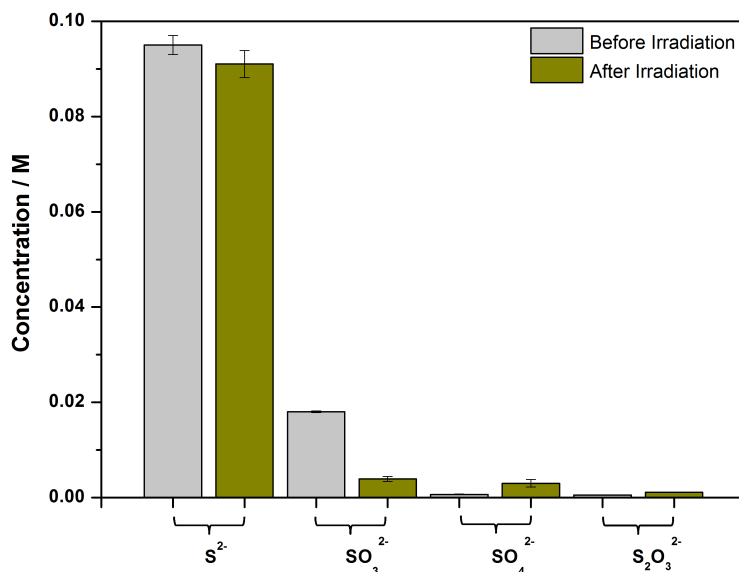
Figure 4.25: The concentrations of S^{2-}, SO_3^{2-}, SO_4^{2-}, and $S_2O_3^{2-}$ before and after the photocatalytic reaction. The photocatalytic reaction of $1\,g\,L^{-1}$ FeS_2 suspended in 0.1 M $Na_2S \cdot 9\,H_2O$ and 0.02 M Na_2SO_3 (pH $\sim$ 13-14) and irradiated for 4.5 h by a xenon lamp.

decreased from 0.095 M to 0.091 M, the SO_3^{2-} decreased from 0.018 M to 0.004 M while 0.003 M SO_4^{2-} and 0.001 M $S_2O_3^{2-}$ have been produced. The amounts of produced products is smaller than the amount of consumed sacrificial reagents. The concentrations of the products are five times higher than the concentration of the produced H_2.

To clarify the role of the sacrificial reagents and the product of this reaction further experiments have been conducted. Two diluted suspensions, the first one with 0.01 M Na_2S (pH $\sim$ 6.5-7.5) and the second one with 0.01 M Na_2SO_3 (pH $\sim$ 8-9) have been prepared. In both experiments $1\,g\,L^{-1}$ pyrite was used as the photocatalyst and the photocatalytic reaction was carried out for 48 h under illumination

with a xenon lamp.

In both experiments $SO_4{}^{2-}$ could already be detected before the illumination even started ($SO_4{}^{2-}$ should be one of the main products of the photocatalytic reaction). The explanation of this behavior is the chemistry of pyrite in water[30, 37]. According to the following reaction FeS_2 in water produce Fe^{3+} and $SO_4{}^{2-}$:

$$FeS_2 + 8\,H_2O \longrightarrow Fe^{3+} + 2\,SO_4{}^{2-} + 16\,H^+ + 15\,e^- \tag{4.6}$$
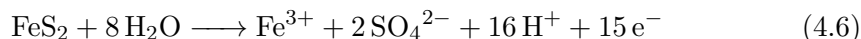
Hence the source of $SO_4{}^{2-}$ before the irradiation is pyrite itself. The following results from these two experiments have been achieved:

Suspensions with 0.01 M Na$_2$S: The concentration changes of S^{2-} and $SO_4{}^{2-}$ have been determined via photometric cuvette test. During this reaction, the concentration of S^{2-} is found to decrease and the concentration of $SO_4{}^{2-}$ increased (table 4.8). Here the S^{2-} concentration before the illumination shows a smaller value than expected. This could be explained by the fact that some of the S^{2-} anions adsorbed at the surface of FeS_2. In most experiments, the dark adsorption of acceptors or donors at the surface of the photocatalyst have been reported [30, 137]. All in all 2.6 mM H_2 has been produced.

Table 4.8: The concentrations of S^{2-} and $SO_4{}^{2-}$ before and after the photocatalytic reaction. The photocatalytic reaction of $1\,g\,L^{-1}$ FeS_2 suspended in 0.01 M $Na_2S \cdot 9\,H_2O$ and irradiated for 48 h by a xenon lamp.

	C_0 [mM]	C_t [mM]
S^{2-}	2.23	2.04
$SO_4{}^{2-}$	5.68	6.5

Suspensions with 0.01 M Na$_2$SO$_3$: The concentration changes of $SO_3{}^{2-}$ and $SO_4{}^{2-}$ have been determined via photometric cuvette tests. In this experiment, the concentration of $SO_3{}^{2-}$ has been decreased during the photocatalytic reaction and the concentration of $SO_4{}^{2-}$ has been increased.

Based on all the facts concerning the chemistry of pyrite in water and these results which are reported here stoichiometric analyses of the H_2 production reaction is not possible. Nevertheless, these results indicate which products have been produced and help to clarify the mechanism of the H_2 production with FeS_2 in presence of sulfide and sulfite.

5 Discussion

In this chapter, the results of the experimental part will be discussed and will be interpreted in detail.

In the first section, the materials of the present study and their characteristic properties will be discussed. In the following sections, the photoelectrochemical properties of hematite- and pyrite- electrodes will be discussed. The photocatalytic results will be discussed in two separat sections. First, the photocatalytic oxygen or hydrogen production in the presence of suitable sacrificial reagents will be discussed. Here the role and the optimum loading percent of the co-catalysts will be discussed, follow by the discussion of the role of used sacrificial reagents for particular O_2 or H_2 evolution reactions. The last section deals with photocatalytic overall water splitting, applying either one photocatalyst or two photocatalysts in the Z-scheme system.

5.1 Materials

5.1.1 Hematite (α-Fe$_2$O$_3$)

The synthesized Fe_2O_3 nanoparticles exhibit hematite crystal structure with a particle size distribution between 20-30 nm (see section 4.1.1). The optical characterization of these hematite nanoparticles indicates that they absorb the visible region of the light spectrum. The calculated bandgap energy was between 1.9 and 2.1 eV corresponding to an onset wavelenght of $\lambda \sim 650$ to 590 nm.

The commercially used Fe_2O_3 was obtained from io-Li-tec Germany and also declared the hematite crystal structure (see section 4.1.2). The particle size distribution of this powder was between 20 - 40 nm. The bandgap energy of commercially used α-Fe$_2$O$_3$ was around 2.1 eV for the indirect transition. All of the bandgap energy values are in good agreement with the literature, that is 2 - 2.2 eV[4].

According to the majority of reports, hematite has an indirect band gap transition and the direct transition is forbidden [4, 19–22]. Figure 5.1 presents a comparison between the Tauc-plots of the modified Kubelka-Munk function of both the direct

78
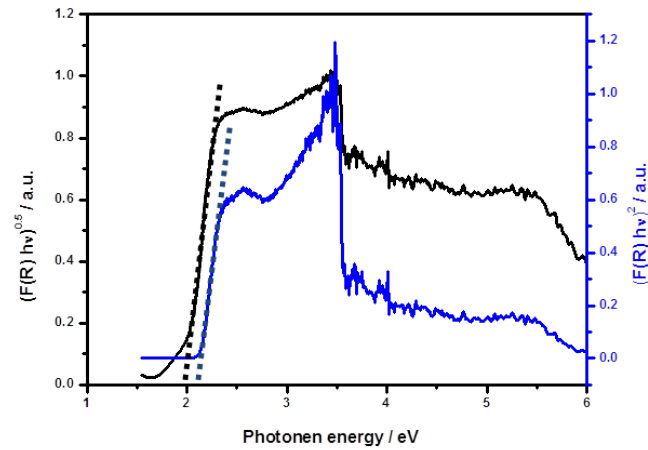
Figure 5.1: Diffuse reflectance spectra of commercial Fe_2O_3 powder, the comparison between the Tauc-plots of the modified Kubelka-Munk function versus the photon energy for indirect allowed transition (black graph) and the forbidden direct transition (blue graph).

and indirect transition states of the hematite. Misho and Murad investigated the absorption and transmission spectra of Fe_2O_3, FeS_2, and FeS [22]. According to their work, the forbidden direct transition for Fe_2O_3 is between 1.63 - 1.86 eV. The value for the direct transition in Figure 5.1 is ~ 1.8 eV.

The XRD pattern of both synthesized and commercially used Fe_2O_3 show no other impurities such as goethite (FeOOH), magnetite (Fe_3O_4) or maghemite (γ-Fe_2O_3) in the crystal structure. All of the reflection peaks belong to the alpha phase of the Fe_2O_3. Because the main diffraction peaks of the gamma phase are at the positions of $2\theta = 30.2, 35.6, 43.2, 57.3$, and $62.9°$ (PDF 039-1346).

5.1.2 Pyrite (FeS$_2$)

The synthesized FeS_2 nanoparticles exhibit pyrite crystal structure with a particle size distribution between 20 to 35 nm (see section 4.2.1). The UV-Vis and UV-Vis-NIR absorption spectra of pyrite nanoparticles (self-prepared) show a broad absorption of the light spectrum (Figure 4.8). This could expected for a gray in color materials like pyrite, which absorb a broad range of the light spectrum. The calculated bandgap energy was around 0.9 eV, which corresponds to $\lambda = 1370$ nm.

The commercially used FeS_2 obtained from Sigma-Aldrich also indicated pyrite crystal structure (see section 4.2.2). The bandgap energy of commercially used

pyrite was calculated to be around 1.1 eV corresponding to $\lambda = 1127$ nm (see Figure 4.10). The bandgap energy values of both synthesized and commercially used FeS$_2$ are in good agreement with the literature, that is 0.9 ± 0.2 eV [16, 30, 37, 38].

According to the majority of reports, pyrite has an indirect band gap transition and the direct transition is forbidden. In some reports, the forbidden direct band of pyrite is calculated and is reported to be in the range of 1.5 to 2.6 eV. However, our results show the indirect allowed transition and do not show the forbidden indirect transition. The comparison between the Tauc-plots of the modified Kubelka-Munk function of both the direct and indirect transition states of the pyrite are presented in appendix 4.

The XRD pattern of both synthesized and commercially used FeS$_2$ show only the characteristic reflection peaks of the cubic phase of FeS$_2$ (pyrite). FeS$_2$ could also exist as marcasite, pyrrhotite, or troilite. The characteristic reflection peaks of marcasite are usually at the positions of $2\theta = 33.5, 39, 47.8,$ and $52°$ (PDF 02-1342), while for pyrrhotite at $2\theta = 30, 34, 43.5, 53.2, 65,$ and $71°$ (PDF 17-0201), and for troilite at $2\theta = 30, 34, 44, 54, 57, 65,$ and $51.5°$ (PDF 01-1274).

5.2 Photoelectrochemical Properties of Hematite

The electrochemical behavior of hematite was investigated employing α-Fe$_2$O$_3$ electrodes, which were prepared via dip-coating from the colloidal suspension. In this section, the current vs. potential properties of the α-Fe$_2$O$_3$ electrodes will be discussed, followed by discussion of the results obtained from impedance measurements (flat-band potentials and donor densities).

5.2.1 Current-Potential

Current-potential curves for α-Fe$_2$O$_3$ electrodes are presented in the section 4.3.1. The first investigations were performed on α-Fe$_2$O$_3$ electrodes obtained at different calcination temperatures (400 °C, 500 °C, 600 °C, and 700 °C). These results are presented in Figure 4.11. In the cathodic potential area a particular response to the potential could not be observed. Reduction of dissolved oxygen could be one of the possible reactions in the cathodic currents [41]. In addition, there is no response to the light (photoactivity) detected in the negative potentials.

However, the anodic currents show a different behavior. In all of the experiments, a large rise in anodic current appeared under illumination. The blank tests on FTO
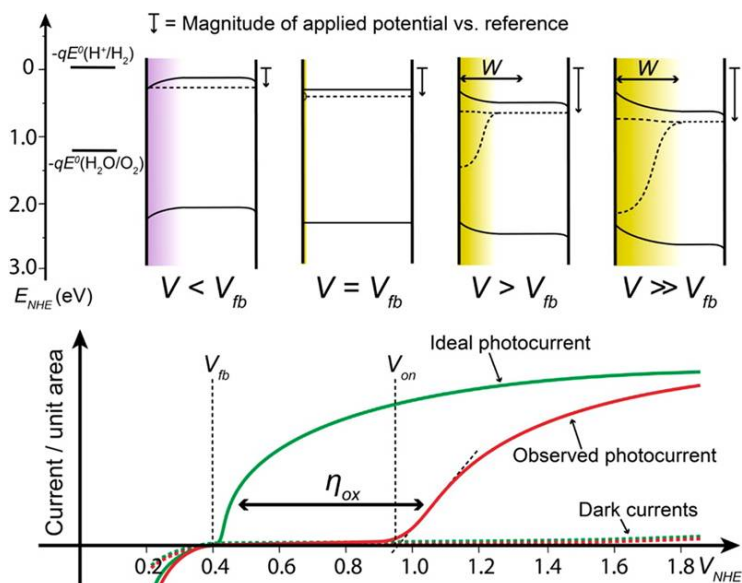
Figure 5.2: Energy diagram of an n-type semiconductor photoanode under polarization using a potentiostat at different potentials (V) relative to the flat band potential (here V_{fb}) and illustration of the different situation relating to the photocurrent measurement: Accumulation layer when $V < V_{fb}$ (purple shaded region), flat band situation ($V = V_{fb}$), depletion layer formation when $V > V_{fb}$ (yellow shaded region and W show width of this layer) and finally inversion layer. Bottom: the illustration of ideal photocurrent density versus applied potential curves are presented relative to the flat band potential (V_{fb}), the overpotential for the oxidation reaction, η_{ox}, is present for a typical electrode with an onset of photocurrent at V_{on}. Reprinted with permission from [42] ©2013 American Chemical Society.

glasses, which were thermally treated similar to α-Fe$_2$O$_3$ electrodes, indicated that the photoeffect is only due to the Fe$_2$O$_3$ itself.

As mentioned, the plateau current and the onset potential are the two critical parameters which should be considered to interpret these results. The onset of steady-state photocurrent, which usually appears a few tenths of a volt anodic to the flat-band potential depicts the condition in which enough band bending occurs in the semiconductor space charge layer (see top of the Figure 5.2). In this case, there will be a sufficient competition between the hole transfer to the reduce reagents in the solution and other processes [133]. In the ideal case, the overpotential for the electrochemical reaction approaches should be zero and it should be possible to measure the photocurrent at all potentials more anodic than flat band potential

(and this will be $\sim$ 0.3-0.4 V, see the green curve in Figure 5.2). However, in the real case, the system exhibit an overpotential and the photocurrent could not observed directly anodic of flat band potential but after an additional potential has been applied (and this will be $\sim$ 0.8-1.0 V, see red curve in Figure 5.2) [42].

The results show a cathodic shift of the onset potentials when the calcination temperature is increased. For example, the onset potential of α-Fe$_2$O$_3$ electrode obtained at $400\,^\circ$C calcination temperature is 1.45 V vs. RHE (in Figure 4.11 0.75 V vs. NHE at pH 13) while the onset potential for α-Fe$_2$O$_3$ electrode obtained at $600\,^\circ$C is 0.91 V vs. RHE (in Figure 4.11 0.2 V vs. NHE at pH 13). Based on this fact it could be assumed that the charge transfer to the solution is improved and as result, the electrocatalytic oxygen evolution started at the lower potentials. This means the decreasing of the overpotential of the water oxidation reaction. In the next paragraphs, we will interpret this fact and explain the possible reasons for this behavior.

The second important parameter from the I-V curves is the plateau current, which indicates the amount of photogenerated holes reaching SCLJ. The results show an effective rise in the plateau current when the calcination temperature is increased. For example, for α-Fe$_2$O$_3$ electrodes calcined at $400\,^\circ$C, the photocurrent onset at about 0.2 V giving $J = 0.1\,\mathrm{mA\,cm^{-2}}$ while for α-Fe$_2$O$_3$ electrodes calcined at $700\,^\circ$C, $J = 0.3\,\mathrm{mA\,cm^{-2}}$. Altogether the thermal treatment improves the efficiency of the electrodes.

Sivula *et al.* present in a review article [4] amongst others the state of the art hematite photoelectrodes and efforts to improve the efficiency of them. The investigations on hematite photoelectrodes provide two effective strategies to optimize the efficiency of hematite performance in PEC (Figure 5.3). These two strategies are: i) improving the quality of the electrode morphology, which leads to a rise in the photocurrent density, and ii) surface chemistry and surface treatments, which leads to a decrease in the essential overpotential for the water splitting. These two strategies are presented in the Figure 5.3.

The results presented in the section 4.3.1 indicate that at least one of the issues of the solar water splitting with hematite could be overcome in this work. The overpotential measured in some experiments is clearly decreased (see Figure 4.12 and and Figure 4.11 for the electrodes calcined at $600\,^\circ$C and $700\,^\circ$C). This should be considered even though the photocurrent density in the experiments was low, because it was at least possible to improve this issue in some experiments (with higher calcination temperatures). Indeed compared to the most recently reported studies
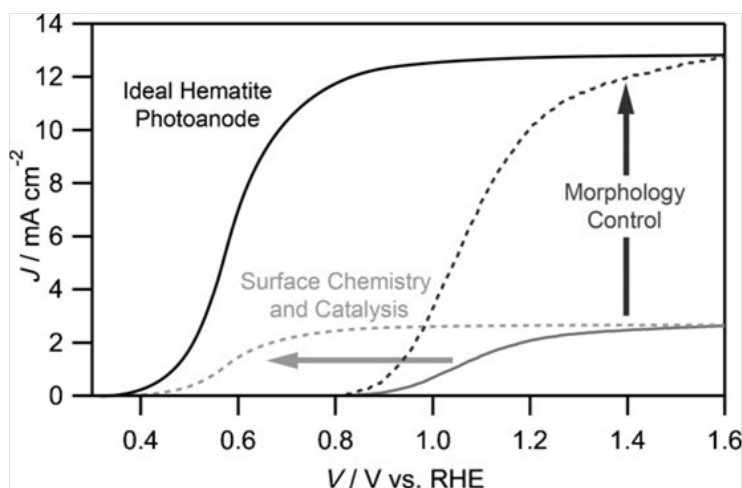
Figure 5.3: Two strategies for improving hematite performance; i) Morphology control, ii) Surface chemistry and catalysis; solid black trace: performance of an ideal hematite photoanode, solid grey trace: performance of state of the art hematite photoanode, Reprinted with permission from [4] ©2011 John Wiley & Sons.

about hematite photoelectrodes, the electrodes in this work are produced simply via dip-coating, and no further treatments, such as surface chemistry treatment [45], adding or doping catalysts [47, 138, 139], adding sacrificial reagents into the electrolyte [140], were performed. For example, Tilley *et al.* [47] could measured a photocurrent over 3 mA cm^{-2} at 1.23 V vs. RHE for hematite photoanode (under AM1.5G 100 mW cm^{-2} simulated sunlight). The improvement in performance of the hematite is succeeded due to the using nanostructured hematite and using IrO$_2$ as the catalyst.

Improvement of the photoactivity by annealing is reported by Sivula *et al.* in 2010 [18]. The authors prepared mesoporous hematite photoanodes by means of a solution-based colloidal approach. They report that high temperature (700 °C and 800 °C) thermal treatment leads to an increase in the particle size, and this changed the optical properties of the films by the increasing the absorption coefficient up to a factor of 2. In fact in the present study, an increase in the calcination temperature lead to the color change of the hematite photoanodes from red to dark red. The diffuse reflectance measurements of hematite electrodes indicate an increase in the F(R) with a rise in the calcination temperature. The diffuse reflectance spectra of hematite electrodes and their determined band gap energies are presented in Appendix 5.

The second relevant point which Sivula *et al.* mentioned in their report is the effect of FTO glass. Their investigations showed that upon inreasing the sintering temperature the Sn atoms could diffuse from the FTO substrate into the Fe_2O_3. Thereby, Sn^{4+} could act as electron donating substitutional impurities. Impurity doping is known as a convenient method for improving the photocatalytic performance. Furthermore, donor doping such as Ti^{4+} [141], Sn^{4+} [138], and Si^{4+} [142] shows a positive effect on the photoactivity of hematite photoanodes.

The last point in this section is the stability of the hematite photoanodes. In the present study, all of the photoelectrochemical investigations were performed in basic medium (0.1 M NaOH). In one of the first investigations on hematite as photoanode, Hardee and Bard [41] reported on the instability of iron oxide electrodes in acidic media. In the acidic solution (pH<4) Fe_2O_3 will be dissolved slowly. Indeed iron oxide in an acidic solution will be dissolved according to the following reaction:

$$Fe_2O_3 + 6\,H^+ \longrightarrow Fe^{3+}(aq) + 3\,H_2O \tag{5.1}$$
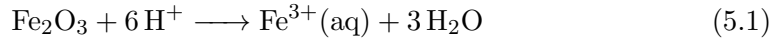
A further issue which will be discussed in section 5.3.4 about the pyrite electrodes is the photocorrosion. Photogenerated holes could corrode Fe_2O_3 in acidic media according to the following reaction:

$$6\,h^+ + Fe_2O_3 \longrightarrow 2\,Fe^{3+}(aq) + \frac{3}{2}\,O_2 \tag{5.2}$$
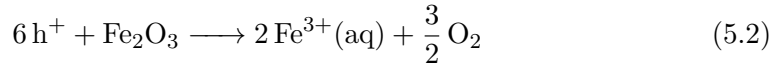
Further investigations show that Fe_2O_3 photoelectrodes are stable against photocorrosion if the oxidized species of the redox couple are presented in the reaction [133]. However based on these critical points about the stability of the Fe_2O_3 electrodes in acidic media, the decision was made that all of the photoelectrochemical studies in this work were performed in basic solution.

5.2.2 Flat-band Potentials and Donor Densities

The determined flat-band potentials of α-Fe_2O_3 electrodes are in good agreement with the reported values in the literature, which is reported to be 0.53 V vs. RHE by Le Formal *et al.* [124] or 0.4 V vs. RHE by Dare-Edwards *et al.* [28]. However, in the literature other values for the flat-band potential of Fe_2O_3 exist as well [24]. In some reports it is not clear whether or not the deviation of the pH dependence of the flat-band potential from -59 mV/pH is considered. For example Quinn *et al.*

reported a value of -0.67 V vs. SCE (in 2M NaOH) [143].

In addition, the donor densities of undoped Fe_2O_3 photoanodes obtained in this work correspond to the values reported in the literature [24, 124, 144]. The (N_D) was $1.0 \times 10^{19}\,\mathrm{cm^{-3}}$ for α-Fe_2O_3-electrode obtained at $400\,°C$ and $3.23 \times 10^{18}\,\mathrm{cm^{-3}}$ for α-Fe_2O_3-electrode obtained at $600\,°C$. Some reported N_D values for hematite electrodes are summarized as follows: $7.1 \times 10^{20}\,\mathrm{cm^{-3}}$ for Si-Fe_2O_3 (by Le Formal *et al.* [124]), $5 \times 10^{18}\,\mathrm{cm^{-3}}$ for TiO_2-Fe_2O_3 (by Dare-Edwards *et al.* [28]), and $1.0 \times 10^{18}\,\mathrm{cm^{-3}}$ for undoped Fe_2O_3 (by Kennedy and Frese [145]).

5.3 Photoelectrochemical Properties of Pyrite

The electrochemical behavior of both FeS_2-electrodes prepared from natural pyrite and commercially available FeS_2-powder was investigated (more information about the electrodes are described in section 3.1.7). At this point, the current vs. potential properties of the natural pyrite will be discussed. For this reason, it will be better to consider just one of the CV curves from the Figure 4.14.
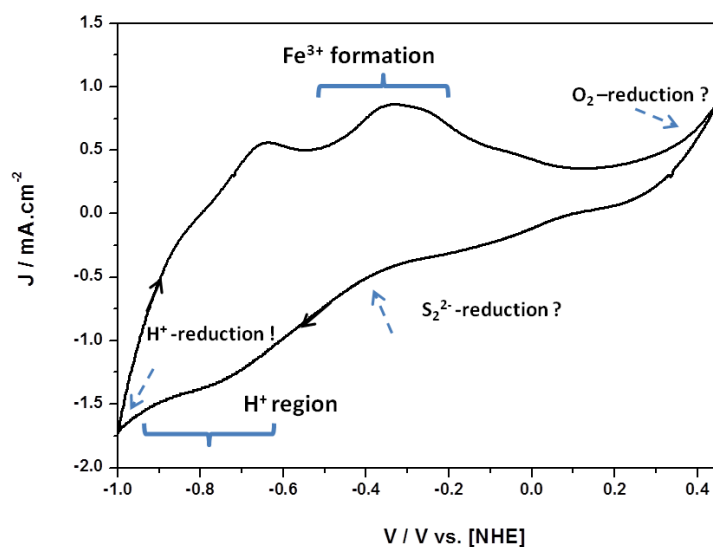
Figure 5.4: Cyclic voltammogram of the natural pyrite electrode in the dark (0.1 M NaOH used as electrolyte, pH 13). All possible or assumed reaction regions are labeled.

Figure 5.4 presents one of the measured voltammograms of the natural pyrite in the dark. In this case, the electrochemical behavior of pyrite in the dark seems to be similar to that of a metal, as blocking of currents was not recognized during

the measurements. This behavior is usually expected from a good and smooth semiconductor electrolyte junction.

For comparison, Figure 5.5a. presents a typical cyclic voltammogram for a reversible single electrode. This figure illustrates how a typical CV curve in case of perfect contact should be expected. Furthermore, in Figure 5.5b. two cyclic voltammograms for a metal (here platinum) in different applied potential range are presented.

For the interpretation of the voltammogram (Figure 5.4), first, the possible reactions in cathodic and anodic potential will be discussed, followed by the explanation of the photocurrent behavior. At end of this section, the impedance measurement results will be discussed.

Figure 5.5: a) A typical cyclic voltammogram recorded for a reversible single electrode, b) Typical cyclic voltammogram for a metal (here platinum) in different applied potential range.[146].

86

5.3.1 Anodic Potential (Positive Potential)

In all of the voltammograms (in Figure 4.14), a peak which increases as a function of the number of cycles could be observed. This peak is labeled as the Fe^{3+} formation region in the Figure 5.4 and could be correlated to the reversible potential of Fe(II)/Fe(III) ($E^0 = 0.77$ V (see reaction 5.3) [135].
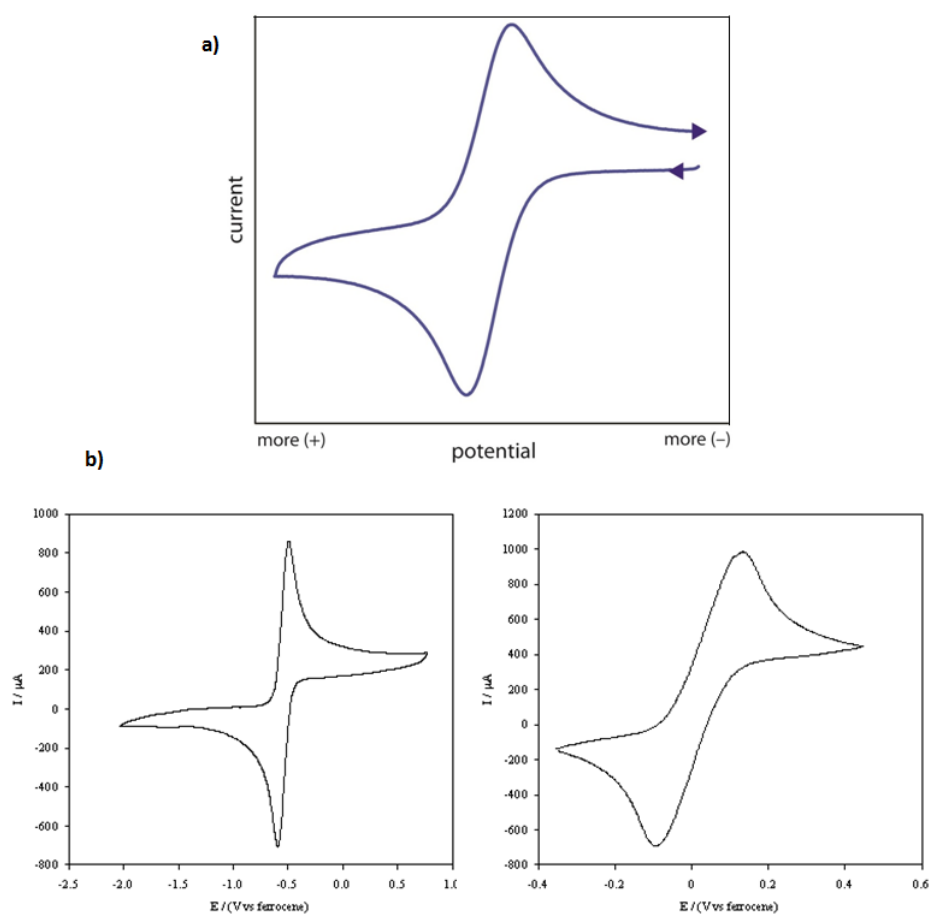
$$Fe^{3+} + e^- \rightleftharpoons Fe^{2+} \tag{5.3}$$

At the more positive potential region (O_2 reduction region in the Figure 5.4) two possible reactions could occur. One of these could be the oxygen reduction reaction because all of the measurements were carried out in the presence of air. In aqueous solutions this reaction typically occurs as follows: the direct 4-electron reduction pathway from O_2 to H_2O or the 2-electron reduction pathway from O_2 to hydrogen peroxide (H_2O_2)[147].

The second possible reaction in this region is a corrosion reaction (reaction 4.6). Based on this reaction SO_4^{2-} and Fe^{3+} will be formed and a reddish brown film will be produced (see Figure 5.7). The color of the film could be from the formation of Fe(III)-oxide. At this point, no oxidation of H_2O to O_2 could be assumed.

Furthermore, FeS_2 could also produce other sulfur species according to the following reaction:

$$FeS_2 \longrightarrow Fe^{3+} + 2\,S^i + 3\,e^- \tag{5.4}$$
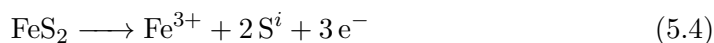
Here S^i depicts interfacial sulfur species which is presumably formed during the corrosion [30].

5.3.2 Cathodic Potential (Negative Potential)

One of the main electrochemical reaction during cathodic polarization of pyrite electrode is the reduction of S_2^{2-} ions (reaction 5.5) in the lattice before the H_2 evolution reaction ($E^0 = -0.76$ V (vs. NHE, pH 13) [32]. The CV in Figure 5.4 proves this reaction (S_2^{2-}-reduction region).

$$2\,e^- + S_2^{2-} \longrightarrow 2\,S^{2-} \qquad E^0 = -0.48\,V\,(vs.\ NHE) \tag{5.5}$$
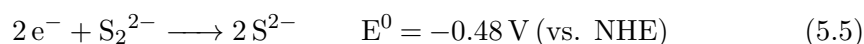
In addition, the reduction of interfacial sulfur species (S^i in the reaction 5.4) could occur at this point.

5.3.3 Dark Current versus Photocurrent

Even pyrite electrodes show a quasi-metallic behavior, a clear split between the dark current and photocurrent could be observed in both the natural pyrite electrode and the pyrite electrode prepared from the FeS$_2$-powder. Photoeffects are detected at higher current densities (see blue voltammograms (photocurrent) compared to the black ones (dark current) in Figure 4.14 and Figure 4.15). For a better com-
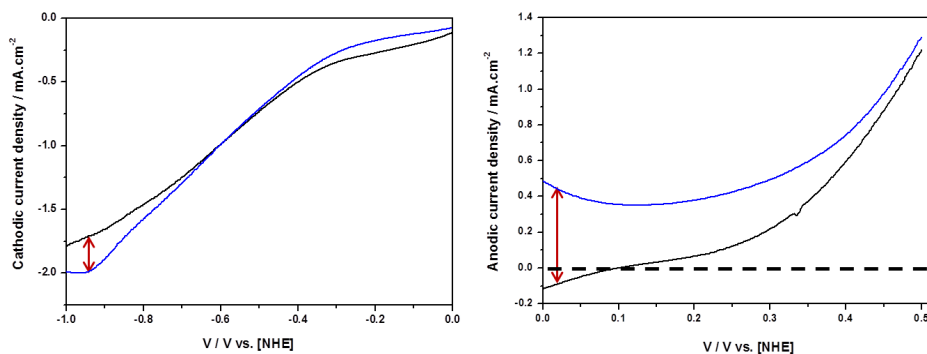
Figure 5.6: I-V curves of the natural pyrite electrode measured in 0.1 M NaOH. Left: cathodic current densities, Right: anodic current densities; The current densities (mA cm^{-2}) in the dark (black lines) and under illumination ($\lambda = 455$ nm, $18.7\,\mathrm{mW\,cm^{-2}}$, blue lines) are shown as a function of the applied potential V vs. NHE.

parison of the photoeffect, two anodic and cathodic currents of the natural pyrite electrode are presented in Figure 5.6. The cathodic photocurrent shows that the current density decreases to the lower photocurrent, while the anodic photocurrent verifies more response to the photoeffect (see labeled red vectors in Figure 5.6). In the anodic photocurrent a gap of $0.6\,\mathrm{mA\,cm^{-2}}$ between the dark current and the photocurrent could be observed.

Another important point during the photoelectrochemical measurements was the observation of photocorrosion. The photocorrosion was lower during measurements with lower illumination intensity.

5.3.4 Photocorrosion

The main side reaction at the positive potentials of the photocurrent is the photocorrosion. During the measurements, the formation of a dark-red film could be observed. The color of this film is probably caused by the formation of iron oxide at the pyrite surface.

Figure 5.7 presents a picture of the natural pyrite electrode after the photoelectrochemical measurements. The formation of Fe(III)-oxide at the electrode surface
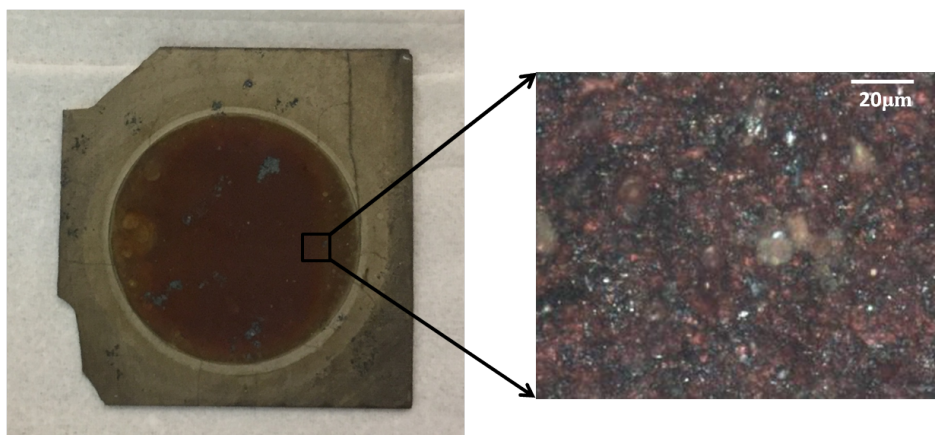
Figure 5.7: Natural pyrite electrode after the photoelectrochemical measurements; The left image presents a Raman microscope image of the selected area of this electrode.

has been investigated by means of Raman microscopy. Figure 5.8 presents two Raman spectra of the natural pyrite electrode. These spectra were taken from two different spots on the electrode. The black spectrum was taken from a gray spot that corresponds to pyrite structure [149, 150]. The red spectrum was taken from a dark red spot which could not be identified as pyrite structure. The bands in this spectrum are in a good agreement with reported bands of iron oxide hematite in the literature [148, 150].

After discussion all of the possible reactions in pyrite electrode (see section 5.3.1 and section 5.3.2), it is clear that electrochemistry or photoelectrochemistry on the pyrite using just water as the supporting electrolyte in not a good choice to investigate this material, because pyrite in the water and under illumination is unstable.
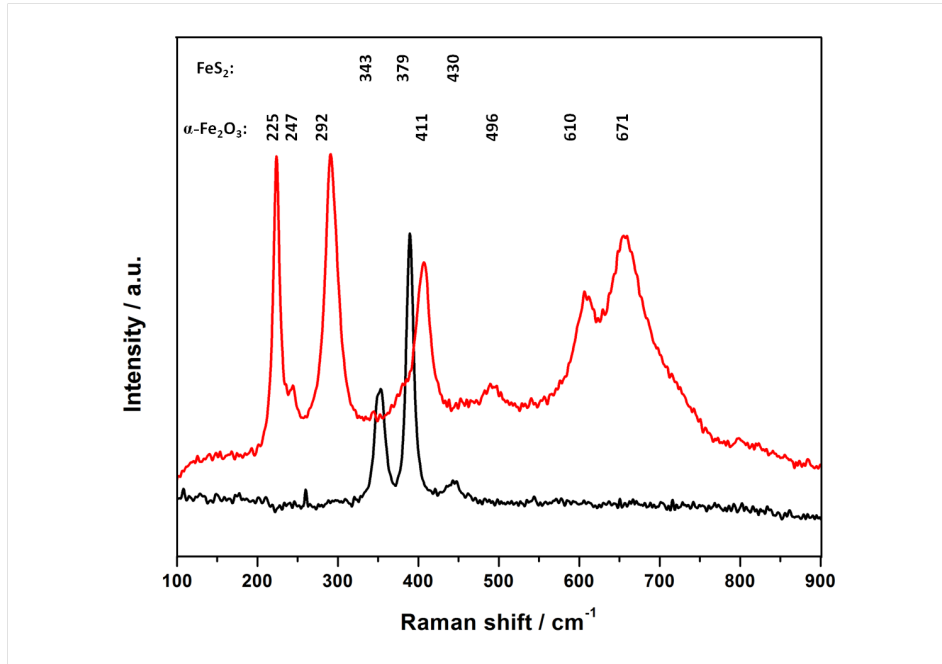
Figure 5.8: Raman spectra of the natural pyrite electrode. The black spectrum was taken from a gray part of the electrode, the red spectrum was taken from a dark-red part of the electrode. Labels α-Fe$_2$O$_3$ and FeS$_2$ indicate Raman frequencies (in cm^{-1}) of the typical Raman spectra of hematite and pyrite reported in the literature. (the values are taken from [148–150].)

5.3.5 Flat-band Potential of FeS$_2$

In all of the investigations on pyrite in the present study, pyrite shows the behavior of an n-type semiconductor. This could be assumed from the Mott-Schottky plots. Generally, when the space charge is populated with electrons, the slope will be negative. This means that the doping density is negative and the material is a p-type semiconductor. On the other hand, for an n-type semiconductor, the slope will be positive [151]. This is the case for the pyrite electrodes in the present study.

Pyrite is found as both an n- and p-type semiconductor in nature. However, the most investigation on pyrite found that n-type pyrite is more common [16, 31–33, 135, 152–154]. This variety could be caused by the sensitivity of thermoelectric probe measurement, the surface disturbance induced by polishing, or the presence of impurities in the samples [16].

As mentioned before, the natural pyrite electrode was corroded during the measurements. Therefore the pyrite electrode was prepared from FeS$_2$ powder. The

Doctor Blade method was applied to coat commercially available FeS_2 powder on the FTO glass (see section 3.1.7). These electrodes were employed to determine the flat-band potential of the pyrite by means of impedance spectroscopy. It should be noted that all of the impedance experiments were carried out in the dark with frequencies of 500 Hz and 100 Hz (the electrodes were corroded more quickly at a frequency of 1 kHz). The results, which are presented in the table 4.4 , indicate that the E_{FB} is in the range between -0.18±0.02 and -0.16±0.02 V vs. NHE (measured at pH=13). These values are much positive than $E^0_{H^+/H_2}$ (-0.76 V vs. NHE, pH 13).
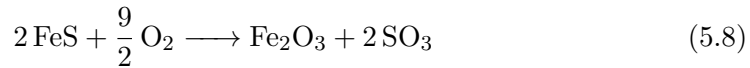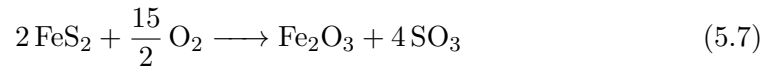
One key factor in the interpretation of these results is the preparation pathway of the pyrite electrode. As mentioned, the last step in the preparation pathway was the thermal treatment in the air. The thermal treatment of the iron sulfide at $400\,°C$ in air induces the formation of iron oxides (such as Fe_2O_3 and Fe_3O_4)[155].

Pelovski *et al.* investigated thermochemical decomposition of pyrite in the air. The authors could identify alpha and gamma modification of Fe_2O_3 beside FeS_2 in their analyses. They proposed that in a temperature range of 683-789 K (corresponding to 409-515 °C) FeS_2 decomposes according to the:

$$FeS_2 \longrightarrow FeS + S \tag{5.6}$$

Furthermore, FeS_2 and FeS will be oxidized according to the following reactions:

$$2\,FeS_2 + \frac{15}{2}\,O_2 \longrightarrow Fe_2O_3 + 4\,SO_3 \tag{5.7}$$

$$2\,FeS + \frac{9}{2}\,O_2 \longrightarrow Fe_2O_3 + 2\,SO_3 \tag{5.8}$$

Based on these reactions and the fact that the pyrite electrodes were thermally treated in the air, certainly, the electrodes exhibit impurities like Fe_2O_3. These impurities lead to the positive shift of the flat band potential.

The band gap of pyrite is reported by several groups to be 1±0.2 eV. In addition, the flat band potential, the conduction band edge potential (E_C), and the position of the energy bands of pyrite have been investigated by several groups. However, there is a wide disagreement in the E_C values (or E_{FB}, since E_{FB} is usually $0.3\,eV$ below than E_C in an n-type semiconductor). This could be based on the different applied methods, experimental conditions, or the electrode preparation technique. Wei *et al.* [154] also mentioned this difference in their work and try to compile some of the E_C values from the different investigations on pyrite. Figure 5.9 presents some

of the E_C values determined by various authors [154, 156–158].
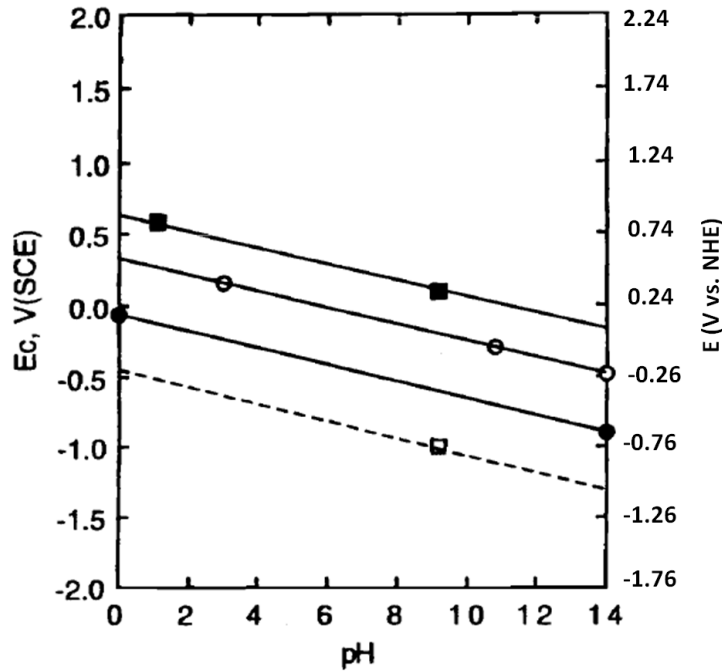
Figure 5.9: Some of the reported values for the conduction band edge (E_C) of pyrite by different authors, Adapted from [154]; ■Values are from [157],○Values are from [154], ●Values are from [156], □Values are from [158].

Furthermore, the donor densities (N_D) of pyrite electrodes have been determined (see Section 4.4.2). The donor density of pyrite is reported to be $0.76 \times 10^{19}\,\mathrm{cm}^{-3}$ [33]. The values obtained in the present study are in good agreement with the literature.

After the discussion of our investigations on pyrite electrodes, it could be assumed that the chemistry of FeS$_2$ in aqueous media and electrode preparation method have a huge factor and these lead to disagreement in the literature about the position of the conduction band edge.

5.4 Photocatalytic H$_2$ or O$_2$ Production

The two main photocatalysts in the present study are α-Fe$_2$O$_3$ and FeS$_2$. These two photocatysts have been employed for the photocatalytic O$_2$ and H$_2$ production, respectively. In almost all of these experiments the photocalyst was loaded with a co-catalyst. The first four sections of this chapter deal with the role and effect of the

co-catalysts in the photocatalytic reactions. In addition, the role of the sacrificial reagent for each individual process (H$_2$ or O$_2$ evolution) will be discussed.

5.4.1 Role of the Co-catalysts

In the present study, the production of hydrogen gas from the reduction of the H$_2$O, and the production of oxygen gas from the oxidation of the H$_2$O was studied. For this purpose, the co-catalyst (Co-Cat) loaded Fe$_2$O$_3$ (or FeS$_2$) has been employed under visible illumination. Platinum (Pt), Gold (Au), Cobalt (Co), Copper (Cu), Iridium (Ir), Chromium (Cr), Ruthenium (Ru), and Nickel (Ni) were loaded as pure metal or as metal oxide on commercially available Fe$_2$O$_3$-powders (or FeS$_2$-powders) as co-catalysts. (See section 3.1.5)

The role of the co-catalysts has been described in detail in section 2.6.1. The co-catalysts could function as active sites for reduction reactions (or oxidation reactions) and/or suppress the reverse reaction of water formation. The role of the co-catalysts could also be explained with a comparison between reduction and oxidation reactions, which take place in a photoelectrochemical cell. In photoelectrochemistry, the interfacial electron transfers during a reduction or oxidation reaction are separated due to the fact that they proceed at the semiconductor and counter electrode, both dipping into the redox electrolyte. For example, at a photoanode, the reactive holes oxidize the redox electrolyte, while photogenerated electrons migrate through an external wire to the counter electrode, where they reduce the redox electrolyte. In the case of a photocatalyst, the electron transfer during reduction and oxidation reactions occurs at the surface of the photocatalyst. It is generally assumed that the photogenerated electrons are first trapped at reactive surface sites, before undergoing interfacial electron transfers. Therefore, loading the photocatalysts with metals could be like introducing a surface "counter electrode" to the particle and it might improve the efficiency of reactive charge generation (see Figure 5.10) [96, 103, 159].

Generally, the role of the co-catalysts in both water oxidation and reduction is important and depends on their interaction with the semiconductor through the interface/junction. An efficient water oxidation co-catalyst should be capable of quick transfer of holes to H$_2$O, while a good water reduction co-catalyst should be capable of quick transfer of electrons for reduction of H$^+$. This is only possible when the energy levels and electronic structure of the co-catalyst and the photocatalyst are in harmony. This means the electronic structures (Fermi levels or band levels) of both materials at the interface should be able to drive the charge transport process
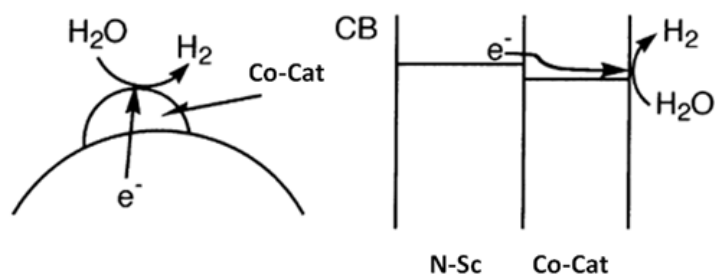
Figure 5.10: Schematic illustration of the electron transfer through the co-catalyst (Co-Cat) at the surface of the photocatalyst in the example of an N-type semiconductor (N-Sc).

in the right direction [160].

In the present work three aspects of the role of the co-catalyst loading have been investigated: first, the optimum loading amount, followed by the best co-cat for either the water oxidation or reduction reaction.

5.4.2 Optimum Co-Cat Loading percent

RuO_2 and IrO_2 have already been shown to be good O_2 evolution co-catalysts [59, 65, 161, 162]. On the other hand, Pt is one of the most investigated and common H_2 evolution Co-Cat [163, 164].

The α-Fe_2O_3 powders have been modified with different wt.% of RuO_2 to find the optimum loading percent for the O_2 evolution reaction (see section 4.5.2). Figure 4.18 presents the results of these investigations. The oxygen production rate increased clearly when the loading percent of RuO_2 was increased to 0.5%. The optimum loading of this particular co-catalyst for this reaction is 0.5 wt.%. The oxygen evolution rate decreased with further increase in RuO_2 loading (e.g. to 1 wt.%).

Generally, these results show that RuO_2 loading has a positive influence on the O_2 evolution reaction. However, the optimum loading percent of the RuO_2 should be considered. At a very high loading percent, RuO_2 could react as a recombination center for the photogenerated electron and holes, and this reduces the photocatalytic activity [165, 166]. Based on these results 0.5 wt.% was chosen as the loading percent for further investigations.

The optimum wt% for the Co-Cat loading on FeS_2 has been investigated on modified FeS_2 nanoparticles (see section 4.5.5). The results of these investigations

have been presented in the Figure 4.20. The interesting point of these results is that the 0.5 wt% loading shows the highest H$_2$ production rate. 1% loading leads to the decreased H$_2$ evolution rate. From these results, it could be assumed that an excess amount of Pt (beyond the optimum loading of 0.5 wt.%) increases the probability of a recombination reaction and this leads to a decrease in the photocatalytic activity.

The appearance of a maximum in activity with an optimum loading of co-catalyst has been reported by several authors [102, 165, 167]. The interesting point is that 0.5 wt. % of the loading shows the best results not only in the present study, but also in many other investigations. Several authors reported an optimum loading percent of 0.5 for TiO$_2$ photocatalyst [164, 168, 169]. Puangpetch *et al.* reported an optimum Pt loading of 0.5 wt.% for SrTiO$_3$ [170]. In ZnO photocatalyst 0.5 wt. % of α-Fe$_2$O$_3$ is also shown to be an optimum loading percent [171].

Further reasons for the decrease in activity above the optimum loading percent have also been explained. Too much Co-Cat loading could reduce photon absorption by the photocatalyst, and as mentioned lead to the production of electron-hole recombination centers. Another reason could probably be that the Co-Cat might act as a catalyst, and catalyzes the backward reaction of hydrogen and oxygen [48, 164].

5.4.3 Effect of Co-Cat Loading on O$_2$ Evolution Reaction

In the present study, the production of O$_2$ with metal loaded Fe$_2$O$_3$ under visible light irradiation was investigated . Therefore Co-Cat/Fe$_2$O$_3$-powders were employed for the production of O$_2$ through oxidation of water. Thereby Fe^{3+} were used as electron acceptors (sacrificial agents). The results are presented in section 4.5.3. Figure 5.11 depicts an illustration of O$_2$ production with co-catalyst loaded Fe$_2$O$_3$ in the presence of Fe^{3+}.

The results in the table 4.5 indicate that the O$_2$ production rate is clearly higher with all Co-Cat loaded Fe$_2$O$_3$ than the bare Fe$_2$O$_3$ expect for IrO$_2$ and Cr$_2$O$_3$ (NiO/Fe$_2$O$_3$ exhibit nearly the same activity as bare Fe$_2$O$_3$).

All three metal oxides RuO$_2$, CuO, and CoO show more or less the same effect on the O$_2$ evolution rate. This might be due to the fact that transition-metal oxides in contact with the semiconductor form a Schottky barrier, and this leads to effective trapping of the holes, resulting in efficient charge separation and improved photocatalytic activity (see Figure 2.12). Pt and Au loading also improves the photocatalytic activity of Fe$_2$O$_3$, but less than RuO$_2$, CuO, and CoO. This might be due to the different loading methods. These two noble metals were loaded by the
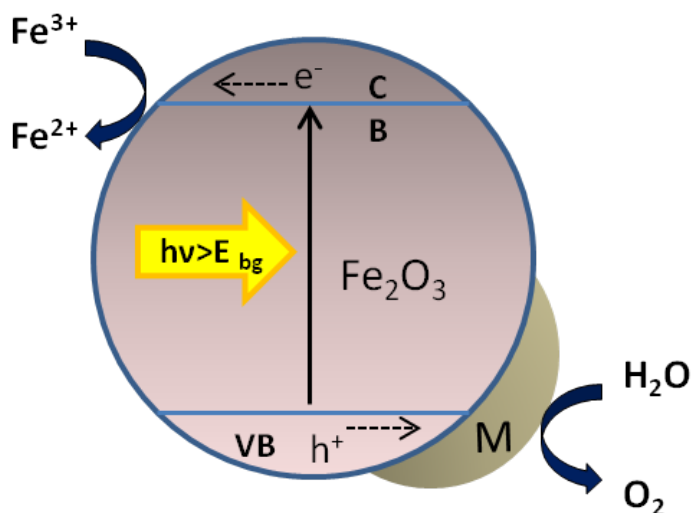
Figure 5.11: Schematic illustration of the water oxidation with co-catalyst (M) loaded Fe_2O_3 photocatalyst

in situ photodepostion and all of the metal oxides with the impregnation method. There are some discussions in the literature about the effect of different loading methods [48, 51]. This variation might affect the contact between the co-catalyst and the semiconductor and the creation of the active sites for the photocatalytic reactions. Moreover, Au and Pt are known as good electron acceptor catalysts, this could be a further reason that the O_2 evolution rates in case of Pt/Fe_2O_3 and Au/Fe_2O_3 were less than RuO_2/Fe_2O_3, CuO/Fe_2O_3 and CoO/Fe_2O_3.

NiO/Fe_2O_3 and IrO_2/Fe_2O_3 exhibit less activity than the bare Fe_2O_3. The interesting point is that NiO/FeS_2 shows the highest activity for H_2 production (see table 4.6). Therefore, it could be expected that NiO/Fe_2O_3 reveals less activity for O_2 production. On the other hand, IrO_2 is one of the more often employed materials for photoelectrochemical oxygen evolution reactions, while a negative effect on photocatalytic O_2 evolution reaction is shown here. However, the reported photoelectrodes for O_2 evolution are usually prepared in different ways. The photoelectrodes are usually prepared under high thermal treatment to improve the stability of iridium oxide [20, 172]. In contrats, in the present study iridium species (from $IrCl_3$) were simply impregnated on the iron oxide surface.

In addition, these metal oxides might influence the electronic structure of Fe_2O_3 and could lower the quasi-fermi level, which raises the recombination of electron-hole pairs and thus suppresses the O_2 evolution. In this case, the recombination

process becomes competitive or even dominant process against the water oxidation process (Figure 5.12 b). Generally, the quasi-Fermi level described the electrochemical potential of one carrier type at a time (i.e., either electrons or holes) under nonequilibrium (e.g., illuminated) conditions. Changes in ΔE_F effect recombination of the charge carriers (see Figure 5.12 a).
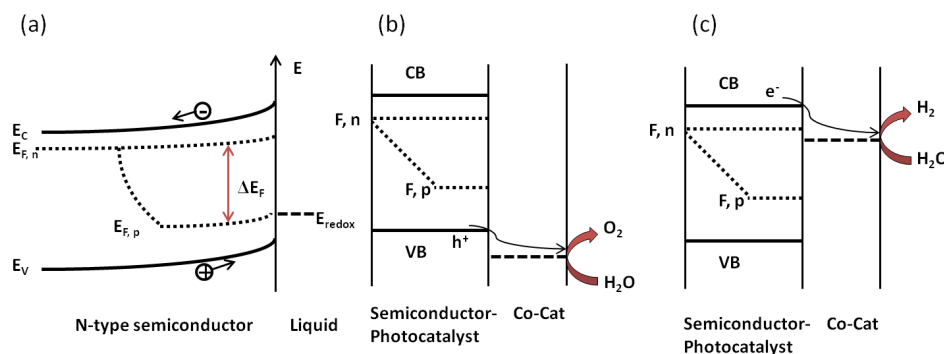
Figure 5.12: a) Energy band model for an n-type semiconductor/liquid contact in terms of differences in the quasi-Fermi levels ($E_{F,n}$ is the electron quasi-Fermi level and $E_{F,p}$ is the hole quasi-Fermi level.), b) competition between recombination of electron-hole pairs through changes in ΔE_F and water oxidation process or c) water reduction process.

Aside from the photocatalytic test, RuO_2/Fe_2O_3 has been characterized. For this purpose, Raman spectroscopy was applied. Raman spectra of both bare Fe_2O_3 and RuO_2/Fe_2O_3 were taken to determine the changes in the surface properties. However, the spectrum of RuO_2/Fe_2O_3 shows no changes in the Raman shift. This could be due to the low loading percent (0.5). All of the bands in the spectrum are the same as the bands of the bare Fe_2O_3. The comparison of these spectra is presented in appendix 6.

5.4.4 Effect of the Co-Cat Loading on the H_2 Evolution Reaction

In the present study, the role of different co-catalysts on the H_2 production has been investigated. Hence, Co-Cat/FeS_2-powders were used as the photocatalyst and sulfide and sulfite as sacrificial electron donors. The results are presented in section 4.5.6. Figure 5.13 shows an illustration of H_2 production for FeS_2 with and without a co-catalyst. The results in table 4.6 demonstrated that the yields of H_2 production are rather high for NiO/FeS_2 and Au/FeS_2. In these cases, the deposited Co-Cat could act as an electron sink, which prevents the recombination of

Figure 5.13: Schematic illustration of photocatalytic H_2 formation in the presence of electron donor employing (a) bare FeS_2 and (b) with co-catalyst (M) loaded FeS_2. A co-catalyst could reduces the recombination of the photogenerated electrons and holes and provides active sites for proton reduction.

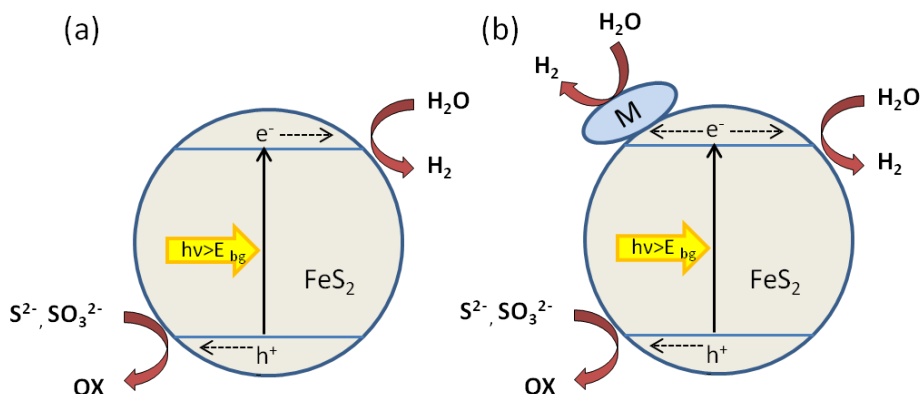electron-hole pairs. Moreover, NiO, Au, and Pt are well known as good co-catalysts for H_2 production [51]. NiO and Au show high activity here, but this is not the case for Pt. However, it should be noted that the H_2 formation proceeds with relatively high efficiency even in the absence of any co-catalyst (see FeS_2 data in table 4.6). In this case, it can be assumed that Fe (II) gropes reduce to Fe(0), and this Fe (0) collected conduction band electrons, similar to Co-Cat deposits on the FeS_2 surface. This mechanism is also described in the literature for Ni (0)/NiO [173].

In the other cases (Cr_2O_3, CuO, CoO, IrO_2, Pt, RuO_2), the metal adsorption on FeS_2 might have affected its electronic structure and could lower the quasi-fermi level, which enhances the recombination of electron-hole pairs and thereby suppresses the proton reduction evolving H_2. The recombination process becomes the competitive or even dominant process compared to the proton reduction process (Figure 5.12 c). The last point in this context is that RuO_2 and IrO_2 are well known as good co-catalysts for O_2 production reactions [5, 51, 65], and it is not a surprise that they show less activity here for H_2 production.

Further investigations on the NiO/FeS_2 system have been carried out. Raman and EDXS were used to determine the changes in the surface properties or chemical compositions of the sample. The Raman spectrum of NiO/FeS_2 shows no changes in the Raman shift. Here could be also due to the low loading percent of the co-catalyst (0.5). All of the bands in the spectrum are the same as the bands of the bare FeS_2 sample. The comparison of these spectra is presented in appendix 7.

However, by means of the EDXS, the existence of NiO in the samples is proved. The EDXS analyses show 0.48 wt. % of NiO in the sample, which is in good agreement with the applied loading percent (0.5). The results are presented in appendix 7.

5.4.5 Oxygen Production in Presence of Fe^{3+}/Fe^{2+}

The photocatalytic O$_2$ evolution on α-Fe$_2$O$_3$ (or Co-Cat/α-Fe$_2$O$_3$) proceeded in the presence of Fe^{3+}. Iron(III) ions are very effective electron acceptors and already used for O$_2$ evolution with WO$_3$ and TiO$_2$ particles [108, 110]. Even though AgNO$_3$ is one of the most frequently applied sacrificial reagents for the water oxidation [5, 97], Fe^{3+} was the better choice in the present study. Fe(III) ions can react with photogenerated electrons and produce Fe(II) ions so that a reversible redox couple (Fe^{3+}/Fe^{2+}, $E^0 = 0.77$ V vs. SHE) is presented in the solution. This is beneficial compared to Ag$^+$, which can reduce to Ag simply by being deposited on the photocatalyst surface [11, 108].

In addition, some blank experiments were also performed. In the blank experiments, the ferric solution without the photocatalyst was irradiated and no O$_2$ could be detected.

The concentration changes of Fe^{3+} and Fe^{2+} before and after the photocatalytic reactions were determined. The results are presented in section 4.7.1 . These investigations indicate that the amount of consumed Fe^{3+} is higher than the amount of produced Fe^{2+}. It is also notable that the consumption and production are not within the stoichiometric ratio in comparison to the amount of produced O$_2$. Different parameters should be considered to explain this behavior. Here first this behavior will be interpreted and the mechanism of photocatalytic water oxidation in presence of iron ions will be subsequently discussed.

Figure 4.17 reveals that the O$_2$ evolution was rather high in the first 3 hours of the irradiation, but this drastically changed and became very low in the remaining time. One reason for this could be the adsorption of oxygen by the photocatalyst or the loss of oxygen into the gas phase above the solution [108]. Oxygen can also dissolve in water and is therefore not detectable (solubility of O$_2$=1.28 mmol L^{-1} [174]). It is also possible that in acidic media O$_2$ reacts with electrons and H$^+$ to produce H$_2$O$_2$ according to the following reaction [147]:

$$O_2 + 2\,H^+ + 2\,e^- \longrightarrow H_2O_2 \qquad E^0 = 0.28\,V(NHE), pH\,7 \qquad (5.9)$$
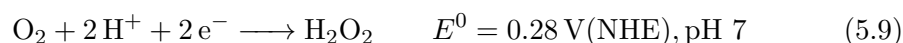
H_2O_2 could also be reduced to H_2O:

$$H_2O_2 + 2\,H^+ + 2\,e^- \longrightarrow 2\,H_2O \qquad E^0 = 1.35\,V(NHE), pH\,7 \qquad (5.10)$$
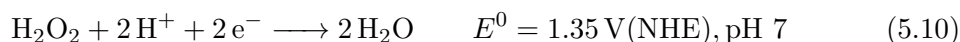
Another reason which impairs the O_2 evolution procedure is the $Fe(NO_3)_3$ solution. The UV-vis spectra of aqueous $Fe(NO_3)_3$ indicate that this solution absorbs the light with $\lambda < 550$ nm (the molar absorption coefficient (ε) of the Fe^{3+} ion was calculated to be 0.02 cm^2 mol^{-1}) (Figure 5.14). The light absorption of Fe^{3+} in this region affects the oxygen production because hematite also absorbs the light in this region.
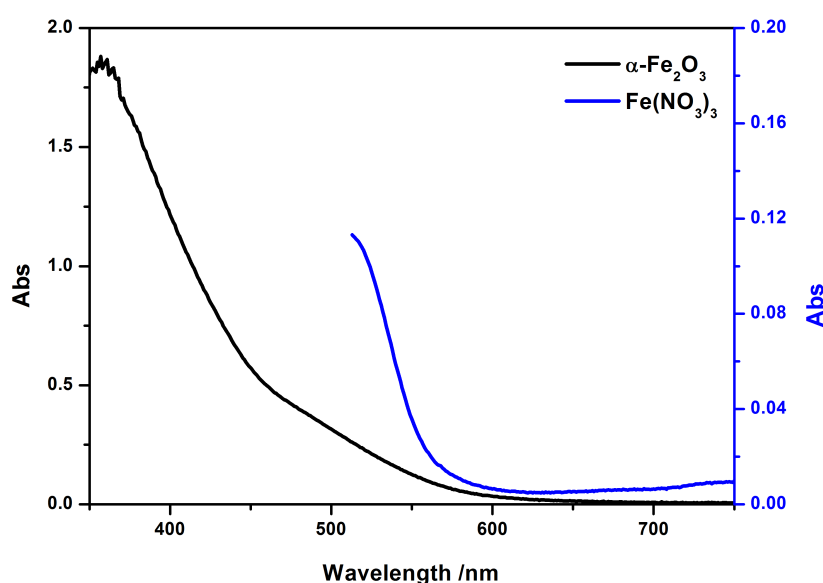
Figure 5.14: A comparison between the UV-Vis spectra of the transparent colloidal α-Fe$_2$O$_3$ nanoparticles and an aqueous solution of $Fe(NO_3)_3$ (2 mM)

The effect of Fe^{3+} ions-absorption on oxygen formation is also discussed by Darwent and Mills in 1981 [108]. These authors studied the photocatalytic O_2 formation using WO_3 as the photocatalyst in the presence of Fe^{3+} ions (0.01 M FeCl$_3$). They observed that oxygen was only produced in the wavelength range $\lambda < 500$ nm, because WO_3 has a band gap of 2.6 eV (corresponding to λ=480 nm). The maximum O_2 production occurred around 410 nm and below this value the O_2 production decreased. They attribute this behavior to the absorption of Fe^{3+} ions between 320-500 nm (see Figure 5.15).
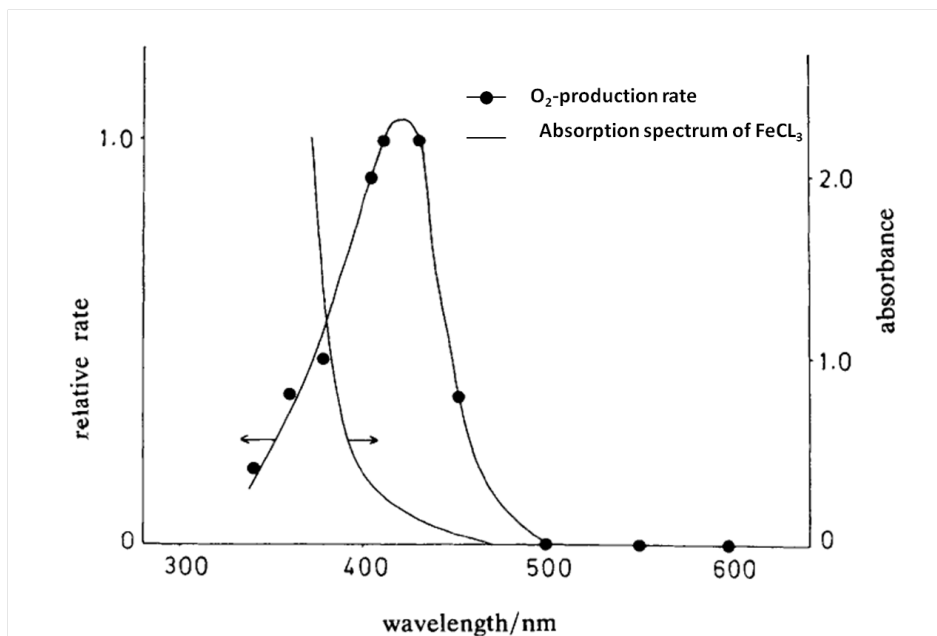
Figure 5.15: Comparison between photocatalytic O_2 production, applied WO_3 powder as the photocatalyst ($6.5\,\mathrm{mg\,L^{-1}}$ of WO_3 in 0.01 M $FeCl_3$ 0.05 M H_2SO_4), and the absorption spectrum of $FeCl_3$ (0.01 M $FeCl_3$ in 0.05 M H_2SO_4), adapted from [108].

Figure 5.16 depicts the position of the conduction and the valence band of hematite in contact with water at pH 7 (CB and VB positions determined by considering the measured E_{FB}- and the E_g- values of hematite in this thesis). The position of the conduction band of Fe_2O_3 is much higher than the reduction potential of Fe^{3+} to Fe^{2+} ($E^0_{Fe^{3+}/Fe^{2+}} \sim 0.36$ V (NHE) at pH 7) and slightly lower than the hydrogen production potential. Indeed in some of the experiments traces of H_2 gas could be detected but they were not high. In addition, Figure 5.16 illustrates the reduction potentials of one-electron couples in water at pH 7.

The proposed mechanism for O_2 production in the presence of Fe^{3+} is summarized here:

$$Fe_2O_3 + h\nu \xrightarrow{E \geq E_{bg}} e^- + h^+ \tag{5.11}$$

$$e^- + h^+ \longrightarrow \text{recombination} \longrightarrow \text{heat} \tag{5.12}$$

$$4\,h^+ + 2\,H_2O \longrightarrow 4\,H^+ + O_2 \tag{5.13}$$

$$e^- + Fe^{3+} \longrightarrow Fe^{2+} \tag{5.14}$$
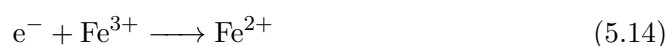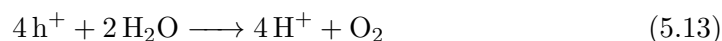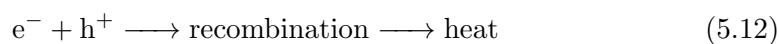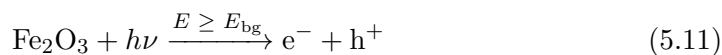
Figure 5.16: Schematic diagram of the energy levels between the semiconductor Fe_2O_3 and several redox couples in water at pH 7 (the values of one-electron couples are taken from [82].

One reason for the low photonic efficiency of the O_2 evolution over Fe_2O_3 is the recombination of the electron-hole pairs (reaction 5.12). It is also possible for several side reactions to occur so that an efficient photocatalytic reaction will be prevented. These side reactions are:

- reverse reaction of holes with Fe^{2+}:

$$Fe^{2+} + h^+ \longrightarrow Fe^{3+} \tag{5.15}$$
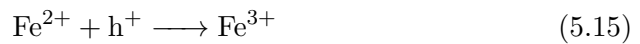
- produced O_2 (reaction 5.13) reduced to H_2O_2 according to reaction 5.9 or could still be adsorbed at surface and produce $O_2^{\bullet-}$ [110]:

$$O_{2(ads)} + e^- \longrightarrow O_{2(ads)}^{\bullet-} \tag{5.16}$$

$$O_{2(ads)}^{\bullet-} + e^- + 2\,H^+ \longrightarrow H_2O_2 \tag{5.17}$$

5.4.6 Hydrogen Production in Presence of S^{2-}/SO_3^{2-}

In the present study pyrite electrodes in the electrochemical cell have been studied and the anodic dissolution of pyrite electrodes has been observed (see section 5.3). It

is assumed that pyrite in an electrochemical cell reacts with water to produce Fe^{3+}, $SO_4{}^{2-}$, H^+ and electrons according to the reaction 4.6. In addition, it is known that during illumination and in the absence of electron donors the material photo-corrodes by holes according to reaction 2.5 [135, 175]. However, the possibility of stabilization of FeS_2 in the aqueous solution containing electron donor species such as I^- ($E^0_{I_2/I^-} = 0.54$ V (SHE)), Br^- ($E^0_{Br_2/Br^-} = 1.09$ V (SHE)) or Fe^{2+} ($E^0_{Fe^{3+}/Fe^{2+}} = 0.54$ V (SHE)) has been reported [30, 176].

Here the photocatalytic H_2 production with pyrite (or Co-Cat/pyrite) was investigated in the presence of S^{2-} and $SO_3{}^{2-}$ as sacrificial reagents. These species prevent FeS_2 from photocorrosion by acting as hole scavengers and also promote hydrogen evolution through making up half of the water splitting reaction. The reaction mechanism for the photocatalytic hydrogen production over FeS_2 in the presence of S^{2-} and $SO_3{}^{2-}$ is similar to the reported mechanisms of CdS photocatalysts (described in section 2.6.5) [103, 113, 177].

The hydrolysis of S^{2-} and $SO_3{}^{2-}$ ions leads to the formation of a basic media for the reaction. S^{2-} hydrolyses as follow:

$$S^{2-} + H_2O \longrightarrow HS^- + OH^- \tag{5.18}$$

$$HS^- + H_2O \longrightarrow H_2S + OH^- \tag{5.19}$$

and $SO_3{}^{2-}$ hydrolyses as follow:

$$SO_3{}^{2-} + H_2O \longrightarrow HSO_3{}^- + OH^- \tag{5.20}$$

$$HSO_3{}^- + H_2O \longrightarrow H_2SO_3 + OH^- \tag{5.21}$$
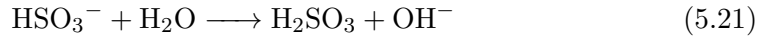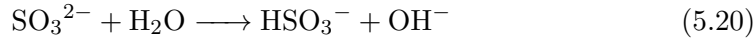
Under the basic conditions the flat band potential of FeS_2 ($\sim$ -0.60 V NHE, pH 7) and the redox potential of H^+/H_2 will be negatively shifted.

In water at pH 7, the position of the valence band of FeS_2 is $\sim$ +0.4 V (NHE) [39] which is quite below the standard redox potentials of possible oxidation reactions in this work (blue dashed line in Figure 5.17). Figure 5.17 illustrates the energy level of the valence band (VB) and conduction band (CB) of FeS_2 and their relationship to the oxidation level of reducing agents in this work. The positions of CB and VB were taken from the reported values in the literature [27, 30, 33, 39], since in this work, natural pyrite electrodes were affected by corrosion and the thermal treatment in air on further pyrite electrodes lead to the positive shift of E_{FB} (more detail in section 5.3.5). This diagram indicates that two-electron transfer processes
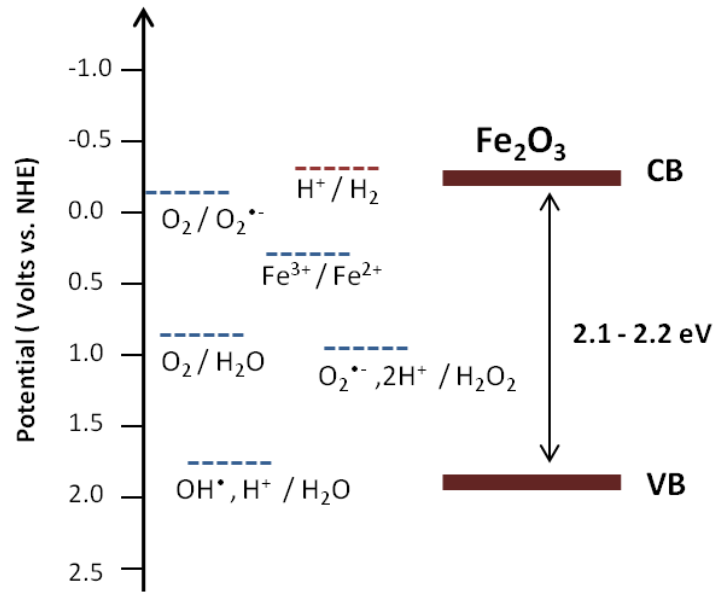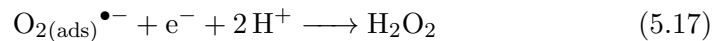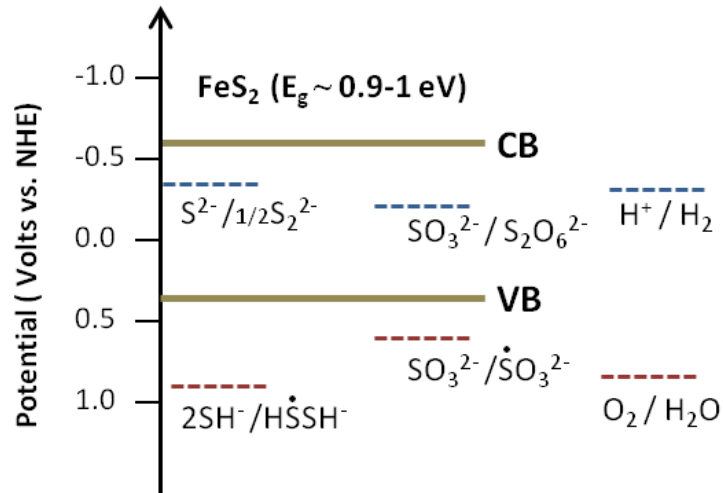
Figure 5.17: Schematic diagram of the energy levels between the semiconductor FeS$_2$ and reducing agents in the water at pH 7 (the values of one-electron couples are taken from [82]).

(oxidation of S^{2-} and SO$_3$$^{2-}$ to the S$_2$$^{2-}$ and S$_2$O$_6$$^{2-}$ / blue dashed lines) are thermodynamically more favorable than the one-electron transfer (oxidation of S^{2-} and SO$_3$$^{2-}$ to the S$^{-\bullet}$ and $^{\bullet}$SO$_3$$^{-}$ / red dashed lines).

The proposed mechanism and all intermediates are summarized here:

- Generation of charge carriers (irradiation with $E \geq E_{bg}$ of FeS$_2$):

$$\text{FeS}_2 + h\nu \longrightarrow \text{e}^-_{\text{CB}} + \text{h}^+_{\text{VB}} \tag{5.22}$$

- Recombination of charge carriers:

$$\text{FeS}_2(\text{e}^-_{\text{CB}} + \text{h}^+_{\text{VB}}) \longrightarrow \text{FeS}_2 \tag{5.23}$$

- Trapping of charge carriers for H$_2$ formation:

$$2\,\text{H}_2\text{O} + 2\,\text{e}^-_{\text{CB}} \longrightarrow \text{H}_2 + 2\,\text{OH}^- \tag{5.24}$$

- Due to the fact that the concentration of S^{2-} is higher than SO$_3$$^{2-}$ (and assuming that the reaction rate constant is equal for both oxidation reactions), we suppose that the photogenerated holes in the valence band oxidize S^{2-} to
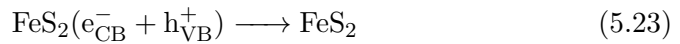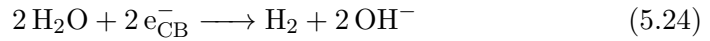
$S_2{}^{2-}$:

$$2\,S^{2-} + 2\,h_{VB}^{+} \longrightarrow S_2{}^{2-} \tag{5.25}$$

- $S_2{}^{2-}$ reacts with $SO_3{}^{2-}$ to produce thiosulfate (this can efficiently suppress the formation of disulfide ($S_2{}^{2-}$) ions and support the hydrogen production):

$$S_2{}^{2-} + SO_3{}^{2-} \longrightarrow S_2O_3{}^{2-} + S^{2-} \tag{2.18}$$
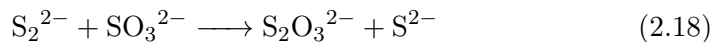
This sulfur species could be further oxidized to sulfate by reaction with hydroxyl groups in the water. Sulfate could also be produced by the oxidation of $SO_3{}^{2-}$ ions according to the following reaction[177]:

$$SO_3{}^{2-} + 2\,h^{+} + 2\,OH^{-} \longrightarrow SO_4{}^{2-} + H_2O \tag{2.14}$$

The co-catalysts also play an important role in the oxidation reaction. They could provide reactive surface sites and support thereby the two-electron transfer processes for the oxidation of S^{2-}.

The concentration changes of S^{2-}, $S_2O_3{}^{2-}$, $SO_4{}^{2-}$, and $S_2O_3{}^{2-}$ were determined and reported in section 4.7.2. These detected products are in good agreement with the proposed mechanism. The obtained results indicate that more sacrificial reagents have been consumed than the produced products (see Figure 4.25). This could be due to the fact that other products were produced which were not detectable by the measurement method chosen in the present work, for example the production of some interfacial sulfur species or the production of elemental sulfur [103, 177].

The second important conclusion from the results shown in section 4.7.2 is that the concentrations of the products are approx. 5 times higher than the concentration of the produced H_2. Based on the proposed mechanism for the H_2 production reaction (reaction 5.24) $2e^{-}$ are needed. If we assume that h^{+} just reacts with $S_2{}^{-}$ species (reaction 5.25), this gives a 1:1 equivalency. But the results show a different ratio; 1 (for H_2) to 5 (for oxidation products). Therefore it should be considered that holes also react with other species like $SO_3{}^{2-}$ (reaction 2.14) or interfacial sulfur species. Furthermore, electrons could be involved in the reduction of Fe^{3+} to Fe^{2+} (reaction 5.3). As mentioned in section 4.7.2, Fe^{3+} and $SO_4{}^{2-}$ are formed in the solution according to the reaction 4.6. These Fe^{3+} ions could react with the electrons and this lead to less production of H_2 ($E^0_{Fe^{3+}/Fe^{2+}} \sim 0.36\,V$ (NHE) at pH 7).

5.5 Photocatalytic Water Splitting

The overall water splitting was probed on Pt/TiO_2 (single photocatalyst water splitting system) and on the combination of $Co-Cat/Fe_2O_3$ and $Co-Cat/FeS_2$ (Z-scheme overall water splitting system). In this section the results of these experiments will be interpreted and discussed.

5.5.1 Single Photocatalyst Water Splitting System (Pt/TiO$_2$)

Titanium dioxide is the most commonly used photocatalyst for PC and PEC water splitting systems [5, 48, 53, 81]. In the present study Pt/TiO_2 (0.5 wt % Pt) has been prepared and applied to investigate the overall water splitting in pure water. The results are presented in section 4.6.1. As mentioned there, the ratio of the H_2/O_2 production does not confirm the stoichiometric ratio of H_2- and O_2-evolution during the photocatalytic overall water splitting. In fact, the determined O_2 evolution rate was very low (0.14 $\mu mol\,h^{-1}$).

There are many investigations on TiO_2 photocatalysts for water splitting. However, most of these reports present just the results of the H_2 evolution reaction. Either they use sacrificial reagents such as methanol or just in pure water [56, 98–100, 132].

Kandiel *et al.* [167] have investigated platinized TiO_2 photocatalyst powders employing the same experimental equipment, which has been used in the present work. They could not find any evidence for direct water splitting even in the presence of very low methanol concentrations and no O_2 gas was detected.

An interesting effect of carbonate salt addition on the water spilling over Pt-loaded TiO_2 has been reported by Sayama *et al.* [178]. They have observed H_2 and O_2 production only in the presence of carbonate salts. They explained two reasons for their observations. First, the backward reaction of H_2 and O_2 (to form H_2O) was suppressed distinctly on Pt in the presence of carbonate ions. The second reason was the changes in the surface of TiO_2 in the presence of carbonate ions. The surface of titanium dioxide was covered with several types of carbonate species, thus these carbonate species support desorption of O_2 from the TiO_2 surface.

The work of Yoshida *et al.* [179] belongs to few reports about the overall water splitting over Pt-loaded TiO_2. They study the effect of the oxidation state of Pt species and Pt-loading on the photocatalytic activity of TiO_2. The authors assumed that calcination temperature plays an important role and that different treatment at temperatures leads to different oxidation states of Pt. Indeed, in the present

study, the same method for the preparation of Pt loaded TiO_2 has been used, and simultaneous production of H_2 (8.33 $\mu mol\,h^{-1}$) and O_2 (0.14 $\mu mol\,h^{-1}$) could be observed.

In the literature it is mentioned quite often that the adsorption of the initially produced O_2 at the surface of TiO_2 is the main reason for less O_2 gas detection (or in some cases, entirely no O_2 gas detection) in this reaction. The initial O_2 will be formed in water according to reaction 5.13. This O_2 rapidly reacts with electrons and is adsorbed at the surface of TiO_2 [81, 164, 180, 181]:

$$O_2 + e^-_{CB} \xrightarrow[\text{Surface state}]{TiO_2} O_2^- \tag{5.26}$$
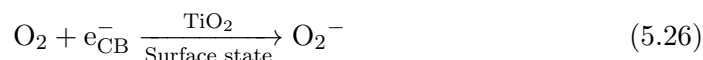
5.5.2 Z-Scheme Overall Water Splitting

Besides titanium dioxide, other materials are also employed for photocatalytic overall water splitting. Several tantalate photocatalysts are reported to be able to split water to H_2 and O_2 [5, 83, 84, 182]. However, the large band gap of these materials makes it impossible to effectively utilize solar energy. Therefore the Z-scheme systems (two-photon process) are good strategy to split water under visible light irradiation.

The present study shows that Fe_2O_3 and FeS_2 have the ideal band gap to absorb the visible light. Moreover, the band structure of Fe_2O_3 is appropriate for the oxidation of water and the band structure of FeS_2 is suitable for the reduction of water. In section 4.5.3 and section 4.5.6 it is shown that Co-Cat/Fe_2O_3 and Co-Cat/FeS_2 in the presence of suitable sacrificial reagents could produce O_2 and H_2, respectively. In addition, it has been demonstrated that RuO_2/Fe_2O_3 and NiO/FeS_2 exhibit the highest photocatalytic activity compared to other Co-Cat/photocatalyst combinations.

Generally, a Z-scheme system is a combination of one H_2- photocatalyst, one O_2-photocatalyst, and an electron mediator. However, the affinity between the photocatalysts and the electron mediator could inhibit the activity and make this system complicated. In addition, the electron mediators could promote the backward reactions of the intermediates or undesired water production from H_2 and O_2. The light absorption could also be affected by the electron mediators. Based on these reasons, the first experiments in this system were performed in the absence of an electron mediator.

The first combination was NiO/FeS_2 and RuO_2/Fe_2O_3 in pure water (see table 4.7). The combination of two semiconductors is already shown to be an effec-
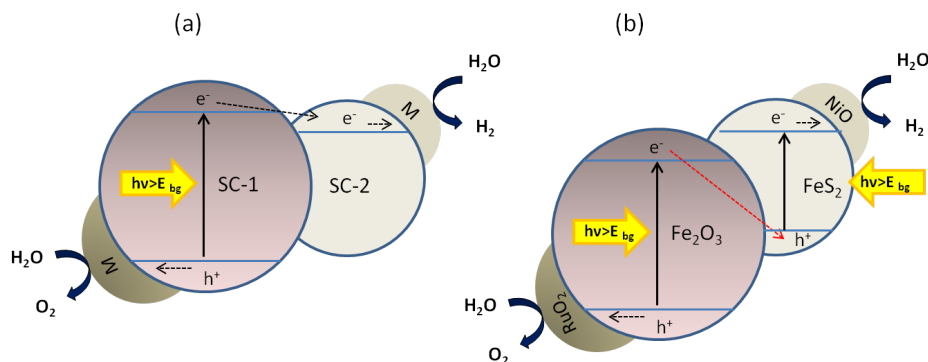
Figure 5.18: Illustration of the electron transfer in combination with two photocatalysts: a) How to perform an efficient heterojunction structure between two semiconductor photocatalysts (SC-1/SC-2), b) How is the heterojunction structure between NiO/FeS_2 and RuO_2/Fe_2O_3, in this case, there is no electron transfer from the CB of Fe_2O_3 to CB of FeS_2 feasible.

tive approach to improve the photocatalytic activity [51]. Since the combination of two semiconductors forms a heterojunction structure, this should lead to a better separation of the photogenerated charge carriers.

Figure 5.18 (a) presents the combination of two semiconductors in a heterojunction structure. In this figure, it has been assumed that SC-1 absorbs light to produce photogenerated electron-hole pairs. Holes oxidize water to oxygen while electrons will be transferred to SC-2 to produce H_2. This assumption is the best way to have an efficient heterojunction structure between two semiconductors. However, this heterojunction structure is not possible for NiO/FeS_2 and RuO_2/Fe_2O_3, because the band structure of these two semiconductors does not allow this combination. For the better interpretation, the band gaps and band alignments of hematite and pyrite are presented in Figure 5.19. Figure 5.19 reveals that the conduction band edge level of Fe_2O_3 is lower than that of FeS_2. Hence the combination shown in Figure 5.18(b) is the expected junction between these two semiconductors. This combination could not support the electron transfer between two particles, which means that each photocatalyst acts separately to produce H_2 and O_2. However, the efficiency of this combination was not satisfied (see table 4.7).

Further investigations were performed involving the electron mediator (redox mediators). In this case, it is assumed that the redox mediator support the electron transfer between the two semiconductors. The proposed process is depicted in Figure 5.20. Here FeS_2 (in the reaction $Co-Cat/FeS_2$) reduces water to H_2 via
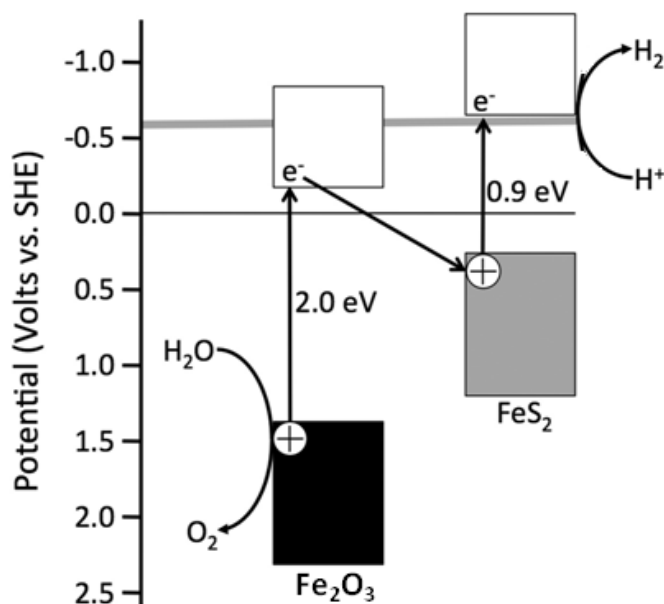
Figure 5.19: Illustration of the band gaps and band alignments for hematite and pyrite. Solid thin and thick gray horizontal lines indicate the E_{fb} values of hematite and pyrite, respectively. This illustration depicts how to perform these two semiconductors in a combination such as a tandem cell. Reprinted with permission from [39].©2012 Mineralogical Society of America.

the photogenerated electrons, and the photogenerated holes oxidize D (electron donor, in the reaction I^-) to A (electron acceptor, in the reaction IO_3^-). On the other hand, on Fe_2O_3 (in the reaction Co-Cat/ Fe_2O_3) the photogenerated electrons reduce A (IO_3^-) back to the D (I^-), while the holes oxidize H_2O to O_2.

In the present study a combination of IO_3^-/I^- was used as the reversible redox mediator. The results are presented in table 4.7. These results indicate that the rates of H_2 and O_2 production were improved when the redox mediator was applied. The interesting point is that almost a stoichiometric ratio for the overall water splitting has been obtained. As mentioned, for a stoichiometric overall water splitting the H_2 amount should be twice as high as the O_2 amount. In three experiments the concentration of IO_3^-/I^- was changed to determine the best concentration ratio for simultaneous H_2 and O_2 production. The combination of 0.1 M I^- and 2.5 mM IO_3^- lead to the highest H_2 evolution rate while the combination of 0.1 M for both IO_3^- and I^- produced the highest O_2 evolution rate.

Abe *et al.* [91] have investigated the simultaneous H_2 and O_2 production in a
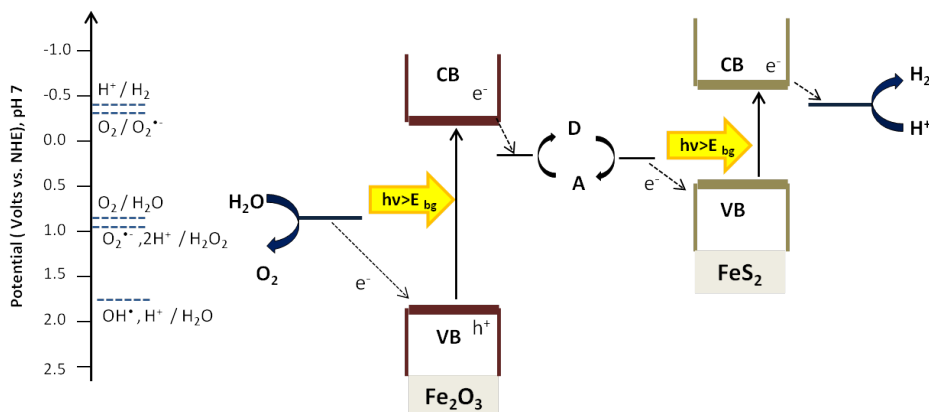
Figure 5.20: Schematic illustration of how to perform Z-scheme water splitting system using Fe_2O_3 as the O_2 evolution photocatalyst, FeS_2 as the H_2 evolution photocatalyst, and a redox couple. On the left side, the standard potential energy diagram for the water splitting is presented in V vs. NHE at pH 7.

Z-scheme system employing IO_3^-/I^- as the shuttle redox couple for different photocatalyst couples (such as TiO_2-rutile/Pt-WO_3 or Pt-TiO_2-anatase/Pt-$SrTiO_3$ and other combinations). The authors investigated the effect of different concentrations and pH values for the mediator. Indeed they observed the highest H_2 production rate at a low concentration of IO_3^-, as observed in the present study. Moreover, basic pH was more favorable and proved the water splitting reactions. However, in the present study, the Fe_2O_3 was not stable at basic pH and no O_2 evolution could be detected.

For a better interpretation of the results, an energy diagram of both Fe_2O_3 and FeS_2 along with their band gap energies in eV is shown in Figure 5.21. On the left side, the standard potentials of the redox couples in this system are presented in V vs. NHE at pH 7 (for I_3^-/I^- is +0.54 V vs. NHE at pH7, for IO_3^-/I^- is +0.67 V vs. NHE at pH 7). The pH value was 7 in all investigations presented in section 4.6.2.

The position of the standard potentials of the IO_3^-/I^- is more or less the same as the valence band position of FeS_2 ($\sim + 0.6$ V vs. NHE, pH 7). This position is determined according to the reported value in the literature for the conduction band edge level and band gap energy of pyrite, therefore if the band gap energy is more than 1 eV (which was determined in the present work and some other reports [30, 37, 38].) this level could also be appropriate for the IO_3^-/I^- redox couple as
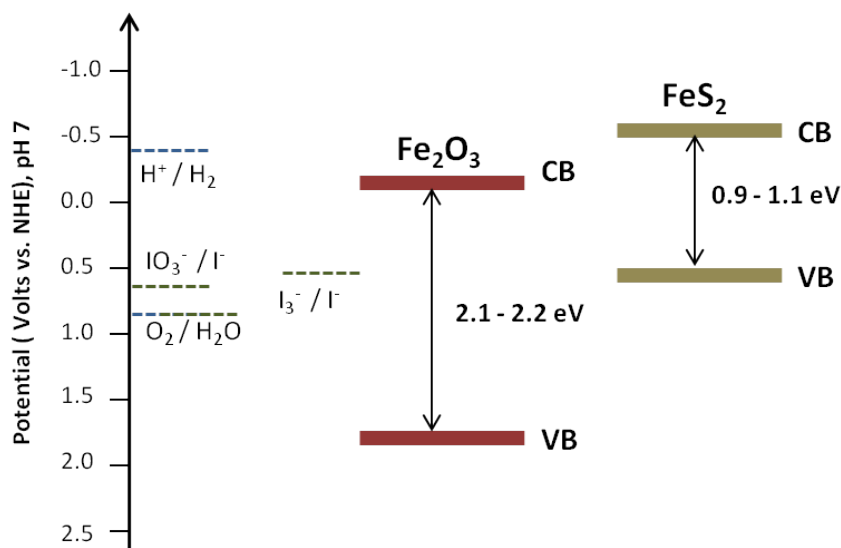
Figure 5.21: Schematic diagram of the energy levels between Fe_2O_3, FeS_2, and the redox couples (IO_3^-/I^- and I_3^-/I^-) in the water at pH 7

well.

Furthermore, it should be considered that in some experiments the concentration of IO_3^-/I^- was not same. This lead to changes in the redox potential based on the Nernst equation:

$$E \approx E^0 + \frac{0.059V}{z_e} \ln \frac{[Ox]}{[Red]} \tag{5.27}$$

Here z_e is the number of transferred electrons in half-reaction (reaction 5.29). For example when $[IO_3^-] = 0.02$ mM and $[I^-] = 0.1$ M, gives $E_{IO_3^-/I^-} = 0.63$V vs. NHE at pH 7.

The proposed mechanism for each photocatalyst will be:

- Generation of charge carriers in both photocatalysts (with a visible light source $\lambda > 420$ nm):

$$h\nu \longrightarrow e^- + h^+ \tag{5.28}$$

- The reactions occuring on the O_2 evolution photocatalyst will be: water oxidation by the holes to produce O_2 on the Fe_2O_3 (reaction 5.13) and e^- reduce IO_3^- to I^-:

$$IO_3^- + 3\,H_2O + 6\,e^- \longrightarrow I^- + 6\,OH^- \tag{5.29}$$
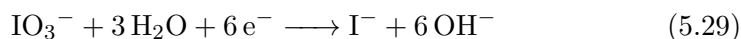
- The reactions on the H_2 evolution photocatalyst will be: water reduction by

the electrons to produce H_2 on the FeS_2 (reaction 5.24) and oxidation of I^- to I_3^- or IO_3^- via holes:

$$3\,I^- + 2\,h^+ \longrightarrow I_3^- \tag{5.30}$$

$$3\,I^- + 6\,h^+ + 6\,OH^- \longrightarrow IO_3^- + 3\,H_2O \tag{5.31}$$
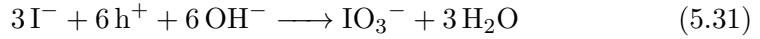
- It should be noted that each reaction which involved IO_3^-, I_3^- and I^- species has a backward reaction as well. In fact, reaction 5.31 is the backward reaction of reaction 5.29.

As mentioned, higher I^- concentration promotes the H_2 evolution rate. Based on this fact, the following process could be assumed; step 1: the water reduction to H_2 and I^- oxidation to IO_3^- (or first to I_3^- then to IO_3^-) over Co-Cat/FeS_2, step 2: reduction of IO_3^- to I^- and water oxidation to O_2 over Co-Cat/Fe_2O_3. However, in the case that the concentration of both species was the same, these two reaction could eventually occur at the same time.

The last experiments in this system involved NiO-Pt/FeS_2 and RuO_2-Pt/Fe_2O_3 as the photocatalysts. Here Pt was loaded on NiO/FeS_2 and RuO_2/Fe_2O_3 to improve the efficiency. In this case simultaneous H_2 and O_2 production in a ration of 2:1 was detected.

Two co-catalyst systems have been shown to be a good strategy for improving the activity of the water splitting reaction. In some investigations, the co-loading was developed in a core-shell structure (noble metal as core/metal oxide as shell) [84, 94, 183]. However, this strategy was only effective for the large band gap materials, which are able to produce both H_2 and O_2 at the same time. For example, Ta_3N_5 was modified with Pt and IrO_2 nanoparticles [183]. The high activity of this modification is due to the core/shell structure and the existence of two co-catalysts for the collection of both electrons and holes. The electron and hole transport are rectified and the photocatalytic activity is improved.

5.5.3 Efficiency of the Z-Scheme System

Discussion of the efficiency of the applied dual photocatalyst system (α-Fe_2O_3 and FeS_2) is important for utilizing and improvements of the system. In this section, the theoretical conversion efficiency of the dual system of α-Fe_2O_3/FeS_2 will be calculated.

Bolton *et al.* [12] calculated ideal solar conversion efficiencies of single-bandgap

and dual-bandgap systems. For example, the maximum efficiency for a dual system was $\sim 27\%$ for two semiconductors with band gaps of 1.7 and 1.1 eV.

The conversion efficiency of incident solar energy to chemical (Gibbs) energy was calculated based on the following equation:

$$\eta = \frac{J_g \cdot \mu_{ex} \cdot \phi_{conv}}{S} \qquad (5.32)$$

J_g: absorbed photon flux (photons $s^{-1}m^{-2}$), μ_{ex}: excess chemical potential generated by the system by absorption of light ($237.2\,\text{kJ}\,\text{mol}^{-1}$), ϕ_{conv}: quantum yield for conversion of absorbed photons into products, S: total incident solar irradiance ($\text{W}\,\text{m}^{-2}$).

Bolton *et al.* used solar spectral irradiance for their calculation. In fact eq. (5.32) could be adapted for other light spectra too. J_g is usually calculated from the wavelength which is $\lambda \leq \lambda_g$ (λ_g wavelength correspond to the band gap energy). In the present study, two photocatalysts are involved in the reaction. Here it is considered that the photon flux for both photocatalysts is equal, and is calculated for a wavelength between 420 - 660 nm. S is calculated from the irradiance of the used Xe arc lamp, and ϕ_{conv} is 0.25 for a dual system [12]. These figures give a conversion efficiency of $\sim 14\%$ for the system.

This calculated efficiency is much higher than observed hydrogen formation in the Z- Scheme system. For example, the H_2 evolution rate of $0.25\,\mu\text{mol}\,\text{h}^{-1}$ gives the efficiency of 3×10^{-3} %. This means that the overall energy conversion efficiency of this system is very low and far from practical application.

6 Summary and Conclusions

Photoelectrochemical and photocatalytic water splitting to form molecular hydrogen and oxygen using solar energy are two approaches to achieve clean and renewable energy. The aim of this thesis was water splitting under visible light irradiation because only in this way could solar light efficiently be utilized. Two iron-based semiconductors were applied as photocatalysts.

Overall water splitting using visible light irradiation and just one photocatalyst seems difficult because the photocatalyst which is usually able to perform this reaction has a large band gap and is most likely not visible light active. Based on this fact, it was practical to use two photocatalysts with smaller band gaps, so that one of them was suitable for the H_2 evolution reaction and the other one for the O_2 evolution reaction.

The two earth-abundant and iron-based semiconductors in this study were hematite (α-Fe_2O_3) and pyrite (FeS_2). The band gap energies of these two semiconductors allow them to be visible light active. In addition, due to the position of their band gaps, hematite is only able to produce O_2 while pyrite can only produce H_2.

In the present study nanocrystalline pyrite and hematite were first successfully synthesized. It is widely believed that nanocrystalline materials have some advantages, such as shorter charge transport pathways and larger redox active surface areas. Due to these properties the efficiency of the process could be improved. The synthesized nanoparticles and commercially available powders were employed to prepare electrodes or used as the photocatalysts in PC O_2 or H_2 evolution systems.

The PEC measurements were performed to determine the I-V characteristics behavior of hematite and pyrite in the dark and under illumination. In addition, the specific area of I-V curves which is responsible for the water oxidation or water reduction reaction was investigated. The results of the photoelectrochemical measurements of the hematite electrodes indicate that high thermal treatment (600 °C and 700 °C) has a positive effect, photoactivity was increased and the overpotential of water oxidation reaction in some experiments was clearly decreased. The PEC measurements of pyrite electrodes demonstrated that this material is very sensitive

and photocorroded during the measurements. Furthermore, impedance measurements were performed and the flat-band potentials and the donor density of both photoelectrodes were determined.

One main objective of the thesis was to develop a system which is able to do overall water splitting under visible light irradiation. The literature and the PEC measurements made it clear that hematite is an oxygen evolution photocatalyst and pyrite a hydrogen evolution photocatalyst. In order to find the best combination for a Z-scheme water splitting system, each photocatalyst was individually studied. In this process the synthesized nanoparticles were used first and then the commercially available powders. Moreover, the commercially available powders were investigated extensively to determine the effect of Co-Cat loading and sacrificial reagents in each individual reaction.

Photocatalytic water oxidation was investigated employing Fe_2O_3 (or Co-Cat/Fe_2O_3) as the photocatalyst under visible illumination. The surface of the photocatalyst was loaded with different noble metals or metal oxides to improve the photocatalytic activity. In pure water, no O_2 evolution was observed, therefore in all experiments Fe^{3+} was used as a sacrificial electron scavenger. The O_2 evolution rate was clearly increased in Co-Cat modified Fe_2O_3 compared to bare Fe_2O_3. Metal oxides such as RuO_2 and CuO improve the water oxidation reactions more than noble metals such as Pt and Au. The O_2 production rate was highest over Ru/Fe_2O_3 (0.15 µmol h^{-1}, $\zeta = 1.83 \times 10^{-3}$ %) and lowest over IrO_2/Fe_2O_3 (0.01 µmol h^{-1}, ($\zeta = 0.13 \times 10^{-3}$ %) and Cr_2O_3/Fe_2O_3 (0 µmol h^{-1}).

Photocatalytic hydrogen formation was investigated employing FeS_2 (or Co-Cat/FeS_2) as the photocatalyst under visible light irradiation. In pure water, no H_2 evolution was detected, which is why sulfide and sulfite were used as sacrificial reagents (electron donors). These reagents promoted hydrogen evolution reactions and also prevented FeS_2 from photocorrosion. The pyrite particles have been modified with different metals and metal oxides. Both the modified FeS_2 and the unmodified pyrite particles are able to produce molecular H_2 in the presence of sacrificial reagents. NiO/FeS_2 and RuO_2/FeS_2 showed the highest 14.65 µmol h^{-1} (ζ = 6.66 $\times 10^{-2}$ %) and the lowest 5.19 µmol h^{-1} ($\zeta = 2.36 \times 10^{-2}$ %) photocatalytic activity for H_2 production, respectively. The theoretical maximum efficiency of this system (single photocatalyst, and absorbed photon flux between 420 - 660 nm) will be $\sim$ 29 %.

The most active O_2 and H_2 evolution photocatalysts were selected to determine their performance in a Z-scheme water splitting system. The first investigation

of this system indicated that the best performance occurs in the presence of a redox couple. Different concentration combinations of IO_3^-/I^- were chosen as the shuttle redox couple. A system of NiO/FeS_2-RuO_2/Fe_2O_3 and 0.1 M of IO_3^-/I^- as the shuttle redox couple produced the highest simultaneous rate of production of H_2 (0.23 μmol h^{-1}) and O_2 (0.15 μmol h^{-1}). By loading Pt on NiO/FeS_2 and RuO_2/Fe_2O_3 system, H_2 and O_2 were evolved in a stoichiometric ratio of 2:1.

From the PEC measurements in this thesis it can be concluded that in the case of hematite electrodes, high-temperature treatment is required to obtain a good water oxidation rate. On the other hand, pyrite electrodes are unstable in water and under illumination. Photocorrosion is one of the main issues in the use of this material as a photoelectrode (photocathode) in the PEC systems. Therefore developing protection layers for pyrite electrodes should be considered. If these two photoelectrodes (α-Fe_2O_3/FeS_2) are planned to be applied in a tandem cell configuration, protection layers are needed to fulfill all requirements of a tandem device structure.

From the PC investigation it can be concluded that hematite and pyrite are able to produce O_2 and H_2, respectively, in the presence of sacrificial reagents. However, the conversion efficiency was not remarkable compared to the theoretical maximum efficiency of the system ($\sim$ 29 %). Simultaneous H_2 and O_2 productions were succeeded by the combination of both photocatalysts in the z-scheme system. Here overall water splitting under visible light irradiation could be observed. Hence the goal of this thesis was achieved. Furthermore, it can be concluded that the charge transfer between the two photocatalysts is improved by means of the shuttle redox mediator. In the design of new Z-scheme systems, suitable redox mediators play an important role. In this context changing the pH or the concentration (ratio of Red/Ox) may improve photocatalytic efficiency.

References

(1) Boettcher, S. W.; Mallouk, T. E.; Osterloh, F. E. Themed issue on water splitting and photocatalysis. *Journal of Materials Chemistry A* **2016**, *4*, 2764–2765.

(2) Connolly, J., *Photochemical conversion and storage of solar energy*; Elsevier Science: 2012.

(3) Grätzel, M. Photoelectrochemical cells. *Nature* **2001**, *414*, 338–344.

(4) Sivula, K.; Le Formal, F.; Grätzel, M. Solar water splitting: progress using hematite (α-Fe$_2$O$_3$) photoelectrodes. *ChemSusChem* **2011**, *4*, 432–449.

(5) Kudo, A.; Miseki, Y. Heterogeneous photocatalyst materials for water splitting. *Chemical Society reviews* **2009**, *38*, 253–78.

(6) Hisatomi, T.; Kubota, J.; Domen, K. Recent advances in semiconductors for photocatalytic and photoelectrochemical water splitting. *Chemical Society Reviews* **2014**, *43*, 7520–7535.

(7) Fujishima, A.; Honda, K. Electrochemical photolysis of water at a semiconductor electrode. *Nature* **1972**, *238*, 37–38.

(8) Seger, B.; Castelli, I. E.; Vesborg, P. C. K.; Jacobsen, K. W.; Hansen, O.; Chorkendorff, I. 2-Photon tandem device for water splitting: comparing photocathode first versus photoanode first designs. *Energy & Environmental Science* **2014**, *7*, 2397–2413.

(9) Weber, M. F.; Dignam, M. J. Splitting water with semiconducting photoelectrodes efficiency considerations. *International Journal of Hydrogen Energy* **1986**, *11*, 225–232.

(10) Varghese, O. K.; Grimes, C. A. Appropriate strategies for determining the photoconversion efficiency of water photoelectrolysis cells: a review with examples using titania nanotube array photoanodes. *Solar Energy Materials and Solar Cells* **2008**, *92*, 374–384.

References

(11)   Osterloh, F. E., Nanoscale effects in water splitting photocatalysis. In *Topics in current chemistry, "solar energy for fuels"*, Tüysüz, H., Chan, C. K., Eds.; Springer International Publishing: 2015; Vol. 371, pp 105–142.

(12)   Bolton, J. R.; Strickler, S. J.; Connolly, J. S. Limiting and realizable efficiencies of solar photolysis of water. *Nature* **1985**, *316*, 495–500.

(13)   Walter, M. G.; Warren, E. L.; McKone, J. R.; Boettcher, S. W.; Mi, Q.; Santori, E. A.; Lewis, N. S. Solar water splitting cells. *Chemical Reviews* **2010**, *110*, 6446–6473.

(14)   Kato, H.; Sasaki, Y.; Shirakura, N.; Kudo, A. Synthesis of highly active rhodium-doped $SrTiO_3$ powders in z-scheme systems for visible-light-driven photocatalytic overall water splitting. *Journal of Materials Chemistry A* **2013**, *1*, 12327.

(15)   Holleman, A.; Wiberg, E., *Lehrbuch der Anorganischen Chemie*, 34. Edition; Walter de Gruyter: 1995.

(16)   Shuey, R. T., *Devlopment in economic geology 4, semiconducting ore minerals*; Elsevier: 1975.

(17)   Cornell, R. M.; Schwertmann, U., *The iron oxides: structure, properties, reactions, occurrences and uses*; Wiley-VCH: 1996.

(18)   Sivula, K.; Zboril, R.; Formal, F. L.; Robert, R.; Weidenkaff, A.; Tucek, J.; Frydrych, J.; Grätzel, M. Photoelectrochemical water splitting with mesoporous hematite prepared by a solution-based colloidal approach. *American Chemical Society* **2010**, *132*, 7436–7444.

(19)   Debnath, N. C.; Anderson, A. Optical spectra of ferrous and ferric oxides and the passive film: a molecular obital study. *Journal of The Electrochemical Society* **1982**, *129*, 2169.

(20)   Badia-Bou, L.; Mas Marza, E.; Rodenas, P.; Barea, E. M.; Fabregat-Santiago, F.; Gimenez, S.; Peris, E. V.; Bisquert, J. Water oxidation at hematite photoelectrodes with an iridium-based catalyst. *The Journal of Physical Chemistry C* **2013**, *117*, 3826–3833.

(21)   Kennedy, J. H.; Frese, K. W. Photooxidation of water at α-Fe_2O_3 electrodes. *Journal of The Electrochemical Society* **1978**, *125*, 709–714.

(22)   Misho, R. H.; Murad, W. A. Band gap measurements in thin films of hematite Fe_2O_3, pyrite FeS_2 and troilite FeS prepared by chemical spray pyrolysis. *Solar Energy Materials and Solar Cells* **1992**, *27*, 335–345.

(23) Lindgren, T.; Vayssieres, L.; Wang, H.; Lindquist, S.-E., Photo-oxidation of water at hematite electrodes. In *Chemical physics of nanostructured semiconductors*, Kokorin, A. I., Bahnemann, D., Eds.; November 2015; Taylor & Francis: 2003, pp 83–110.

(24) Hankin, a.; Alexander, J. C.; Kelsall, G. H. Constraints to the flat band potential of hematite photo-electrodes. *Phys Chem Chem Phys* **2014**, *16*, 16176–16186.

(25) Kleiman-shwarsctein, A.; Hu, Y.-s.; Forman, A. J.; Stucky, G. D.; Mcfarland, E. W. Electrodeposition of α-Fe$_2$O$_3$ doped with Mo or Cr as photoanodes for photocatalytic water splitting. *Journal of Physical Chemistry* **2008**, *112*, 15900–15907.

(26) Beermann, N.; Vayssieres, L.; Lindquist, S.-E.; Hagfeldt, A. Photoelectrochemical studies of oriented nanorod thin films of hematite. *Journal of The Electrochemical Society* **2000**, *147*, 2456.

(27) Yong, X.; Schoonen, M. A. A. The absolute energy positions of conduction and valence bands of selected semiconducting minerals. *American Mineralogist* **2000**, *85*, 543–556.

(28) Dare-Edwards, M. P.; Goodenough, J. B.; Hamnett, A.; Trevellick, P. R. Electrochemistry and photoelectrochemistry of iron(III) oxide. *Journal of the Chemical Society, Faraday Transactions* **1983**, *79*, 2027.

(29) Bragg, W. L. The analysis of crystals by the X-ray spectrometer. *The Royal Society* **1914**, *89*, 468.

(30) Ennaoui, A.; Fiechter, S.; Pettenkofer, C.; Alonso-Vante, N.; Büker, K.; Bronold, M.; Höpfner, C.; Tributsch, H. Iron disulfide for solar energy conversion. *Solar Energy Materials and Solar Cells* **1993**, *29*, 289–370.

(31) Mishra, K.; Osseo Asare, K. Aspects of the interfacial electrochemistry of semiconductor pyrite (FeS$_2$). *Journal of The Electrochemical Society* **1988**, *135*, 2502–2509.

(32) Jaegermann, W.; Tributsch, H. Photoelectrochemical reactions of FeS$_2$ (pyrite) with H$_2$O and reducing agents. *Journal of applied electrochemistry* **1983**, *13*, 743–750.

(33) Ennaoui, A.; Tributsch, H. Energetic characterization of the photoactive FeS$_2$ (pyrite) interface. *Solar Energy Materials* **1986**, *14*, 461–474.

References

(34) Wei, D.; Osseo-Asare, K. Semiconductor electrochemistry of particulate pyrite. *Journal of The Electrochemical Society* **1997**, *144*, 546.

(35) Ennaoui, A.; Fiechter, S.; Jaegermann, W.; Tributsch, H. Photoelectrochemistry of highly quantum efficient single-crystalline n-FeS$_2$ (Pyrite). *Journal of The Electrochemical Society* **1986**, *133*, 97–106.

(36) Thomas, B.; Ellmer, K.; Mfiller, M.; Spfner, C. H.; Fiechter, S.; Tributsch, H. Structural and photoelectrical properties of FeS$_2$ (pyrite) thin films grown by MOCVD. *Journal of Crystal Growth* **1997**, *170*, 808–812.

(37) Rickard, D.; Luther, G. W. Chemistry of iron sulfides. *Chemical Reviews* **2007**, *107*, 514–562.

(38) Eyert, V.; Höck, K.; Fiechter, S.; Tributsch, H. Electronic structure of FeS$_2$: the crucial role of electron-lattice interaction. *Physical Review B* **1998**, *57*, 6350–6359.

(39) Eggleston, C. M.; Stern, J. R.; Strellis, T. M.; Parkinson, B. a. A natural photoelectrochemical cell for water splitting: implications for early Earth and Mars. *American Mineralogist* **2012**, *97*, 1804–1807.

(40) Maeda, K.; Domen, K. New non-oxide photocatalysts designed for overall water splitting under visible light. *Journal of Physical Chemistry C* **2007**, *111*, 7851–7861.

(41) Hardee, K. L.; Bard, A. J. Semiconductor electrodes V . The application of chemically vapor deposited iron oxide films to photosensitized electrolysis. *Journal of The Electrochemical Society* **1976**, *123*, 1024–1026.

(42) Sivula, K. Metal oxide photoelectrodes for solar fuel production, surface traps, and catalysis. *The Journal of Physical Chemistry Letters* **2013**, *4*, 1624–1633.

(43) Itoh, K.; Bockris, J. O. Thin film photoelectrochemistry: iron oxide. *Journal of The Electrochemical Society* **1984**, *131*, 1266–1271.

(44) Itoh, K.; Bockris, J. O. M. Stacked thin-film photoelectrode using iron oxide. *Journal of Applied Physics* **1984**, *56*, 874–876.

(45) Young, K. M. H.; Klahr, B. M.; Zandi, O.; Hamann, T. W. Photocatalytic water oxidation with hematite electrodes. *Catalysis Science & Technology* **2013**, *3*, 1660.

(46) Le Formal, F.; Grätzel, M.; Sivula, K. Controlling photoactivity in ultra-thin hematite films for solar water-splitting. *Advanced Functional Materials* **2010**, *20*, 1099–1107.

(47) Tilley, S. D.; Cornuz, M.; Sivula, K.; Grätzel, M. Light-induced water splitting with hematite: improved nanostructure and iridium oxide catalysis. *Angewandte Chemie (International ed. in English)* **2010**, *49*, 6405–8.

(48) Ni, M.; Leung, M. K. H.; Leung, D. Y. C.; Sumathy, K. A review and recent developments in photocatalytic water-splitting using TiO_2 for hydrogen production. *Renewable and Sustainable Energy Reviews* **2007**, *11*, 401–425.

(49) Memming, R., *Semiconductor electrochemistry*; Wiley-VCH: 2001, pp 332–367.

(50) Li, X. P.; Vante, N. A.; Tributsch, H. Involvement of coordination chemistry during electron transfer in the stabilization of the pyrite (FeS_2) photoanode. *Journal of Electroanalytical Chemistry* **1988**, *242*, 255–264.

(51) Chen, X.; Shen, S.; Guo, L.; Mao, S. S. Semiconductor-based photocatalytic hydrogen generation. *Chemical reviews* **2010**, *110*, 6503–70.

(52) Yamaguti, K.; Sato, S. Photolysis of water over metallized powdered titanium dioxide. *Journal of the Chemical Society, Faraday Transactions 1: Physical Chemistry in Condensed Phases* **1985**, *81*, 1237.

(53) Park, H.; Park, Y.; Kim, W.; Choi, W. Surface modification of TiO_2 photocatalyst for environmental applications. *Journal of Photochemistry and Photobiology C: Photochemistry Reviews* **2013**, *15*, 1–20.

(54) Iwase, A.; Kato, H.; Kudo, A. Nanosized Au particles as an efficient cocatalyst for photocatalytic overall water splitting. *Catalysis Letters* **2006**, *108*, 7–10.

(55) Ismail, A. A.; Hakki, A.; Bahnemann, D. W. Mesostructure Au/TiO_2 nanocomposites for highly efficient catalytic reduction of p-nitrophenol. *Journal of Molecular Catalysis A: Chemical* **2012**, *358*, 145–151.

(56) Ismail, A. A.; Bahnemann, D. W. Synthesis of TiO_2/Au nanocomposites via Sol-Gel process for photooxidation of methanol. *Journal of Advanced Oxidation Technologies* **2009**, *12*, 9–15.

(57) Domen, K.; Naito, S.; Soma, M.; Onishi, T.; Tamaru, K. Photocatalytic decomposition of water vapour on an $NiO-SrTiO_3$ catalyst. *J. Chem. Soc., Chem. Commun.* **1980**, *0*, 543–544.

References

(58) Ismail, A. A.; Bahnemann, D. W. Mesostructured Pt /TiO$_2$ nanocomposites as highly active photocatalysts for the photooxidation of dichloroacetic acid. *The Journal of Physical Chemistry C* **2011**, *115*, 5784–5791.

(59) Duonghong, D.; Borgarello, E.; Grätzel, M. Dynamics of light-induced water cleavage in colloidal systems. *Journal of the American Chemical Society* **1981**, *103*, 4685–4690.

(60) Dung, D.; Ramsden, J.; Grätzel, M. Dynamics of interfacial electron-transfer processes in colloidal semiconductor systems. *Journal of the American Chemical Society* **1982**, *104*, 2977–2985.

(61) Teramura, K.; Maeda, K.; Saito, T.; Takata, T.; Saito, N.; Inoue, Y.; Domen, K. Characterization of ruthenium oxide nanocluster as a cocatalyst with (Ga$_{1-x}$Zn$_x$) (N$_{1-x}$O$_x$) for photocatalytic overall water splitting. *Journal of Physical Chemistry B* **2005**, *109*, 21915–21921.

(62) Kandiel, T. A.; Ismail, A. A.; Bahnemann, D. W. Mesoporous TiO$_2$ nanostructures: a route to minimize Pt loading on titania photocatalysts for hydrogen production. *Physical chemistry chemical physics* **2011**, *13*, 20155–61.

(63) Linsebigler, A. L.; Lu, G.; Yates, J. T. Photocatalysis on TiO$_2$ surfaces: principles, mechanisms, and selected results. *Chemical Reviews* **1995**, *95*, 735–758.

(64) Maeda, K.; Higashi, M.; Lu, D.; Abe, R.; Domen, K. Efficient nonsacrificial water splitting through two-step photoexcitation by visible light using a modified oxynitride as a hydrogen evolution photocatalyst. *Journal of the American Chemical Society* **2010**, *132*, 5858–5868.

(65) Iwase, A.; Kato, H.; Kudo, A. A novel photodeposition method in the presence of nitrate ions for loading of an iridium oxide cocatalyst for water splitting. *Chemistry Letters* **2005**, *34*, 946–947.

(66) Guijarro, N.; Prévot, M.; Sivula, K. Enhancing the charge separation in nanocrystalline Cu$_2$ZnSnS$_4$ photocathodes for photoelectrochemical application: the role of surface modifications. *The Journal of Physical Chemistry Letters* **2014**, *5*, 3902–3908.

(67) Hodes, G.; Howell, I.; Peter, L. A new concept in photovoltaic cells. *Journal of The Electrochemical Society* **1992**, *139*, 3136–3140.

(68) Sabio, E. M.; Chamousis, R. L.; Browning, N. D.; Osterloh, F. E. Photocatalytic water splitting with suspended calcium niobium oxides: why nanoscale is better than bulk - a kinetic analysis. *Journal of Physical Chemistry C* **2012**, *116*, 3161–3170.

(69) Osterloh, F. E. Inorganic nanostructures for photoelectrochemical and photocatalytic water splitting. *Chemical Society reviews* **2013**, *42*, 2294–320.

(70) Chamousis, R. L.; Osterloh, F. E. Use of potential determining ions to control energetics and photochemical charge transfer of a nanoscale water splitting photocatalyst. *Energy & Environmental Science* **2014**, *7*, 736.

(71) Nail, B. A.; Fields, J. M.; Zhao, J.; Wang, J.; Greaney, M. J.; Brutchey, R. L.; Osterloh, F. E. Nickel oxide particles catalyze photochemical hydrogen evolution from water-nanoscaling promotes p-type character and minority carrier extraction. *ACS Nano* **2015**, *9*, 5135–5142.

(72) O'Regan, B.; Grätzel, M. A low-cost, high-efficiency solar cell based on dye-sensitized colloidal TiO_2 films. *Nature* **1991**, *353*, 737–740.

(73) Paracchino, A.; Laporte, V.; Sivula, K.; Grätzel, M.; Thimsen, E. Highly active oxide photocathode for photoelectrochemical water reduction. *Nature materials* **2011**, *10*, 456–61.

(74) Brillet, J.; Cornuz, M.; Formal, F. L.; Yum, J.-H.; Grätzel, M.; Sivula, K. Examining architectures of photoanode–photovoltaic tandem cells for solar water splitting. *Journal of Materials Research* **2010**, *25*, 17–24.

(75) Saito, K.; Koga, K.; Kudo, A. Lithium niobate nanowires for photocatalytic water splitting. *Dalton Transactions* **2011**, *40*, 3909–3913.

(76) Yan, S.; Wan, L.; Li, Z.; Zou, Z. Facile temperature-controlled synthesis of hexagonal Zn_2GeO_4 nanorods with different aspect ratios toward improved photocatalytic activity for overall water splitting and photoreduction of CO_2. *Chemical communications* **2011**, *47*, 5632–5634.

(77) Yokoi, T.; Sakuma, J.; Maeda, K.; Domen, K.; Tatsumi, T.; Kondo, J. N. Preparation of a colloidal array of $NaTaO_3$ nanoparticles via a confined space synthesis route and its photocatalytic application. *Physical Chemistry Chemical Physics* **2011**, *13*, 2563–2570.

(78) Memming, R., Photoinduced charge transfer processes at semiconductor electrodes and particles. In *Topics in current chemistry, Electron transfer I*, Mattay, J., Ed.; Springer Berlin Heidelberg: 1994; Vol. 169, pp 105–181.

References

(79) Hagfeldt, A.; Grätzel, M. Light-induced redox reactions in nanocrystalline systems. *Chemical Reviews* **1995**, *95*, 49–68.

(80) O'Regan, B.; Moser, J.; Anderson, M.; Grätzel, M. Vectorial electron injection into transparent semiconductor membranes and electric field effects on the dynamics of light-induced charge separation. *Journal of Physical Chemistry* **1990**, *94*, 8720–8726.

(81) Schneider, J.; Kandiel, T. A.; Bahnemann, D. W., Solar photocatalytic hydrogen production: current status and future challenges. In *Materials and processes for solar fuel production*, Viswanathan, B., Subramanian, V. R., Lee, J. S., Eds.; Springer New York: 2014; Vol. 174 of the series "Nanostructure Science and Technology", pp 41–74.

(82) Wardman, P. Reduction potentials of one-electron couples involving free radicals in aqueous solution. *J. Phys Chem. Ref. Data* **1989**, *18*, 1637–1753.

(83) Kato, H.; Asakura, K.; Kudo, A. Highly efficient water splitting into H_2 and O_2 over lanthanum-doped $NaTaO_3$ photocatalysts with high crystallinity and surface nanostructure. *Journal of the American Chemical Society* **2003**, *125*, 3082–3089.

(84) Kato, H.; Kudo, A. Photocatalytic water splitting into H_2 and O_2 over various tantalate photocatalysts. *Catalysis Today* **2003**, *78*, 561–569.

(85) Kato, H.; Kudo, A. Highly efficient water splitting into H_2 and O_2 over lanthanum-doped $NaTaO_3$ photocatalysts with high crystallinity and surface nanostructure. *Journal of the American Chemical Society* **2003**, *125*, 3082–3089.

(86) Chen, D.; Ye, J. Selective-synthesis of high-performance single-crystalline $Sr_2Nb_2O_7$ nanoribbon and $SrNb_2O_6$ nanorod photocatalysts. *Chemistry of Materials* **2009**, *21*, 2327–2333.

(87) Kudo, A.; Kato, Hideki; Nakagawa, S. Water splitting into H_2 and O_2 on new $Sr_2M_2O_7$ (M = Nb and Ta) photocatalysts with layered perovskite structures: factors affecting the photocatalytic activity. *The Journal of Physical Chemistry B* **2000**, *104*.

(88) Li, X.; Low, J.; Yu, J., Photocatalytic hydrogen generation. In *Photocatalysis : applications*, Dionysiou, D. D., Li Puma, G., Ye, J., Schneider, J., Bahnemann, D., Eds.; 15; The Royal Society of Chemistry: 2016.

(89) Jing, D.; Guo, L. A novel method for the preparation of a highly stable and active CdS photocatalyst with a special surface nanostructure. *The journal of physical chemistry. B* **2006**, *110*, 11139–45.

(90) Bard, A. J. Photoelectrochemistry and heterogeneous photocatalysis at semi-conductors. *Journal of photochemistry* **1979**, *10*, 59–75.

(91) Abe, R.; Sayama, K.; Sugihara, H. Development of new photocatalytic water splitting into H_2 and O_2 using two different semiconductor photocatalysts and a shuttle redox mediator IO_3^-/I^-. *Journal of Physical Chemistry B* **2005**, *109*, 16052–16061.

(92) Sayama, K.; Mukasa, K.; Abe, R.; Abe, Y.; Arakawa, H. A new photo-catalytic water splitting system under visible light irradiation mimicking a Z-scheme mechanism in photosynthesis. *Journal of Photochemistry and Photobiology A: Chemistry* **2002**, *148*, 71–77.

(93) Wang, Q.; Hisatomi, T.; Ma, S. S. K.; Li, Y.; Domen, K. Core/shell structured La- and Rh-codoped $SrTiO_3$ as a hydrogen evolution photocatalyst in z-scheme overall water splitting under visible light irradiation. *Chemistry of Materials* **2014**, *26*, 4144–4150.

(94) Maeda, K.; Domen, K. Photocatalytic water splitting: recent progress and future challenges. *The Journal of Physical Chemistry Letters* **2010**, *1*, 2655–2661.

(95) Sasaki, Y.; Nemoto, H.; Saito, K.; Kudo, A. Solar water splitting using powdered photocatalysts driven by z-schematic interparticle electron transfer without an electron mediator. *Journal of Physical Chemistry C* **2009**, *113*, 17536–17542.

(96) Kisch, H., *Semiconductor photocatalysis: principles and applications*; Wiley-VCH: 2015.

(97) Maeda, K. Photocatalytic water splitting using semiconductor particles: history and recent developments. *Journal of Photochemistry and Photobiology C: Photochemistry Reviews* **2011**, *12*, 237–268.

(98) Marugán, J.; Hufschmidt, D.; López-Muñoz, M.-J.; Selzer, V.; Bahnemann, D. Photonic efficiency for methanol photooxidation and hydroxyl radical generation on silica-supported TiO_2 photocatalysts. *Applied Catalysis B: Environmental* **2006**, *62*, 201–207.

References

(99) Kandiel, T. A.; Dillert, R.; Robben, L.; Bahnemann, D. W. Photonic efficiency and mechanism of photocatalytic molecular hydrogen production over platinized titanium dioxide from aqueous methanol solutions. *Catalysis Today* **2011**, *161*, 196–201.

(100) Wang, C.-y.; Rabani, J.; Bahnemann, D. W.; Dohrmann, J. K. Photonic efficiency and quantum yield of formaldehyde formation from methanol in the presence of various TiO_2 photocatalysts. *Journal of Photochemistry and Photobiology A: Chemistry* **2002**, *148*, 169–176.

(101) Ismail, A. A.; Bahnemann, D. W. One-step synthesis of mesoporous platinum/titania nanocomposites as photocatalyst with enhanced photocatalytic activity for methanol oxidation. *Green Chemistry* **2011**, *13*, 428.

(102) Zong, X.; Yan, H.; Wu, G.; Ma, G.; Wen, F.; Wang, L.; Li, C. Enhancement of photocatalytic H_2 evolution on CdS by loading MoS_2 as cocatalyst under visible light irradiation. *Journal of the American Chemical Society* **2008**, *130*, 7176–7.

(103) Jang, J. S.; Ham, D. J.; Lakshminarasimhan, N.; Choi, W. Y.; Lee, J. S. Role of platinum-like tungsten carbide as cocatalyst of CdS photocatalyst for hydrogen production under visible light irradiation. *Applied Catalysis A: General* **2008**, *346*, 149–154.

(104) Jang, J.; Joshi, U.; Lee, J. Solvothermal synthesis of CdS nanowires for photocatalytic hydrogen and electricity production. *Journal of Physical Chemistry C* **2007**, *111*, 13280–13287.

(105) Hara, K.; Sayama, K.; Arakawa, H. Photocatalytic hydrogen and oxygen formation over SiO_2-supported RuS_2 in the presence of sacrificial donor and acceptor. *Applied Catalysis A: General* **1999**, *189*, 127–137.

(106) Ishikawa, A.; Takata, T.; Kondo, J. N.; Hara, M.; Kobayashi, H.; Kazunari, D. Oxysulfide $Sm_2Ti_2S_2O_5$ as a stable photocatalyst for water oxidation and reduction under visible light irradiation ($\lambda \leq 650$ nm). *Journal of the American Chemical Society* **2002**, *124*, 13547–13553.

(107) Meng, F.; Li, J.; Cushing, S. K.; Bright, J.; Zhi, M.; Rowley, J. D.; Hong, Z.; Manivannan, A.; Bristow, A. D.; Wu, N. Photocatalytic water oxidation by hematite/reduced graphene oxide composites. *ACS Catalysis* **2013**, *3*, 746–751.

(108) Darwent, J. R.; Mills, A. Photo-oxidation of water sensitized by WO_3 powder. *Journal of the Chemical Society, Faraday Transactions 2: Molecular and Chemical Physics* **1982**, *78*, 359–367.

(109) Ohmori, T.; Takahashi, H.; Mametsuka, H.; Suzuki, E. Photocatalytic oxygen evolution on α-Fe_2O_3 films using Fe^{3+} ion as a sacrifcial oxidizing agent. *Physical Chemistry Chemical Physics* **2000**, *2*, 3519–3522.

(110) Bamwenda, G. R.; Uesigi, T.; Abe, Y.; Sayama, K.; Arakawa, H. Photocatalytic oxidation of water to O_2 over pure CeO_2, WO_3, and TiO_2 using Fe^{3+} and Ce^{4+} as electron acceptors. *Applied Catalysis A: General* **2001**, *205*, 117–128.

(111) Schneider, J.; Bahnemann, D. Undesired Role of sacrificial reagents in photocatalysis. *The Journal of Physical Chemistry Letters* **2013**, *4*, 3479–3483.

(112) Hykaway, N.; Sears, W. M.; Morisaki, H.; Morrison, S. R. Current-doubling reactions on titanium dioxide photoanodes. *Journal of Physical Chemistry* **1986**, *90*, 6663–6667.

(113) Bao, N.; Shen, L.; Takata, T.; Domen, K. Self-templated synthesis of nanoporous CdS nanostructures for highly efficient photocatalytic hydrogen production under visible light. *Chemistry of Materials* **2008**, *20*, 110–117.

(114) Yan, H.; Yang, J.; Ma, G.; Wu, G.; Zong, X.; Lei, Z.; Shi, J.; Li, C. Visible-light-driven hydrogen production with extremely high quantum efficiency on PtPt/CdS photocatalyst. *Journal of Catalysis* **2009**, *266*, 165–168.

(115) Faust, B. C.; Hoffmann, M. R.; Bahnemann, D. W. Photocatalytic oxidation of sulfur dioxide in aqueous suspension of α-Fe_2O_3. *The Journal of Physical Chemistry* **1989**, *93*, 6371–6381.

(116) Bai, Y.; Yeom, J.; Yang, M.; Cha, S.-h.; Sun, K.; Kotov, N. A. Universal synthesis of single-phase pyrite FeS_2 nanoparticles, nanowires, and nanosheets. *The Journal of Physical Chemistry C* **2013**, *117*, 2567–2573.

(117) Brugger, P. A.; Cuendet, P.; Grätzel, M. Ultrafine and specific catalysts affording efficient hydrogen evolution from water under visible light illumination. *Journal of American Chemical society* **1981**, *103*, 2923–2927.

(118) Ito, S.; Chen, P.; Comte, P.; Nazeeruddin, M. K.; Liska, P.; Pechy, P.; Grätzel, M. Fabrication of screen-printing pastes from TiO_2 powders for dye-sensitised solar cells. *Progress in Photovoltaics: Research and Applications* **2007**, *(in press)*, DOI: `10.1002/pip.768`.

References

(119) Tauc, J.; Grigorovici, R.; Vancu, A. Optical properties and electronic structure of amorphous germanium. *Physica Status Solidi (B)* **1966**, *15*, 627–637.

(120) HACH. Das LANGE Küvetten-Test-System., `http://www.hach.com/`, Accessed: 2016-09-23.

(121) ZAHNER-elektrik GmbH & Co. KG. Products., `http://zahner.de/products/photoelectrochemistry/pec-cells.html`, Accessed:2016-09-08.

(122) Onari, S.; Arai, T.; Kudo, K. Infrared lattice vibrations and dielectric dispersion in α-Fe$_2$O$_3$. *Physical Review B* **1977**, *16*, 1717–1721.

(123) Landolt-Börnstein, Hematite (alpha-Fe$_2$O$_3$): optical properties, dielectric constants. In *Semiconductors "non-tetrahedrally bonded binary compounds II"*, Madelung, O., Rössler, U., Schulz, M., Eds.; Springer: 2000; Vol. 41D.

(124) Le Formal, F.; Tétreault, N.; Cornuz, M.; Moehl, T.; Grätzel, M.; Sivula, K. Passivating surface states on water splitting hematite photoanodes with alumina overlayers. *Chemical Science* **2011**, *2*, 737.

(125) Husk, D.; Seehra, M. Dielectric constant of iron pyrite (FeS$_2$). *Solid State Communications* **1978**, *27*, 1147–1148.

(126) Serpone, N. Relative photonic efficiencies and quantum yields in heterogeneous photocatalysis. *Journal of Photochemistry and Photobiology A: Chemistry* **1997**, *104*, 1–12.

(127) Carraro, M.; Sartorel, A.; Toma, F. M.; Puntoriero, F.; Scandola, F.; Campagna, S.; Prato, M.; Bonchio, M., Artificial photosynthesis challenges: water oxidation at nanostructured interfaces. In *Topics in current chemistry ,"photocatalysis"*, Bignozzi, C. A., Ed.; Springer: 2011; Vol. 303, pp 124–129.

(128) Ohno, T.; Tanigawa, F.; Fujihara, K.; Izumi, S.; Matsumura, M. Photocatalytic oxidation of water by visible light using ruthenium-doped titanium dioxide powder. *Journal of Photochemistry and Photobiology A: Chemistry* **1999**, *127*, 107–110.

(129) Maeda, K.; Domen, K., Surface nanostructures in photocatalysts for visible-light-driven water splitting. In *Topics in current chemistry ,"photocatalysis"*, Bignozzi, C. A., Ed.; Springer: 2011; Vol. 303, pp 95–119.

(130) Ismail, A. A.; Bahnemann, D. W.; Al-Sayari, S. A. Synthesis and photocatalytic properties of nanocrystalline Au, Pd and Pt photodeposited onto mesoporous RuO_2-TiO_2 nanocomposites. *Applied Catalysis A: General* **2012**, *431-432*, 62–68.

(131) Sakthivel, S.; Shankar, M. V.; Palanichamy, M.; Arabindoo, B.; Bahnemann, D. W.; Murugesan, V. Enhancement of photocatalytic activity by metal deposition: characterisation and photonic efficiency of Pt, Au and Pd deposited on TiO_2 catalyst. *Water research* **2004**, *38*, 3001–8.

(132) Hashimoto, K.; Irie, H.; Fujishima, A. TiO_2 photocatalysis: a historical overview and future prospects. *Japanese Journal of Applied Physics* **2005**, *44*, 8269–8285.

(133) Kennedy, J. H.; Anderman, M. Photoelectrolysis of water at α-Fe_2O_3 electrodes in acidic solution. *J. Electrochem. Soc.* **1983**, *130*, 848–852.

(134) Schwertmann, U. Solubility and dissolution of iron-oxides. *Plant Soil* **1991**, *130*, 1–25.

(135) Lalvani, S. B.; Shami, M. Electrochemical oxidation of pyrite slurries. *Journal of The Electrochemical Society* **1986**, *133*, 1364.

(136) Peters, E. Direct leaching of sulfides : chemistry and applications. *Metallurgical and Materials Transactions B* **1976**, *7B*, 505–517.

(137) James R. White, A. J. B. Electrochemical investigation of photocatalysis at CdS suspensions in the presence of methylviologen. *Journal of Chemical Information and Modeling* **2013**, *53*, 1689–1699.

(138) Aroutiounian, V. M.; Arakelyan, V. M.; Shahnazaryan, G. E.; Hovhannisyan, H. R.; Wang, H.; Turner, J. A. Photoelectrochemistry of tin-doped iron oxide electrodes. *Solar Energy* **2007**, *81*, 1369–1376.

(139) Yang, X.; Lian, X.; Liu, S.; Tian, J.; Jiang, C.; Wang, G.; Chen, J.; Wang, R. Investigation of enhanced photoelectrochemical property of cerium doped hematite film prepared by sol-gel route. *International Journal of Electrochemical Science* **2013**, *8*, 3721–3730.

(140) Dotan, H.; Sivula, K.; Grätzel, M.; Rothschild, A.; Warren, S. C. Probing the photoelectrochemical properties of hematite (α-Fe_2O_3) electrodes using hydrogen peroxide as a hole scavenger. *Energy & Environmental Science* **2011**, *4*, 958.

References

(141) Zandi, O.; Klahr, B. M.; Hamann, T. W. Highly photoactive Ti-doped α-Fe$_2$O$_3$ thin film electrodes: resurrection of the dead layer. *Energy & Environmental Science* **2013**, *6*, 634–642.

(142) Kay, A.; Cesar, I.; Grätzel, M. New benchmark for water photooxidation by nanostructured α-Fe$_2$O$_3$ films. *Journal of the American Chemical Society* **2006**, *128*, 15714–15721.

(143) Quinn, R. K.; Nasby, R.; Baughman, R. Photoassisted electrolysis of water using single crystal α-Fe$_2$O$_3$ anodes. *Materials Research Bulletin* **1976**, *11*, 1011–1017.

(144) Wilhelm, S. M.; Yun, K. S.; Ballenger, L. W.; Hackerman, N. Semiconductor properties of iron oxide electrodes. *Journal of The Electrochemical Society* **1979**, *126*.

(145) Kennedy, J. H.; Frese, K. W. Flatband potentials and donor densities of polycrystalline α-Fe$_2$O$_3$ determined from Mott-Schottky plots. *Journal of The Electrochemical Society* **1978**, *125*, 723.

(146) Pastor-Moreno, G. Electrochemical applications of CVD diamond., Ph.D. Thesis, University of Bristol, 2012.

(147) Song, C.; Zhang, J., Electrocatalytic oxygen reduction reaction. In *PEM feul cell electrocatalyst and catalyst layers. Fundamentals and applications*, Zhang, J., Ed.; Springer London: 2008, pp 89–134.

(148) Chourpa, I.; Douziech-Eyrolles, L.; Ngaboni-Okassa, L.; Fouquenet, J.-F.; Cohen-Jonathan, S.; Soucé, M.; Marchais, H.; Dubois, P. Molecular composition of iron oxide nanoparticles, precursors for magnetic drug targeting, as characterized by confocal Raman microspectroscopy. *The Analyst* **2005**, *130*, 1395.

(149) Vogt, H.; Chattopadhyay, T.; Stolz, H. J. Complete first-order Raman spectra of the pyrite structure compounds FeS$_2$, MnS$_2$ and SiP$_2$. *Journal of Physics and Chemistry of Solids* **1983**, *44*, 869–873.

(150) Raman spectra of opaque minerals., `http://jm-derochette.be/Raman{_}` `Microscope/raman{_}spectra{_}opaque{_}Minerals.htm`, Accessed:2017-01-08.

(151) Chen, Z.; Dinh, H.; Miller, E., *Photoelectrochemical water splitting: standards, experimental methods, and protocols*; Springer: 2013.

(152) Büker, K.; Alonso-Vante, N.; Tributsch, H. Photovoltaic output limitation of n-FeS$_2$ (pyrite) schottky barriers: a temperature-dependent characterization. *Journal of Applied Physics* **1992**, *72*, 5721–5728.

(153) Büker, K.; Alonso-Vante, N.; Scheer, R.; Tributsch, H. Influence of electrochemical activation and surface orientation on the photoresponse of single crystalline pyrite/electrolyte and pyrite/metal junctions. *Berichte der Bunsengesellschaft für physikalische Chemie* **1994**, *98*, 674–682.

(154) Wei, D.; Osseo-Asare, K. Semiconductor electrochemistry of particulate pyrite: Dissolution via hole and electron pathways. *Journal of The Electrochemical Society* **1996**, *143*, 3192–3198.

(155) Arico, A. S.; Antonucci, V.; Giordano, N.; Crea, F.; Antonucci, P. L. Photoelectrochemical behavior of thermally activated natural pyrite-based photoelectrodes. *Materials Chemistry and Physics* **1991**, *28*, 75–87.

(156) Chen, G.; Zen, J. M.; Fan, F. R. F.; Bard, A. J. Electrochemical investigation of the energetics of irradiated FeS$_2$ (pyrite) particles. *The Journal of Physical Chemistry* **1991**, *95*, 3682–3687.

(157) Ahmed, S. M. and Giziewicz, E, Electrochemical studies of iron sulphides in relation to their atmospheric oxidation and prevention of acid drainage, part II. In *Electrochemistry in mineral and metal processing III*, Woods, R., Richardson, P. E., Eds.; Thr Electrochemical Society: 1992; Vol. PV 92-17.

(158) Rochardson, P. E, and Li, Y. Q and Yoon, R. H., The photoelectrochemistry of in.situ fractured pyrite electrodes. In *Electrochemistry in mineral and metal processing III*, Woods, R., Richardson, P. E., Eds.; Thr Electrochemical Society: 1992; Vol. PV 92-17.

(159) Kim, W.; Tachikawa, T.; Majima, T.; Li, C.; Kim, H.-J.; Choi, W. Tin-porphyrin sensitized TiO$_2$ for the production of H$_2$ under visible light. *Energy & Environmental Science* **2010**, *3*, 1789.

(160) Yang, J.; Wang, D.; Han, H.; Li, C. Roles of cocatalysts in photocatalysis and photoelectrocatalysis. *Accounts of Chemical Research* **2013**, *46*.

(161) Humphry-Baker, R.; Lilie, J.; Grätzel, M. In vitro analogs of photosystem II. Combined flash photolytic and conductometric study of light-induced oxygen evolution from water mediated by colloidal RuO$_2$/TiO$_2$. *Journal of the American Chemical Society* **1982**, *104*, 422–425.

(162) Kiwi, J.; Grätzel, M. Oxygen evolution from water via redox catalysis. *Angewandte Chemie International Edition in English* **1978**, *17*, 860–861.

(163) Li, Y.; Lu, G.; Li, S. Photocatalytic transformation of rhodamine B and its effect on hydrogen evolution over Pt/TiO_2 in the presence of electron donors. *Journal of Photochemistry and Photobiology A: Chemistry* **2002**, *152*, 219–228.

(164) Kiwi, J.; Grätzel, M. Optimization of conditions for photochemical water cleavage. Aqueous Pt/TiO_2 (anatase) dispersions under ultraviolet light. *Journal of Physical Chemistry* **1984**, *88*, 1302–1307.

(165) Choi, W.; Termin, A.; Hoffmann, M. R. The role of metal ion dopants in quantum-sized TiO_2: correlation between photoreactivity and charge carrier recombination dynamics. *Journal of Physical Chemistry* **1994**, *98*, 13669–13679.

(166) Bloh, J. Z.; Dillert, R.; Bahnemann, D. W. Designing optimal metal-doped photocatalysts: correlation between photocatalytic activity, doping ratio, and particle size. *The Journal of Physical Chemistry C* **2012**, *116*, 25558–25562.

(167) Kandiel, T. A.; Ivanova, I.; Bahnemann, D. W. Long-term investigation of the photocatalytic hydrogen production on platinized TiO_2: an isotopic study. *Energy & Environmental Science* **2014**, *7*, 1420–1425.

(168) Devipriya, S. P.; Yesodharan, S.; Yesodharan, E. P. Solar photocatalytic removal of chemical and bacterial pollutants from water using Pt/TiO_2-coated ceramic tiles. *International Journal of Photoenergy* **2012**, *2012*, DOI: `10.1155/2012/970474`.

(169) Kandiel, T. A.; Dillert, R.; Bahnemann, D. W. Enhanced photocatalytic production of molecular hydrogen on TiO_2 modified with Pt-polypyrrole nanocomposites. *Photochemical & photobiological sciences* **2009**, *8*, 683–90.

(170) Puangpetch, T.; Sreethawong, T.; Yoshikawa, S.; Chavadej, S. Hydrogen production from photocatalytic water splitting over mesoporous-assembled $SrTiO_3$ nanocrystal-based photocatalysts. *Journal of Molecular Catalysis A: Chemical* **2009**, *312*, 97–106.

(171) Sakthivel, S.; Geissen, S.; Bahnemann, D. W.; Murugesan, V.; Vogelpohl, A. Enhancement of photocatalytic activity by semiconductor heterojunctions : α-Fe_2O_3, WO_3 and CdS deposited on ZnO. **2002**, *148*, 283–293.

(172) Cherevko, S.; Reier, T.; Zeradjanin, A. R.; Pawolek, Z.; Strasser, P.; Mayrhofer, K. J. J. Stability of nanostructured iridium oxide electrocatalysts during oxygen evolution reaction in acidic environment. *Electrochemistry Communications* **2014**, *48*, 81–85.

(173) Ryu, S. Y.; Choi, J.; Balcerski, W.; Lee, T. K.; Hoffmann, M. R. Photocatalytic production of H_2 on nanocomposite catalysts. *Industrial & Engineering Chemistry Research* **2007**, *46*, 7476–7488.

(174) Scharlin, P.; Battino, R.; Silla, E.; Tuñón, I.; Pascual-Ahuir, J. L. Solubility of gases in water: correlation between solubility and the number of water molecules in the first solvation shell. *Pure and Applied Chemistry* **1998**, *70*, 1895–1904.

(175) Peters, E.; Majima, H. Electrochemical reactions of pyrite in acid perchlorate solutions. *Canadian Metallurgical Quarterly* **1968**, *7*, 111–117.

(176) Lowson, R. Aqueous oxidation of pyrite by molecular oxygen. *Chemical Reviews* **1982**, *82*, 461–497.

(177) Buehler, N.; Meier, K.; Reber, J. Photochemical hydrogen production with cadmium sulfide suspensions. *The Journal of Physical Chemistry* **1984**, 3261–3268.

(178) Sayama, K.; Arakawa, H. Effect of carbonate salt addition on the photocatalyticdecomposition of liquid water over Pt–TiO_2 catalyst. *Journal of the Chemical Society, Faraday Transactions* **1997**, *93*, 1647–1654.

(179) Yoshida, Y.; Matsuoka, M.; Moon, S. C.; Mametsuka, H.; Suzuki, E.; Anpo, M. Photocatalytic decomposition of liquid-water on the Pt-loaded TiO_2 catalysts: effects of the oxidation states of Pt species on the photocatalytic reactivity and the rate of the back reaction. *Research on Chemical Intermediates* **2000**, *26*, 567–574.

(180) Salvador, P.; Gutierrez, C. The role of surface state in the electroreduction of dissolved and/or photogenerated oxygen on n-TiO_2 electrodes. *Chemical Physics Letters* **1982**, *86*, 131–134.

(181) Henderson, M. A. A surface science perspective on TiO_2 photocatalysis. *Surface Science Reports* **2011**, *66*, 185–297.

(182) Fujishima, A.; Zhang, X.; Tryk, D. A. Heterogeneous photocatalysis: from water photolysis to applications in environmental cleanup. *International Journal of Hydrogen Energy* **2007**, *32*, 2664–2672.

References

(183) Wang, D.; Hisatomi, T.; Takata, T.; Pan, C.; Katayama, M.; Kubota, J.; Domen, K. Core/shell photocatalyst with spatially separated co-catalysts for efficient reduction and oxidation of water. *Angewandte Chemie (International ed.)* **2013**, *52*, 11252–6.

Appendix

1 Determination of Iron (II/III) Concentration with 1,10-Phenanthroline

In the determination of iron (II) ions in aqueous solutions 1, 10-phenanthroline ($C_{12}H_8N_2$) is used as ligand to form the orange-red $Fe(phen)_3{}^{2+}$ complex:

$$Fe^{2+} + 3\,Phen \longrightarrow Fe(Phen)_3{}^{2+} \tag{1}$$
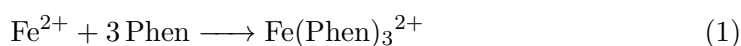
This complex is usually rapidly formed in the acidic pH values. Therefore this reaction was carried out in the pH range of 3.0-3.5 using 0.5 M H_2SO_4.

Ammonium iron (II) sulfate hexahydrate $[Fe(NH_4)_2(SO_4)_2 \cdot 6\,H_2O]$ was used as ferrous source for the determination of absorption coefficient (ε) of the ferrous complex. For this purpose seven standard Fe^{2+} solution was prepared with the concentration of: 0.1, 0.2, 0.3, 0.5, 1.0, 1.5 and 2.0 ppm (correspond to 0.2, 0.5, 0.7, 1.0, 2.5, 3.8, 5.1 $\mu mol\,L^{-1}$ respectively). All of the absorption spectrums were recorded against the reagent blank in the range of 350-700 nm (Figure 1). The absorption values at $\lambda_{max} = 508\,nm$ correspond to ferrous complex. The molar absorption coefficient (ε) of the complex was calculated from the molar concentration and path length according to the Beers low (eq. (3.5)). Linear regression of absorbance versus the concentration of Fe^{2+} in the standards gives a calibration curve (inset of the Figure 1) with the following equation:

$$y = 311.43x + 0.0096 \tag{2}$$

Iron (II) ions concentration was determined with the help of the calibration curve and accounting to the dilution factor of each sample. From each sample first, the iron (II) ions concentration was determined. Iron (III) ions concentration was determined from the total iron concentration in the solution. (The total iron concentration in the solution was determined by reducing Fe^{3+} to Fe^{2+} with hydroxylamine.)
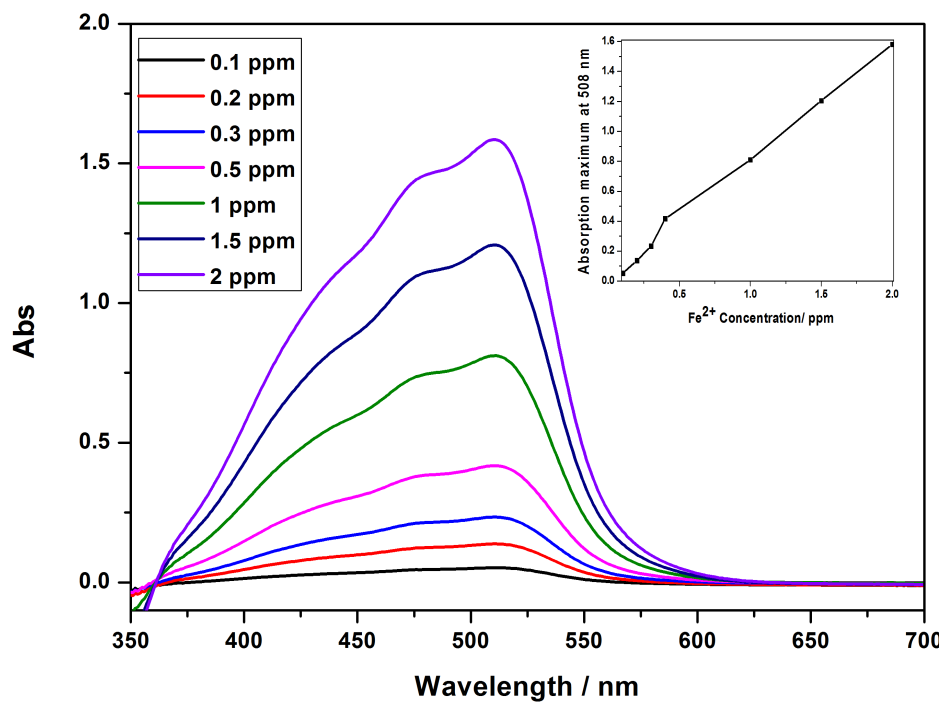
Figure 1: Absorption spectrums of standard Fe^{2+} solution with different concentration (in ppm); inset shows the calibration curve in form of absorbance versus the concentration of Fe^{2+}.

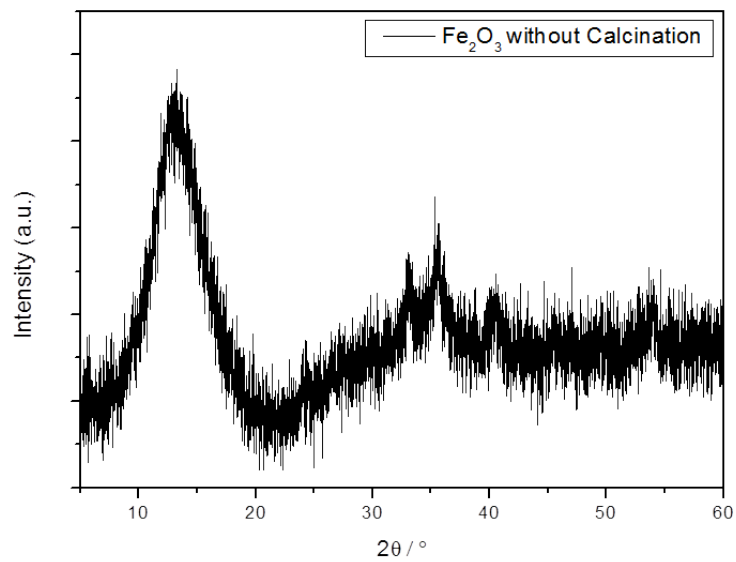# 2 Characterization of Hematite (α-Fe$_2$O$_3$)

Figure 2: XRD pattern of colloidal hematite after freeze-drying

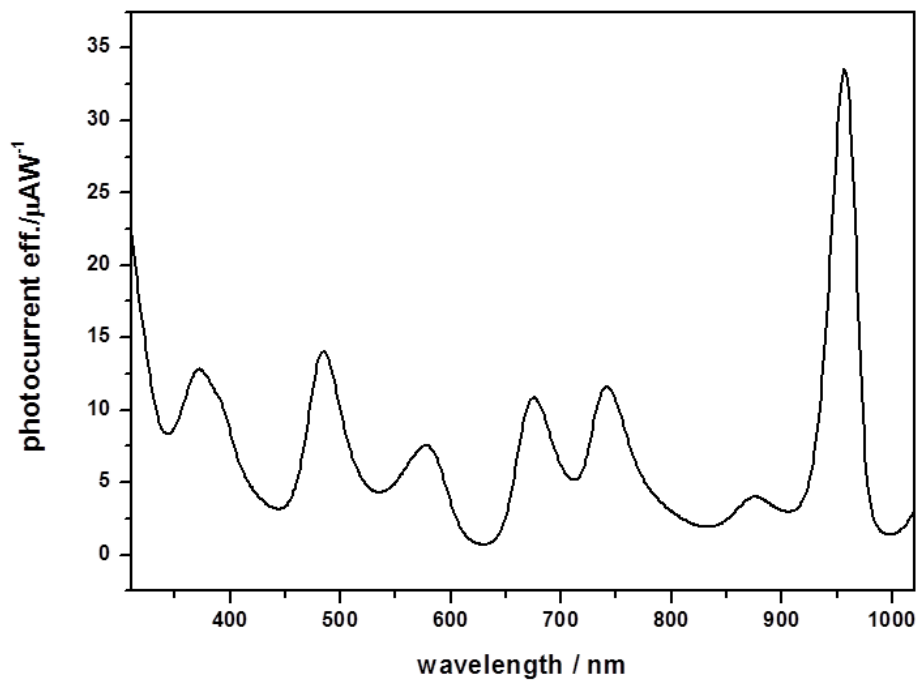*Appendix*

3 PEC Characterization of Pyrite-Electrodes

Figure 3: Photon-to-current conversion efficiency (IPCE) spectrum of the natural
pyrite electrode

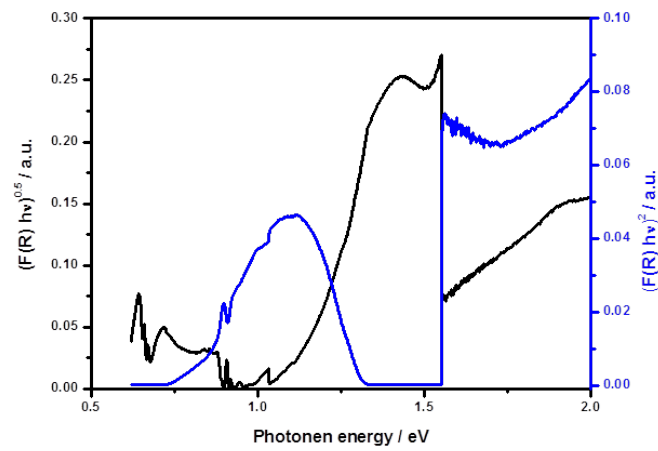# 4 Diffuse reflectance spectra of commercial FeS$_2$ powder

Figure 4: Diffuse reflectance spectra of commercial FeS$_2$ powder, the comparison between the Tauc-plots of the modified Kubelka-Munk function versus the photon energy for indirect allowed transition (black graph) and the forbidden direct transition (blue graph).

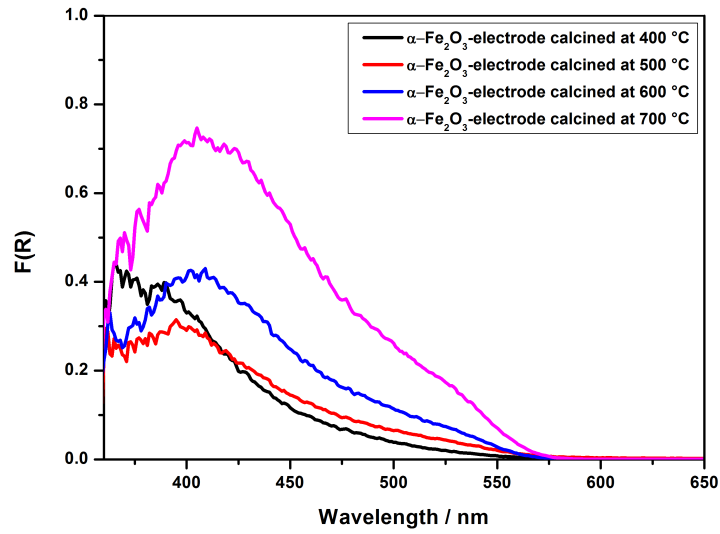# 5 Diffuse reflectance spectra of α-Fe₂O₃ electrodes

Figure 5: Diffuse reflectance spectra of hematite electrodes calcined at different temperature.

Table 1: Band gap energies of hematite electrodes, prepared from the colloidal suspension (15 mM) of α-Fe₂O₃ on FTO substrate and calcined at different temperatures.

Calcination Temperature [°C]	E_g [eV]
400	2.5
500	2.7
600	2.7
700	2.9

6 Characterization of RuO$_2$/α-Fe$_2$O$_3$
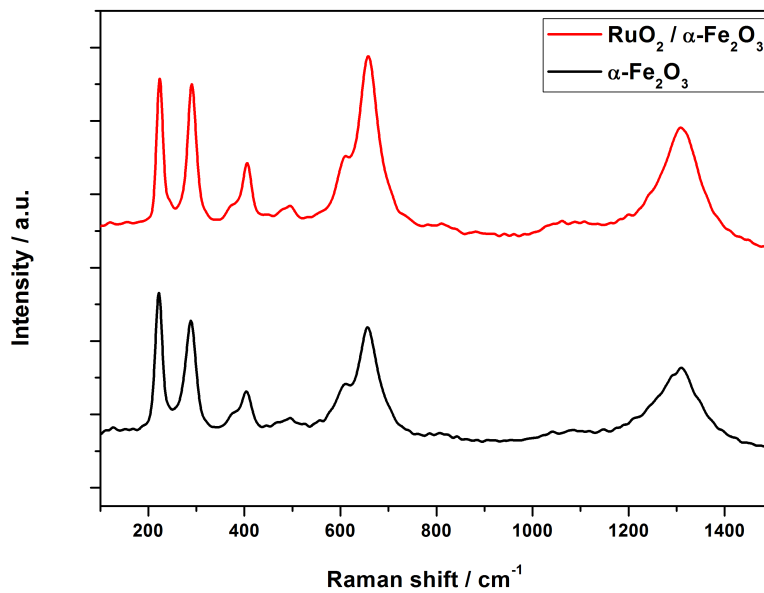
Figure 6: Raman spectra of the bare α-Fe$_2$O$_3$ and RuO$_2$/α-Fe$_2$O$_3$ (with 0.5 wt % of RuO$_2$)

7 Characterization of NiO/FeS₂
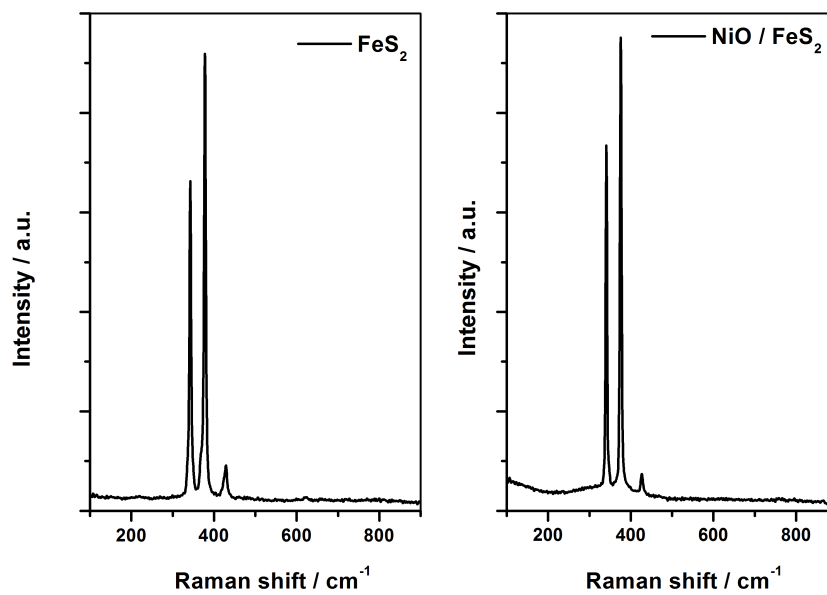
Figure 7: Raman spectra of the bare FeS₂ and NiO/FeS₂ (with 0.5 wt % of NiO)

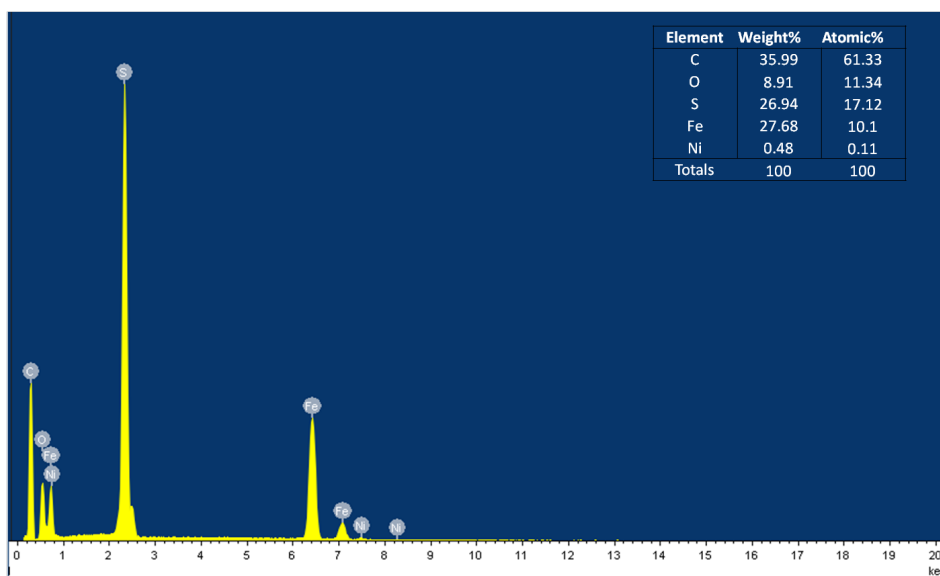| Element	Weight%	Atomic%
C	35.99	61.33
O	8.91	11.34
S	26.94	17.12
Fe	27.68	10.1
Ni	0.48	0.11
Totals	100	100

Figure 8: EDXS spectrum of the NiO/FeS$_2$ (with 0.5 wt % of NiO)

Publications

Journal Publications

„*Photocatalytic Water Splitting employing Pyrite: Effect of Co-Catalysts*“, M. Jami, S. Feroz and D. Bahnemann, Photochemical & Photobiological Sciences, 2016, submitted.

„*Photocatalytic activity of titanium dioxide foams*“, M. Jami, R. Dillert, D. Bahnemann and M. Wark, Catalysis Today, 2016, submitted.

„*Synthesis of mesoprpous $NiO-TiO_2$ nanocompositesphotocatalyst for hydrogen production*“, A. A. Ismail, M. Jami , M. Faisal and D. Bahnemann, International Journal of Hydrogen Energy, In Preparation.

„*Oxygen Production over Cocatalysts modified Hematite (a-Fe_2O_3) by Solar Photocatalysis*“, M. Jami, S. Feroz and D. Bahnemann, Journal of Chemical Engineering and Chemistry Research, In Preparation.

Conference Proceedings Paper

„*Characterization and Activity of TiO_2-Foams for the Photocatalytic Gas Phase Oxidation of NO*“, M. Jami, D. Bahnemann and M. Wark, 8th European Meeting on Solar Chemistry and Photocatalysis: Environmental Applications, June 2014, Thessaloniki, Greece.

Oral Presentations

„*Photocatalytic Water Splitting employing Pyrite: Effect of Co-Catalysts*“, <u>M. Jami</u> and D. Bahnemann, 9th European Meeting on Solar Chemistry and Photocatalysis: Enviromental Applications (SPEA9), June 2016, Strasbourg, France.

„*Nanocrystalline Materials for (Solar) Photoelectrochemical Water Splitting*“, M. Jami, 3rd Russian-German School-Seminar, June 2015, Saint Petersburg, Russia.

„*Photocatalytic activity of titanium dioxide foams*“, M. Jami, 1st Russian-German Workshop, May 2013, Saint Petersburg, Russia.

Poster Presentations

„*Nanocrystalline Materials for (Solar) Photoelectrochemical Water Splitting*", <u>M. Jami</u> and D. Bahnemann, 1th International Solar Fuels Conference (ISF1), 26 April – 1 May 2015, Uppsala, Sweden.

„*Nanocrystalline Electrodes for Photoelectrochemical Water Splitting*", <u>M. Jami</u> and D. Bahnemann , NanoDay, Laboratorium für Nano- und Quantenengineering (LNQE), Leibniz Universität Hannover, October 2014, Hannover, Germany.

„*Photocatalytic Activity of TiO$_2$-Foams*", <u>M. Jami</u>, D. Bahnemann and M. Wark, 20th International Conference on Conversion and Storage of Solar Energy (IPS20), 27 July – 1 August 2014, Berlin, Germany.

„*Characterization and Activity of TiO$_2$-Foams for the Photocatalytic Gas Phase Oxidation of NO*", <u>M. Jami</u>, D. Bahnemann and M. Wark, 8th European Meeting on Solar Chemistry and Photocatalysis: Enviromental Applications (SPEA8), 25-28. June 2014, Thessaloniki, Greece.

„*Photocatalytic Activity of TiO$_2$-Foams*", <u>M. Jami</u>, D. Bahnemann and M. Wark, ZFM Summer-school 2013, Goslar, Germany.

Curriculum Vitae

Personal data

Name	Maryam Jami
Place and Date of Birth	Tangestan (Iran), 11.09.1983
Natinality	Iranian, German

Education

03.2013 − 05.2017	PhD at Institute of Technical Chemistry, Leibniz University Hannover. Topic: „Nanocrystalline materials for solar (photo) electrochemichal water splitting"
03.2010 - 09.2010	Master Thesis at Institute of Physical- and electro- Chemistry, Leibniz University Hannover. Topic: „Photocatalytic activity of TiO_2 foams"
10.2007 - 09.2010	Master of Science in Material and Nanochemistry at Leibniz University Hannover
10.2001 - 04.2005	Bachelor of Science in Pure Chemistry at Persian Gulf University Bushehr (Iran)

Experience

07.2011 - 02.2013	Research assistant at Institute of Technical Chemistry, Leibniz University Hannover

School

10.1997 - 03.2001	Somaie high school (Tangestan / Iran), Graduate at Natural Science